

Washington University in St. Louis

## Washington University Open Scholarship

---

McKelvey School of Engineering Theses & Dissertations

McKelvey School of Engineering

---

Summer 8-15-2022

### Fast and radiation-free high-resolution MR cranial bone imaging for pediatric patients

Parna Eshraghi Boroojeni  
*Washington University in St. Louis*

Follow this and additional works at: [https://openscholarship.wustl.edu/eng\\_etds](https://openscholarship.wustl.edu/eng_etds)



Part of the [Biomedical Engineering and Bioengineering Commons](#)

---

#### Recommended Citation

Eshraghi Boroojeni, Parna, "Fast and radiation-free high-resolution MR cranial bone imaging for pediatric patients" (2022). *McKelvey School of Engineering Theses & Dissertations*. 780.  
[https://openscholarship.wustl.edu/eng\\_etds/780](https://openscholarship.wustl.edu/eng_etds/780)

This Dissertation is brought to you for free and open access by the McKelvey School of Engineering at Washington University Open Scholarship. It has been accepted for inclusion in McKelvey School of Engineering Theses & Dissertations by an authorized administrator of Washington University Open Scholarship. For more information, please contact [digital@wumail.wustl.edu](mailto:digital@wumail.wustl.edu).

WASHINGTON UNIVERSITY IN ST. LOUIS

McKelvey School of Engineering  
Department of Biomedical Engineering

Dissertation Examination Committee:

Hongyu An, Chair

Dennis Barbour

Ulugbek Kamilov

Kamlesh Patel

Monica Shokeen

Fast and Radiation-Free High-Resolution MR Cranial Bone Imaging for Pediatric Patients

by

Parna Eshraghi Boroojeni

A dissertation presented to  
the McKelvey School of Engineering  
of Washington University in  
partial fulfillment of the  
requirements for the degree  
of Doctor of Philosophy

August 2022  
St. Louis, Missouri



© 2022, Parna Eshraghi Boroojeni

# **Table of Contents**

List of Figures .....	v
List of Tables .....	ix
Acknowledgments.....	x
Abstract.....	xii
Chapter 1: Introduction .....	1
1.1 Pediatric Head Trauma and Craniosynostosis: Standard Clinical Imaging Paradigms .....	1
1.2 MRI as a Safe Alternative Option for Cranial Imaging and its Challenges.....	2
1.3 Pediatric Head Trauma and Congenital Craniosynostosis.....	3
1.4 MR Imaging Challenges: Motion and Use of Sedation or General Anesthesia in Pediatric Subjects .....	4
1.5 Robust and Fully Automated Conversion of MR to pCT Images to Translate the Proposed MR Cranial Bone into Clinical Practice .....	6
1.6 MR Reconstruction of Severely Under-Sampled Data to Reduce MR Acquisition Time to Facilitate Clinical Translation.....	8
References.....	12
Chapter 2: Deep learning synthesized pseudo-CT for MR High-Resolution Pediatric Cranial Bone Imaging (MR-HiPCB) .....	17
2.1 Introduction.....	17
2.2 Methods and Materials.....	20
2.2.1 Study Cohort .....	20
2.2.2 Image Acquisition.....	20
2.2.3 Image Pre-processing.....	21
2.2.4 Manual Inverted MRI Processing (iMR) .....	23
2.2.5 Deep-Learning Networks for pCT .....	23
2.2.6 Accuracy Evaluations .....	29
2.3 Results.....	30
2.3.1 MAE and Bone DSC.....	31
2.3.2 Quantitative Difference between pCT and CT .....	33

2.3.3 Qualitative Comparisons.....	34
2.3.4 pCT <sub>Com</sub> at Two MR Field Strengths .....	40
2.4 Discussion and Summary.....	42
References.....	46
Chapter 3: Self-Supervised and Physics-Guided Deep Learning MR Reconstruction: Weighting k-Space Sampling Density in Network Training Loss (wkDeLo) in an Unrolled Network.....	
3.1 Introduction.....	51
3.2 Methods and Materials.....	54
3.2.1 Study Cohort .....	54
3.2.2 Image Acquisition.....	54
3.2.3 Self-supervised and Physics-Guided Deep Learning Reconstruction Using an Unrolled Network.....	54
3.2.4 Weighting k-Space Sampling Density in the Training Loss Function .....	56
3.2.5 Network and Training Details.....	57
3.2.6 Baseline Methods.....	57
3.2.7 Cranial Bone 3D Reconstruction .....	58
3.2.8 Performance Evaluations .....	58
3.3 Results.....	59
3.4 Discussion and Summary.....	65
References.....	68
Chapter 4: Demonstrate that 3D High-Resolution Cranial MR Images Provide CT-Equivalent Bone Information to Clinically Identify Cranial Abnormalities, Patent Sutures, and Fractures ..	
4.1 Introduction.....	73
4.2 Materials and methods .....	75
4.2.1 Study Design and Participants .....	75
4.2.2 Image Acquisition.....	80
4.2.3 Motion Correction.....	81
4.2.4 Deep Learning-Based pCT .....	81
4.2.5 Clinical Evaluations .....	82
4.3 Results.....	84

4.4 Discussion and Summary.....	87
References.....	90
Chapter 5: Summary and Future Work.....	95
5.1 Summary.....	95
5.2 Future Work.....	96
5.2.1 Increase the Sample Size of the Study and Train Different Models for Different Age Ranges.....	96
5.2.2 Develop a 3D Bayesian ResUNet to Estimate Pseudo-CT (pCT) and Uncertainty Maps and Determine the Extent to Which We Can Confidently Identify Cranial Suture Patency, and Fractures via CT-Equivalent Bone 3D High-Resolution Cranial MR Images .....	98
5.2.3 Generate 1 Min Motion-Corrected pCTs.....	99
5.2.4 Introducing New Evaluation Matrices for More Accurate Evaluation.....	100
References.....	101

# List of Figures

Figure 2.1. Training scheme for three ResUNet networks: Whole Head network (NetWH) Bone/Air Enriched network (NetBA) and brain mask network (NetBM) for brain mask segmentation. For the NetWH, the center voxel of patches was randomly placed within the whole head. For the NetBA, the center voxel of patches was placed within the vicinity of bone, suture, and air regions. For the NetBM, the center voxel of patches was randomly placed within the whole head to segment the brain from MR images (A). ResUNet deployment scheme. The pCT<sub>Com</sub> output was created by combining the pCT outputs from both NetWH and NetBA with a brain mask (B)..... 32

Figure 2.2. Mean Absolute Error (MAE) for pCT<sub>NetWH</sub>, pCT<sub>NetBA</sub>, and pCT<sub>Com</sub> (A). Mean Absolute Error (MAE) for pCT<sub>NetWH</sub>, pCT<sub>NetBA</sub>, and pCT<sub>Com</sub> within the cranial bone mask (B). Dice Similarity Coefficient (DSC) box plots for manual inverted MRI (iMR), pCT<sub>NetWH</sub>, pCT<sub>NetBA</sub>, and pCT<sub>Com</sub> (C). pCT<sub>Com</sub> and iMR bone Dice Similarity Coefficients (DSC) as a function of age for all participants (D). The fitted lines from linear regression are shown for both pCT<sub>Com</sub> ( $DSC = 0.005 \times age + 0.85, P < 0.001$ ) and iMR ( $DSC = 0.015 \times age + 0.56, P < 0.001$ ). An Analysis of Covariance (ANCOVA) test showed that the linear regression slope of pCT<sub>Com</sub> DSC is significantly smaller than iMR DSC ( $P < 0.001$ ). .....36

Figure 2.3. Representative Bland-Altman plots between CT and pCT<sub>NetWH</sub> (A and D), pCT<sub>NetBA</sub> (B and E), and pCT<sub>Com</sub> (C and F) within the whole head (A-C), and within the cranial bone mask (D-F). The red horizontal line and the dotted black horizontal lines represent the mean and SD of the differences.....38

Figure 2.4. Representative Images from a patient (4.8-year-old, male). The blue squares mark the lambdoid suture, while the red squares mark the coronal suture. MR images (A), CT (B), BM3D filtered CT (C), pCT<sub>NetWH</sub> (D), pCT<sub>NetBA</sub> (E), pCT<sub>Com</sub> (F), and the corresponding difference images (pCT<sub>NetWH</sub>-CT) (G), (pCT<sub>NetBA</sub>-CT) (H), and (pCT<sub>Com</sub>-CT) (I).....40

Figure 2.5. 3D surface rendered cranial bone image from a participant (4.8-year-old, male) using iMR (A), CT (B), BM3D filtered CT (C), pCT<sub>NetWH</sub> (D), pCT<sub>NetBA</sub> (E), and the pCT<sub>Com</sub> (F).....41

Figure 2.6. Representative volumetric MR (A), pCT<sub>Com</sub> (B), and CT (C) images from a patient (14-year-old, female) with a suture marked in the blue square, and the corresponding 3D surface rendered cranial bone images of manual inverted MR images (iMR) (D), pCT<sub>Com</sub> (E), and CT (F). The blue and red arrows indicate the presence of the coronal and the sagittal sutures, respectively.....42

Figure 2.7. Representative MR (A), pCT<sub>Com</sub> (B), and CT (C) images from a craniosynostosis patient (1.8 year old, female), and the corresponding 3D surface rendered cranial bone images using iMR (D), pCT<sub>Com</sub> (E), and CT (F). Blue arrows indicate the presence of a coronal suture, and the red arrows indicate the absence of a sagittal suture. ....43

Figure 2.8. Representative MR (A), pCT<sub>Com</sub> (B), and CT (C) images from a trauma patient (5.6-year-old, male) with a fracture marked by yellow arrows, and the corresponding 3D surface rendered cranial bone images from iMR (D), pCT<sub>Com</sub> (E) and CT (F). A fracture is marked by a red circle. The proposed deep learning method reduced the noise in the pCT-rendered bone images (E) compared to that of the iMR image (D) (marked by red arrows). ....44

Figure 2.9. Example MR (A), pCT<sub>Com</sub> (B), and CT (C) images from a trauma patient (1.6-year-old, female) with fractures marked by yellow arrows, and the corresponding 3D surface rendered cranial bone images of iMR (D), pCT<sub>Com</sub> (E), and CT (F). A fracture is marked by a red circle. The proposed MR-HiPCB reduced the noise in the surface-rendered bone images (E) compared to that of the iMR image (D) (marked by red arrows). ....45

Figure 3.1. Unfolding network structure .....62

Figure 3.2. MR images 1 min MCNUFFT (A) , 1 min SSDU (B), 1 min un-wkDeLo (C), 1 min (D), and 5 min MCNUFFT reconstruction for 5.6 years old trauma patient, and the corresponding difference images ( $|1 \text{ min MCNUFFT} - 5 \text{ min MCNUFFT}|$ ) (F), ( $|1 \text{ min SSDU} - 5 \text{ min MCNUFFT}|$ ) (G), and ( $|1 \text{ min un-wkDeLo} - 5 \text{ min MCNUFFT}|$ ) (H), ( $|1 \text{ min wkDeLo} - 5 \text{ min MCNUFFT}|$ ) (I). The difference is x10 times. ....65

Figure 3.3. MR images 1 min MCNUFFT (A) , 1 min SSDU (B), 1 min un-wkDeLo (C), 1 min wkDeLo (D), and 5 min MCNUFFT reconstruction for 10.1 years old trauma patient, and the

Corresponding difference images ( $|1 \text{ min MCNUFFT} - 5 \text{ min MCNUFFT}|$ ) (F), ( $|1 \text{ min SSDU} - 5 \text{ min MCNUFFT}|$ ) (G), and ( $|1 \text{ min un-wkDeLo} - 5 \text{ min MCNUFFT}|$ ) (H), ( $|1 \text{ wkDeLo} - 5 \text{ min MCNUFFT}|$ ) (I). The difference is  $\times 10$  times. ....67

Figure 3.4. MR images 1 min MCNUFFT (A) , 1 min SSDU (B), 1 min un-wkDeLo (C), 1 min wkDeLo (D), and 5 min MCNUFFT reconstruction for 16.8 years old patient, and the corresponding difference images ( $|1 \text{ min MCNUFFT} - 5 \text{ min MCNUFFT}|$ ) (F), ( $|1 \text{ min SSDU} - 5 \text{ min MCNUFFT}|$ ) (G), and ( $|1 \text{ min un-wkDeLo} - 5 \text{ min MCNUFFT}|$ ) (H), ( $|1 \text{ min wkDeLo} - 5 \text{ min MCNUFFT}|$ ) (I) The difference is  $\times 10$  times. ....67

Figure 3.5. MR and rendered images from 1 min MCNUFFT (A, F), 1 min SSDU (B, G), 1 min un-wkDeLo (C, H), 1 min wkDeLo (D, I), and 5 min MCNUFFT (E, J) reconstruction for craniosynostosis patient.....68

Figure 3.6. MR and rendered images from 1 min MCNUFFT (A, F), 1 min SSDU (B, G), 1 min un-wkDeLo (C, H), 1 min wkDeLo (D, I), and 5 min MCNUFFT (E, J) reconstruction for craniosynostosis patient.....69

Figure 3.7. MR and rendered images from 1 min MCNUFFT (A, F), 1 min SSDU (B, G), 1 min un-wkDeLo (C, H), 1 min wkDeLo (D, I), and 5 min MCNUFFT (E, J) reconstruction for the trauma patient. Fracture marked in red circle. The proposed wkDeLo reduced the noise in the surface rendered bone images (I) compared to the un-wkDeLo (H) and SSDU images (G) (marked by red arrows). ....70

Figure 3.8. PSNR and SSIM using the un-wkDeLo , SSDU and the proposed wkDeLo reconstructions.....71

Figure 4.1. MR images (left) and the corresponding cranial bone images (right) using the BB (Black Bone) vs GA (Golden Angle radial) scans in a pediatric participant.....85

Figure 4.2. Pseudo-CT(pCT) (A,C,E,G) and CT (B,D,F,H) 3D-reconstruction of images created from MRI of four patients, Patient one with 5 years old and diagnosed with arachnoid cysts and

lambdoid sutures marked in red arrows (A,B), patient two was 19 months old with sagittal synostosis (C,D), patient three was 9 months with Dandy-walker syndrome (E,F), and patient four is 18 months, post-repair of sagittal synostosis (G,H). .....94

Figure 4.3. 1.6 years old, multiple bone fractures. Arrows indicate a fracture. CT axial volumetric sample (A). CT 3D-reconstruction (B, C). pCT axial volumetric sample (D) and pCT 3D-reconstruction (E, F).....96

Figure 4.4. 14 years old, occipital bone fracture. Arrows indicate a fracture. CT axial volumetric sample (A). CT 3D-reconstruction (C). pCT axial volumetric sample (B) and pCT 3D-reconstruction (D).....97



## **List of Tables**

Table 2.1. Patient demographics .....	35
Table 4.1. Patient demographics and imaging data for a trauma patient.....	88
Table 4.2. Patient demographics and imaging data.....	89

# **Acknowledgments**

My Ph.D. advisor, Dr. Hongyu An, is the first person who deserves to be recognized.

She has been an excellent supervisor, an experienced leader, and a wonderful person. She helped when I was stuck on a difficult problem. I can't express how grateful I was to have such a caring and knowledgeable mentor.

I value the critical feedback I received from my thesis committee members, Dr. Kamilov, Dr. Patel, Dr. Barbour, and Dr. Shokeen, which guided my thesis in the right direction.

I would like to thank all the physicians, coordinators, and who helped us recruit patients.

I am grateful to all of my lab mates and friends, as well as Chunwei Ying and Siah Chen, for their assistance and support. Especially Dr. Cihat Eldeniz, with whom I have directly collaborated on BlackBone projects.

I'd also like to thank Dr. Yasheng Chen and Weijie Gan for their invaluable assistance with software development and code debugging, as well as Prof. Paul Commean for editing my manuscripts. I would also like to acknowledge our generous NIH funding sources

I would like to express my gratitude to the Washington University School of Engineering for allowing me to use their dissertation template as a starting point for developing this document.

Parna Eshraghi

*Washington University in St. Louis*

*August 2022*

Dedicated to my caring parents, Mehran Eshrgahi and Sonia Poostpasand

## ABSTRACT OF THE DISSERTATION

Fast and Radiation-Free High-Resolution MR Cranial Bone Imaging for Pediatric Patients

by

Parna Eshraghi Boroojeni

Doctor of Philosophy in Biomedical Engineering

Washington University in St. Louis, 2022

Professor Hongyu An, Chair

Each year, 2.2 million pediatric head computed tomography (CT) scans are performed in the United States. Head trauma and craniosynostosis are two of the most common pediatric conditions requiring head CT scans. Head trauma is common in children and one-third of the patients that present to the emergency room undergoes head CT imaging. Craniosynostosis is a congenital disability defined by a prematurely fused cranial suture. Standard clinical care for pediatric patients with head trauma or craniosynostosis uses high-resolution head CT to identify cranial fractures or cranial sutures. Unfortunately, the ionizing radiation of CT imaging imposes a risk to patients, particularly pediatric patients who are vulnerable to radiation. Moreover, multiple CT scans are often performed during follow-up, exacerbating their cumulative risk. The National Cancer Institute reported that radiation exposure from multiple head CT scans will triple the risk of leukemia and brain cancer. Many medical centers have recently removed CT from the postoperative care of craniosynostosis, limiting postoperative evaluation and highlighting the urgent need for radiation-free imaging. Several “Black bone” magnetic resonance imaging (MRI) methods have been introduced as radiation-free alternatives. Despite the initially encouraging results, these methods have not translated into clinical practice due to several challenges, including

1) subjective manual image processing; 2) long acquisition time. Due to poor signal contrast between bone and its surrounding tissues in MR images, existing post-processing methods rely on extensive manual MR segmentation which is subjective, prone to noise and artifacts, hard to reproduce, and time-consuming. As a result, they do not meet the need for clinical diagnosis and have not been employed clinically. A CT scan takes tens of seconds; however, a high-resolution MR scan takes minutes, which may be challenging for pediatric subject compliance and limit clinical adoption. The overall objective of this study is to develop rapid and radiation-free 3D high-resolution MRI methods to provide CT-equivalent information in diagnosing cranial fractures and cranial suture patency for pediatric patients. Two specific aims are proposed to achieve the overall objective. Aim 1: Develop a fully automated deep learning method to synthesize high-resolution pseudo-CT (pCT) of pediatric cranial bone from MR images. Aim 2: Develop a deep learning image reconstruction method to reduce MR acquisition time.

Aim 1 is to address the issues of subjective manual image processing. In this aim, we developed a robust and fully automated deep learning method to create pCT images from MRI, which facilitates translating MR cranial bone imaging into clinical practice for pediatric patients. Two 3D patch-based ResUNets were trained using paired MR and CT patches randomly selected from the whole head (NetWH) or in the vicinity of bone, fractures/sutures, or air (NetBA) to synthesize pCT. A third ResUNet was trained to generate a binary brain mask using only MRI. The pCT images from NetWH ( $pCT_{NetWH}$ ) in the brain area and NetBA ( $pCT_{NetBA}$ ) in the non-brain area were combined to generate  $pCT_{Com}$ . A manual processing method using inverted MR images (iMR) was also employed for comparison.  $pCT_{Com}$  had significantly smaller mean absolute errors (MAE) than  $pCT_{NetWH}$  and  $pCT_{NetBA}$  in the whole head. Dice Similarity Coefficient (DSC) of the segmented bone was significantly higher in  $pCT_{Com}$  than in  $pCT_{NetWH}$ ,  $pCT_{NetBA}$ , and iMR. DSC from  $pCT_{Com}$

demonstrated significantly reduced age dependence than iMR. Furthermore, pCT<sub>Com</sub> provided excellent suture and fracture visibility comparable to CT.

A fast MR acquisition is highly desirable to translate novel MR cranial to clinical practice in place of CT. However, fast MR acquisition usually results in under-sampled data below the Nyquist rate, leading to artifacts and high noise. Recently, numerous deep learning MR reconstruction methods have been employed to mitigate artifacts and minimize noise. Despite many successes, existing deep learning methods have not accounted for MR k-space sampling density variations. In aim 2, we developed a self-supervised and physics-guided deep learning method by weighting k-space sampling Density in network training Loss (wkDeLo). The proposed method uses an unrolled network with a data consistency (DC) and a regularization (R). A forward Fourier model was used to transform the reconstructed image into k-space. The data consistency between the transformed k-space and the acquired k-space data is enforced in the DC layer. This unrolled network is regularized by k-space deep-learning prior using a convolution neural network. In total, 400 radial spokes were acquired with an acquisition time of 5 minutes. Two disjoint k-space data sets, including the first 1 minute (80 radial spokes) and the remaining 4 minutes (320 radial spokes), were used as the network training input and target. A unique feature of our proposed method is to use a L1 loss weighted by k-space sampling density in an end-to-end training of the unrolled network. Moreover, we also reconstructed images using the same unrolled network structure but without accounting for the k-space sampling density variations in the loss for comparison. In other words, a uniform weighted k-space is used in the training loss (un-wkDeLo). Furthermore, we implemented a well-accepted deep learning reconstruction method, Self-Supervision via Data Undersampling (SSDU) as a baseline method reference. Using the images reconstructed from a 5-min scan as the gold standard, we computed the structural similarity index measure (SSIM) and

peak signal-to-noise ratio (PSNR) for reconstructed images from 1-min k-space data using SSDU, un-wkDeLo, and wkDeLo. The SSIM and PSNR of the wkDeLo images are significantly higher than both SSDU and un-wkDeLo. Moreover, the wkDeLo reconstructed images have the highest sharpness and the least artifacts and noise. In aim 2, we have demonstrated that high quality MR images at a spatial resolution of  $0.6 \times 0.6 \times 0.8 \text{ mm}^3$  could be achieved using only 1 min acquisition time.

Finally, we evaluated the clinical utility of the proposed MR cranial bone imaging in identifying cranial fractures and cranial suture patency. Clinicians by consensus evaluated the MR-derived pCT images. Acceptable image quality was achieved in greater than 90% of all MR scans; diagnoses were 100% accurate in the subset of patients with acceptable image quality. We have demonstrated that the proposed 3D high-resolution MR cranial bone method provided CT-equivalent images for pediatric patients with head trauma or craniosynostosis. This work will have a profound impact on pediatric health by providing clinicians with a rapid diagnostic tool without radiation safety concerns.

# **Chapter 1: Introduction**

## **1.1 Pediatric Head Trauma and Craniosynostosis:**

### **Standard Clinical Imaging Paradigms**

Computed tomography (CT) scanning is a medical imaging technique that allows visualization of an object by acquiring from an x-ray tube and detectors that rotate around the object being scanned. CT scan combines a sequence of X-ray images collected from various angles around your body and uses computer processing to create cross-sectional images (slices) of the bones, blood arteries, and soft tissues within your body. CT scan images contain more information than standard X-rays. They are providing three-dimensional high-resolution images generating sophisticated three-dimensional (3D) reconstructions. CT is an important part of normal patient treatment for a variety of pathologies, including congenital defects, malignancies, and trauma-related complications. In tens of seconds, state-of-the-art CT imaging produces three-dimensional (3D) high-resolution pictures, enabling complex 3D reconstructions. Because of its superior capabilities in bone imaging, 3D reconstructed cranial CT images are widely utilized to diagnose cranial anomalies in pediatric patients. Head (cranial) computed tomography (CT) is the most commonly performed pediatric CT scan with around 2.2 million scans per year in the United States (1,2). The main issue is that ionizing radiation from CT scanning raises cancer risk. Children under the age of five are the most vulnerable (2-7). The number of future radiation-induced cancers from head CTs is expected to be 1210 each year (range 630 to 2370), with 1 in every 5250 head scans in children younger than 5 years resulting in a case of leukemia (2). As



part of their clinical follow-up, many pediatric patients are subjected to multiple head CT scans, which increases the cumulative risk of radiation exposure. Based on research by Pearce et al., the National Cancer Institute has announced that radiation exposure from many head CT scans triples the risk of leukemia and brain cancer (5). When it comes to medical imaging, the use of ionizing radiation must be carefully considered; clinicians are advised to follow the ALARA (As Low as Reasonably Achievable) principles (8). Pediatric radiologists have been focusing on reducing the frequency of CT scans and lowering the radiation dose each scan (9-11). Unfortunately, there is no suitable alternative to CT for detecting cranial anomalies. Therefore, a no-radiation imaging method that can provide CT-equivalent cranial bone information is urgently needed.

## **1.2 MRI as a Safe Alternative Option for Cranial Imaging and its Challenges**

Magnetic Resonance Imaging (MRI) is a safe alternative to CT as it does not expose patients to ionizing radiation. Although MRI provides excellent soft tissue contrasts, it is clinically limited when it comes to evaluating bone structures. Eley and colleagues proposed the "Black Bone" (BB) procedure, which uses a high-resolution conventional 3D gradient echo sequence to distinguish bone from surrounding tissues (12). The vanishing bone signal, which appears white following intensity inversion, was exploited by the BB MRI approaches.

A Cartesian gradient echo sequence is used in this BB approach, which is sensitive to motion artifacts. Clinical evaluation of the BB MRI sequence in pediatric patients with cranial fractures found poor accuracy in the detection of linear fractures in comparison to gold standard CT imaging with a sensitivity of 67% and specificity of 88% (14). With a spatial resolution of 1

mm3, an ultrashort TE (UTE) sequence using pointwise encoding time reduction with radial acquisition (PETRA; Siemens, Erlangen, Germany) was recently adopted to detect skull fractures in pediatric patients (15). The PETRA scan had enhanced detection sensitivity (83%) and specificity (100%) when compared to a prior study utilizing a conventional gradient-echo sequence (14); however, the sensitivity of this approach was reduced to 50% in un-sedated patients.

Despite the initially encouraging results, existing MR cranial bone methods have not translated into clinical practice due to several challenges, including 1) subjective manual image processing; 2) long acquisition time. Due to poor signal contrast between bone and its surrounding tissues in MR images, existing post-processing methods rely on extensive manual MR segmentation which is subjective, prone to noise and artifacts, hard to reproduce, and time-consuming. As a result, they do not meet the need for clinical diagnosis and have not been employed clinically. A CT scan takes tens of seconds; however, a high-resolution MR scan takes minutes, which may be challenging for pediatric subject compliance and limit clinical adoption.

## **1.3 Pediatric Head Trauma and Congenital Craniosynostosis**

Pediatric patients with cranial anomalies such as head trauma and craniosynostosis may benefit from 3D MR cranial bone imaging. In the pediatric population. Head trauma is common in children, with an estimated 1.3 million visits to the emergency department (ED) in 2007 rising to 1.9 million in 2015 (18). A skull fracture occurs in ten to thirty percent of pediatric head traumas. (19) According to Burstein et al., 32 percent of patients who presented to the ED after trauma (falls, assaults, etc.) had head CT imaging done to check for cranial fractures and cerebral

bleeding. The occurrence of a fracture at the outset may necessitate a second head CT scan to monitor healing (20). After a head injury, clinicians must weigh the danger of missing a fracture or traumatic brain injury against the risk of ionizing radiation from CT scans

Craniosynostosis is an uneven head shape caused by the improper early fusing of a cranial suture. Patients might have simple single-suture synostosis or more severe multi-suture synostosis, and craniosynostosis affects one in every 1700 births (21). For diagnosis, a radiologic examination with a head CT is required. Surgical correction improves a patient's aberrant appearance while also treating the negative consequences of reduced cerebral blood flow caused by elevated intracranial pressure on development. Preoperatively, 1 to 3 days after surgery, and 1 year thereafter, a head CT is usually conducted. The preoperative CT is utilized to check for cranial dysmorphology and cranial suture patency. The purpose of a postoperative head CT is to evaluate the postoperative outcome, evaluate cranial defects, and schedule secondary treatments. A head CT scan is performed to check for fractures and cerebral bleeding in patients who have been injured (fell, attack, etc.).

## **1.4 MR Imaging Challenges: Motion and Use of Sedation or General Anesthesia in Pediatric Subjects**

Patient motion can significantly reduce the quality of MR images. Since children are frequently less cooperative than adult patients, pediatric MR imaging is particularly plagued by motion artifacts (22). Repeated examinations are often performed which leads to prolonged studies and added cost. Moreover, the likelihood that the patient will move increases as the scan progresses. Sedation or general anesthesia is commonly used in pediatric patients to minimize movement in clinical MR exams (23). However, sedation or anesthesia is associated with risks including

developmental delay and cardiopulmonary complications (24-26). The U.S. Food and Drug Administration issued a “Drug Safety Communication” warning “that repeated or lengthy use of general anesthetic and sedation drugs in children younger than 3 years of age may affect the development of a child’s brain”. Recommendations were made to avoid sedation or delay elective sedation until after 3 years of age (27). Recent advances in CT imaging have reduced scan time to tens of seconds (30 seconds for head CT), allowing CT imaging in most children without sedation. A retrospective review reported that the sedation rate in head CT imaging was 18% in patients younger than 5 years and 1% in children over 5 years (28). However, for pediatric head MRI, the need for sedation is much higher due to the longer scan time. The sedation rate in MR head imaging was approximately 60-65% in patients 1-6 years old and 32% for all patients under 18 years of age (24). Recent efforts have been made to reduce the need for sedation when performing a pediatric MRI by reducing scan time and using a multi-disciplinary team to coordinate imaging with the patient’s biorhythms (29). However, in a significant proportion of cases, sedation has to be used to obtain clinically acceptable images.

To alleviate the motion issue in the BB and PETRA MR sequences, we implemented a Golden Angle stack-of-stars scan (GA) for its insensitivity to motion to scan pediatric patients without the use of sedation. With a constant azimuthal increment of  $111.25^\circ$ , a golden section of 180, the GA delivers the most uniform K space coverage for any given acquisition length (17). Because the K-space center in GA is sampled frequently, it may be used to detect motion in GA as a single "point" navigator similar to a previous published approach (16).

## **1.5 Robust and Fully Automated Conversion of MR to pCT Images to Translate the Proposed MR Cranial Bone into Clinical Practice**

Generating 3D reconstructed cranial bone images from CT images is straightforward and has been widely accepted as the gold standard in the routine clinical assessment of head trauma and craniosynostosis. The CT Hounsfield units (HU) of bone is notably different from surrounding soft tissue. In contrast, there are significant bone/air and bone/soft tissue signal overlaps in MR images. Moreover, CT HU is a quantitative physical unit, consistent across patients while the MR signal is in arbitrary units and can vary significantly from patient to patient. As a result, it is challenging to reliably distinguish bone from the air or surrounding soft tissues using MRI due to overlapped signal intensity and high inter-subject variability. Thus far, all existing Black Bone analysis methods rely upon extensive manual processing by experienced operators to differentiate bone in the image. These methods are subjective, irreproducible, time-consuming, and unsuitable for routine clinical use. To be clinically applicable, 3D reconstructions are required within minutes of scanning. A robust and automated post-processing method to convert MR images to pseudo-CT (pCT) can greatly facilitate translating MR cranial bone imaging into clinical practice.

Pseudo CT methods using both atlas-based and UTE-based approaches have been developed [30,31]. Emerging deep learning (DL) methods can incorporate multi-scale high-level abstract context information to generate CT-like (pseudo-CT, pCT) images from MR images in a fully automated way. Recently, deep learning models have significantly improved MR estimated pseudo-CT (32-33). Our group has developed a 3D patch-based deep learning-based method for

MR converted pCT images for PET/MR attenuation correction in adults using UTE, DIXON, and T1 weighted MRRAGE images. Pediatric patients have thinner skull bones which make creating a CT-looking images from the MR images more challenging. In the second chapter of the dissertation, we further developed and discussed these deep learning networks to convert GA radial vibe images to high-resolution pCT images for identifying cranial bone fractures and suture patency in pediatric patients with head trauma or craniosynostosis. Sutures and fractures are small regions and fine structures and they need to be preserved in MRI-derived pCT images. We developed a novel and fully automated post-processing method to convert MRI to pCT in pediatric patients based upon a neural network structure called ResUNet (residual U-Net) combining the advantages of both U-Net and residual network structures. Even though traditional U-Net is state of the art in multiple medical image processing applications, it requires fixed-sized input images (34). Our unique deep ResUNet structure offers the following benefits in the conversion of MRI to pCT, 1) using 3D patches as input allows ResUNet to process images of various sizes; 2) training samples can be randomly extracted from all the voxels inside the training images with inherent abundance and diversity; 3) training patches can be extracted from major clusters with significantly different Hounsfield Unit ranges (air/tissue/bone) in a balanced manner to reduce sampling bias in training; 4) adoption of U-Net like structure allows multi-scale high-level abstract context information to be used instead of relying on image intensity alone to convert MR to CT, and 5) deployment is fully automated and fast.

We developed a ResUNet-based deep learning method with enhanced training focusing on sutures and fractures which are the regions of interest in generating high-resolution pCT images from MR images. We combined three ResUNets to generate final pCT images. Two patch-based ResUNets were trained using paired MR and CT patches randomly selected from the whole head

(NetWH) or in the vicinity of bone, fractures/sutures, or air (NetBA) to synthesize pCT. A third ResUNet was trained to generate a binary brain mask using only MRI. We quantitatively assessed the CT and pseudo-CT images using dice coefficients and mean absolute error (MAE). In the second chapter, we demonstrated a promising MRI-based DL approach to achieve CT-equivalent 3D cranial bone images in pediatric subjects using a golden-angle radial (GA) MR scan in a robust and fully automated way to facilitate its translation to clinical use.

## **1.6 MR Reconstruction of Severely Under-Sampled Data to Reduce MR Acquisition Time to Facilitate Clinical Translation**

Recent advances in CT imaging have reduced scan time to tens of seconds, allowing CT imaging in most children without sedation. In contrast, high-resolution MRI acquisition with sub-millimeter voxel size and whole head coverage can be lengthy. Currently, the GA radial MR scan takes 5 minutes. Since children are less cooperative than adult patients, pediatric patients often move during an MR scan, leading to compromised image quality. The long acquisition time is challenging for pediatric patient compliance and limits clinical adoption of MR cranial bone imaging. A short MR acquisition results in under-sampled data below the Nyquist rate, leading to under-sampling artifacts and high noise (low SNR). Therefore, it is highly desirable to develop an imaging technique that is capable of generating high-quality images with a shorter acquisition time to facilitate the adoption of an MR approach

In order to obtain artifact-free images, Nyquist criteria need to be met. The minimum scan acquisition time is fixed by the amount of raw data that must meet the Nyquist criteria chosen by an image field of view and resolution. One approach for reducing the acquisition time is not collecting the full number of K space points demanded by the Nyquist Criterion which results in under-sampling. The Nyquist sampling requirement for our imaging protocol when 100% of the radial spokes required for the Nyquist limit ( $\pi/2 \times \text{matrix size}$ ) is  $320 * \pi/2 \approx 502$ , Radial under-sampling produces streaking artifacts in the image domain. Compressed sensing (CS) reconstruction methods have been developed to reconstruct under-sampled data to reduce scan time and the cost of MR acquisition (35,36). CS methods iteratively optimize a cost function that includes a data fidelity term and a regularization term constructed using a pre-defined prior. However, the prior is usually determined empirically, and the iterative-based procedures is time-consuming to achieve a high-quality reconstruction. Recently, the deep learning approach has been demonstrated to significantly speed up MRI reconstruction with reduced measurements (37-40). Deep learning methods have been developed rapidly in the field of imaging inverse issues. Rather than explicitly establishing an imaging prior, the classic deep-learning strategy relies on training an existing network architecture, such as UNet, to invert the measurement operator by leveraging natural redundancies in the imaging data (41-51). It is common to first bring the measurements to the image domain and train the network to map the corresponding low-quality images to their clean target by solving an optimization problem. End-to-end learning can be expanded to include the measurement operator in unrolled networks. The associated unfolding algorithms treat regularized inversion iterations as layers of a CNN and train it end-to-end in a supervised manner (41, 56-58).



In the third chapter of this dissertation, we proposed a self-supervised and physics-guided deep learning method by weighting k-space sampling density in network training loss. We developed the method for training end-to-end unrolling networks with a weighted loss function by using the density function as weight. We accounted for k-space density variations of MR signal acquisition during the training by adding the density weights to a loss function.

Using images reconstructed from a 5-minute MR scan as the gold standard, we compared the peak signal to noise ratio (PSNR) and similarity index (SSIM) for our 1-min deep learning-based model reconstructed images. Our deep learning-based reconstruction method is effective in reducing artifacts and noise, while still preserving fine details of the structures like sutures and fractures for pediatric patients. We developed a high-resolution MRI reconstruction method to reduce the MR acquisition time from 5 minutes to 1 minute. The 1-minute MR scans provide high-quality visualization of sutures/ fractures in craniosynostosis/trauma patients.

Finally, in the fourth chapter, the CT and pseudo-CT images were qualitatively assessed by two clinicians to identify craniosynostosis or fractures from head trauma cases. We demonstrate that 3D high-resolution cranial MR images provide CT-equivalent bone information to clinically identify cranial abnormalities, patent sutures, and fractures. 3D imaging of cranial structures is used by multiple specialties including Neurosurgery, Craniofacial Surgery, and Neuroradiology for diagnosis, surgical planning, and postoperative evaluation in patients with head trauma and craniosynostosis. The objective of this study is to assess the clinical utility of using the novel MR techniques outlined in this proposal to create CT-equivalent 3D MR cranial bone images without sedation.

In this study, we demonstrated a promising MR method to achieve CT-equivalent 3D cranial bone images in pediatric subjects. We developed a deep learning method to convert MRI images to pCT for pediatric patients. We developed a novel self-supervised and physics-guided MR reconstruction method to shorten the MR acquisition time from 5 minutes to 1 minute. We have demonstrated the clinical utility of the proposed MR cranial bone imaging in detecting skull fractures and sutures in pediatric patients. This work will have a profound impact on pediatric health by providing clinicians with a rapid diagnostic tool without radiation safety concerns.

## **References**

1. Dorfman AL, Fazel R, Einstein AJ, Applegate KE, Krumholz HM, Wang Y, Christodoulou E, Chen J, Sanchez R, Nallamothu BK. Use of medical imaging procedures with ionizing radiation in children: a population-based study. *Arch Pediatr Adolesc Med.* 2011;165(5):458-64. Epub 2011/01/05. doi: 10.1001/archpediatrics.2010.270. PubMed PMID: 21199972; PMCID: PMC3686496.
2. Miglioretti DL, Johnson E, Williams A, Greenlee RT, Weinmann S, Solberg LI, Feigelson HS, Roblin D, Flynn MJ, Vanneman N, Smith-Bindman R. The use of computed tomography in pediatrics and the associated radiation exposure and estimated cancer risk. *JAMA Pediatr.* 2013;167(8):700-7. Epub 2013/06/12. doi: 10.1001/jamapediatrics.2013.311. PubMed PMID: 23754213; PMCID: PMC3936795.
3. Brenner DJ, Elliston CD, Hall EJ, Berdon WE. Estimates of the cancer risks from pediatric CT radiation are not merely theoretical: comment on "point/counterpoint: in x-ray computed tomography, technique factors should be selected appropriate to patient size. against the proposition". *Med Phys.* 2001;28(11):2387-8. PubMed PMID: 11764047.
4. Parker L. Computed tomography scanning in children: radiation risks. *Pediatr Hematol Oncol.* 2001;18(5):307-8. doi: 10.1080/088800101300312564. PubMed PMID: 11452401.
5. Pearce MS, Salotti JA, Little MP, McHugh K, Lee C, Kim KP, Howe NL, Ronckers CM, Rajaraman P, Sir Craft AW, Parker L, Berrington de Gonzalez A. Radiation exposure from CT scans in childhood and subsequent risk of leukaemia and brain tumours: a retrospective cohort study. *Lancet.* 2012;380(9840):499-505. doi: 10.1016/S0140-6736(12)60815-0. PubMed PMID: 22681860; PMCID: 3418594.
6. Smyth MD, Narayan P, Tubbs RS, Leonard JR, Park TS, Loukas M, Grabb PA. Cumulative diagnostic radiation exposure in children with ventriculoperitoneal shunts: a review. *Childs Nerv Syst.* 2008;24(4):493-7. doi: 10.1007/s00381-007-0560-x. PubMed PMID: 18180935.
7. Brenner DJ, Hall EJ. Computed tomography--an increasing source of radiation exposure. *N Engl J Med.* 2007;357(22):2277-84. Epub 2007/11/30. doi: 10.1056/NEJMra072149. PubMed PMID: 18046031.
8. Stewart NM, Hallac RR, Chou PY, Koral K, Blackburn T, Kane AA, Seaward JR. Craniofacial Flash: Minimizing Radiation Dose in Pediatric Craniofacial Computed Tomography. *J Craniofac Surg.*
9. Zulfiqar M, Kim S, Lai JP, Zhou Y. The role of computed tomography in following up pediatric skull fractures. *Am J Surg.* 2017;214(3):483-8. Epub 2016/09/12. doi: 10.1016/j.amjsurg.2016.07.020. PubMed PMID: 27614418

10. Jennings RM, Burtner JJ, Pellicer JF, Nair DK, Bradford MC, Shaffer M, Uspar NG, Tieder JS. Reducing Head CT Use for Children With Head Injuries in a Community Emergency Department. *Pediatrics*. 2017;139(4). Epub 2017/03/04. doi: 10.1542/peds.2016-1349. PubMed PMID: 28255067.
11. Radiation Risks and Pediatric Computed Tomography (CT): A Guide for Health Care Providers 2018. Available from: <https://www.cancer.gov/about-cancer/causes-prevention/risk/radiation/pediatric-ct-scans>.
12. Eley KA, McIntyre AG, Watt-Smith SR, Golding SJ. "Black bone" MRI: a partial flip angle technique for radiation reduction in craniofacial imaging. *Br J Radiol* 2012; **85**(1011): 272-8.
13. Eley KA, Watt-Smith SR, Golding SJ. Three-Dimensional Reconstruction of the Craniofacial Skeleton With Gradient Echo Magnetic Resonance Imaging ("Black Bone"): What Is Currently Possible? *J Craniofac Surg* 2017; **28**(2): 463-7.
14. Dremmen MHG, Wagner MW, Bosemani T, et al. Does the Addition of a "Black Bone" Sequence to a Fast Multisequence Trauma MR Protocol Allow MRI to Replace CT after Traumatic Brain Injury in Children? *AJNR Am J Neuroradiol* 2017; **38**(11): 2187-92.
15. Kralik SF, Supakul N, Wu IC, et al. Black bone MRI with 3D reconstruction for the detection of skull fractures in children with suspected abusive head trauma. *Neuroradiology* 2019; **61**(1): 81-7.
16. Grimm R, Furst S, Dregely I, et al. Self-gated radial MRI for respiratory motion compensation on hybrid PET/MR systems. *Med Image Comput Comput Assist Interv* 2013; **16**(Pt 3): 17-24.
17. Winkelmann S, Schaeffter T, Koehler T, Eggers H, Doessel O. An optimal radial profile order based on the Golden Ratio for time-resolved MRI. *IEEE Trans Med Imaging* 2007; **26**(1): 68-76.
18. Schneier AJ, Shields BJ, Hostetler SG, Xiang H, Smith GA. Incidence of pediatric traumatic brain injury and associated hospital resource utilization in the United States. *Pediatrics*. 2006;118(2):483-92. Epub 2006/08/03. doi: 10.1542/peds.2005-2588. PubMed PMID: 16882799.
19. Nelson EL, Melton LJ, 3rd, Annegers JF, Laws ER, Offord KP. Incidence of skull fractures in Olmsted County, Minnesota. *Neurosurgery*. 1984;15(3):318-24. Epub 1984/09/01. PubMed PMID: 6332998.
20. Burstein B, Upton JEM, Terra HF, Neuman MI. Use of CT for Head Trauma: 2007-2015. *Pediatrics*. 2018;142(4). Epub 2018/09/06. doi: 10.1542/peds.2018-0814. PubMed PMID: 30181120.

21. French LR, Jackson IT, Melton LJ, 3rd. A population-based study of craniosynostosis. *J Clin Epidemiol*. 1990;43(1):69-73. Epub 1990/01/01. PubMed PMID: 2319283.
22. Thieba C, Frayne A, Walton M, et al. Factors Associated With Successful MRI Scanning in Unsedated Young Children. *Front Pediatr* 2018; **6**: 146.
23. Uffman JC, Tumin D, Raman V, Thung A, Adler B, Tobias JD. MRI Utilization and the Associated Use of Sedation and Anesthesia in a Pediatric ACO. *J Am Coll Radiol* 2017; **14**(7): 924-30.
24. Cote CJ, Karl HW, Notterman DA, Weinberg JA, McCloskey C. Adverse sedation events in pediatrics: analysis of medications used for sedation. *Pediatrics* 2000; **106**(4): 633-44.
25. Kannikeswaran N, Mahajan PV, Sethuraman U, Groebe A, Chen X. Sedation medication received and adverse events related to sedation for brain MRI in children with and without developmental disabilities. *Paediatr Anaesth* 2009; **19**(3): 250-6.
26. Malviya S, Voepel-Lewis T, Eldevik OP, Rockwell DT, Wong JH, Tait AR. Sedation and general anaesthesia in children undergoing MRI and CT: adverse events and outcomes. *Br J Anaesth* 2000; **84**(6): 743-8.
27. Derderian CA, Szmuk P, Derderian CK. Behind the Black Box: The Evidence for the U.S. Food and Drug Administration Warning about the Risk of General Anesthesia in Children Younger than 3 Years. *Plast Reconstr Surg* 2017; **140**(4): 787-92.
28. Goldwasser T, Bressan S, Oakley E, Arpone M, Babl FE. Use of sedation in children receiving computed tomography after head injuries. *Eur J Emerg Med* 2015; **22**(6): 413-8.
29. Dong SZ, Zhu M, Bulas D. Techniques for minimizing sedation in pediatric MRI. *J Magn Reson Imaging* 2019.
30. Chen Y, Juttukonda M, Su Y, et al. Probabilistic Air Segmentation and Sparse Regression Estimated Pseudo CT for PET/MR Attenuation Correction. *Radiology* 2015; **275**(2): 562-9.
31. Juttukonda MR, Mersereau BG, Chen Y, et al. MR-based attenuation correction for PET/MRI neurological studies with continuous-valued attenuation coefficients for bone through a conversion from R2\* to CT-Hounsfield units. *Neuroimage* 2015; **112**: 160-8.
32. Liu F, Jang H, Kijowski R, Bradshaw T, McMillan AB. Deep Learning MR Imaging-based Attenuation Correction for PET/MR Imaging. *Radiology* 2018; **286**(2): 676-84.
33. Gong K, Yang J, Kim K, El Fakhri G, Seo Y, Li Q. Attenuation correction for brain PET imaging using deep neural network based on Dixon and ZTE MR images. *Phys Med Biol* 2018; **63**(12): 125011.

34. Ronneberger O, Fisher P, Brox T. U-Net: Convolutional Networks for Biomedical Image Segmentation Medical Image Computing and Computer-Assisted Intervention (MICCAI); 2015. p. 234-41.
35. Donoho DL. Compressed sensing. IEEE Transactions on Information Theory. 2006;52(4):1289-306. doi: 10.1109/TIT.2006.871582.
36. Lustig M, Donoho D, Pauly JM. Sparse MRI: The application of compressed sensing for rapid MR imaging. Magnetic resonance in medicine. 2007;58(6):1182-95.
37. Wang S, Su Z, Ying L, Peng X, Zhu S, Liang F, Feng D, Liang D, editors. Accelerating magnetic resonance imaging via deep learning. 2016 IEEE 13th International Symposium on Biomedical Imaging (ISBI); 2016 2016/04//.
38. Lee D, Yoo J, Tak S, Ye JC. Deep Residual Learning for Accelerated MRI Using Magnitude and Phase Networks. IEEE Transactions on Biomedical Engineering. 2018;65(9):1985-95. doi: 10.1109/TBME.2018.2821699.
39. Liu J, Sun Y, Eldeniz C, Gan W, An H, Kamilov US. RARE: Image Reconstruction Using Deep Priors Learned Without Groundtruth. IEEE Journal of Selected Topics in Signal Processing. 2020;14(6):1088-99. doi: 10.1109/JSTSP.2020.2998402.
40. Lehtinen J, Munkberg J, Hasselgren J, Laine S, Karras T, Aittala M, Aila T. Noise2Noise: Learning Image Restoration without Clean Data. arXiv:180304189 [cs, stat]. 2018.
41. M. T. McCann, K. H. Jin, and M. Unser: Convolutional neural networks for inverse problems in imaging: A review. IEEE Signal Process. Mag., vol. 34, no. 6, pp. 85–95, 2017.
42. A. Lucas, M. Iliadis, R. Molina, and A. K. Katsaggelos. Using deep neural networks for inverse problems in imaging: Beyond analytical methods, IEEE Signal Process. Mag., vol. 35, no. 1, pp. 20–36, Jan. 2018.
43. F. Knoll, K. Hammernik, C. Zhang, S. Moeller, T. Pock, D. K. Sodickson, and M. Akcakaya. Deep learning methods for parallel magnetic resonance imaging reconstruction: A survey of the current approaches, trends, and issues, IEEE Signal Process. Mag., vol. 37, no. 1, pp. 128–140, Jan. 2020.
44. O. Ronneberger, P. Fischer, and T. Brox, U-Net: Convolutional networks for biomedical image segmentation. in Medical Image Computing and Computer-Assisted Intervention (MICCAI), Munich, Germany, October 5-9 2015, pp. 234–241.
45. A. Mousavi, A. B. Patel, and R. G. Baraniuk. A deep learning approach to structured signal recovery. in Proc. Allerton Conf. Communication, Control, and Computing, Allerton Park, IL, USA, Sep. 30-Oct. 2, 2015, pp. 1336–1343.

46. S. Wang, Z. Su, L. Ying, X. Peng, S. Zhu, F. Liang, D. Feng, and D. Liang. Accelerating magnetic resonance imaging via deep learning. in Proc. Int. Symp. Biomedical Imaging, April 2016, pp. 514–517.
47. E. Kang, J. Min, and J. C. Ye. A deep convolutional neural network using directional wavelets for low-dose x-ray ct reconstruction. *Medical Physics*, vol. 44, no. 10, pp. e360–e375, 2017.
48. K. H. Jin, M. T. McCann, E. Froustey, and M. Unser, Deep convolutional neural network for inverse problems in imaging. *IEEE Trans. Image Process.*, vol. 26, no. 9, pp. 4509–4522, Sep. 2017.
49. Y. S. Han, J. Yoo, and J. C. Ye. Deep learning with domain adaptation for accelerated projection reconstruction MR. *Magn. Reson. Med.*, vol. 80, no. 3, pp. 1189–1205, Sep. 2017. 15
50. H. Chen, Y. Zhang, M. K. Kalra, F. Lin, Y. Chen, P. Liao, J. Zhou, and G. Wang. Low-dose ct with a residual encoder-decoder convolutional neural network. *IEEE Trans. Med. Imag.*, vol. 36, no. 12, pp. 2524–2535, Dec. 2017.
51. Y. Li, Y. Xue, and L. Tian. Deep speckle correlation: a deep learning approach toward scalable imaging through scattering media. *Optica*, vol. 5, no. 10, pp. 1181–1190, Oct. 2018.
52. Y. Sun, Z. Xia, and U. S. Kamilov. Efficient and accurate inversion of multiple scattering with deep learning. *Opt. Express*, vol. 26, no. 11, pp. 14 678–14 688, May 2018.
53. D. Lee, J. Yoo, S. Tak, and J. C. Ye. Deep residual learning for accelerated MRI using magnitude and phase networks. *IEEE Trans. Biomed. Eng.*, vol. 65, no. 9, pp. 1985–1995, Sep. 2018.
54. J. C. Ye, Y. Han, and E. Cha. Deep convolutional framelets: A general deep learning framework for inverse problems. *SIAM J. Imag. Sci.*, vol. 11, no. 2, pp. 991–1048, 2018.
55. J. Yoo, S. Sabir, D. Heo, K. H. Kim, A. Wahab, Y. Choi, S.-I. Lee, E. Y. Chae, H. H. Kim, Y. M. Bae, Y.-W. Choi, S. Cho, and J. C. Ye. Deep learning diffuse optical tomography. *IEEE Trans. Med. Imag.*, 2020.
56. Hammernik K, Klatzer T, Kobler E, et al. Learning a variational network for reconstruction of accelerated MRI data. *Magn Reson Med*. 2018;79:3055-3071.
57. Aggarwal HK, Mani MP, Jacob M. MoDL: Model-based deep learning architecture for inverse problems. *IEEE Trans Med Imaging*. 2019;38:394-405
58. B. Yaman, S. A. H. Hosseini, S. Moeller, J. Ellermann, K. Ugurbil, and M. Akçakaya. Self-supervised learning of physics-guided reconstruction neural networks without fully sampled reference data. *Magn. Reson. Med.*, vol. 84, no. 6, pp. 3172–3191, 2020.

# **Chapter 2: Deep learning synthesized pseudo-CT for MR High-Resolution Pediatric Cranial Bone Imaging (MR- HiPCB)**

## **2.1 Introduction**

Head computed tomography (CT) is the most commonly performed pediatric CT scan with approximately 2.2 million scans per year in the United States alone to detect cranial abnormalities in pediatric patients (1,2). Traumatic brain injury is common in the pediatric population resulting in approx. 600,000 to 1.6 million Emergency Department (ED) visits per year (3). Burstein et al. found that 32% of patients who presented to the ED after trauma (fall, assaults, etc.) underwent head CT imaging (4). In children, ten to thirty percent of pediatric head injuries result in a cranial fracture (5). The initial presence of a fracture may require repeat head CT imaging to assess healing in patients seen after trauma. Craniosynostosis is the abnormal early fusion of a cranial suture where one or more sutures close prematurely, causing an irregular-shaped cranium. Craniosynostosis occurs in approximately 1 out of 1700 births (6). The average width of sutures ranges from  $0.8 \pm 0.1$  mm to  $2.4 \pm 0.1$  mm (7), and the width of skull



fracture lines may be small. CT imaging at sub-millimeter resolution is currently the method of choice for identifying skull fractures or evaluating craniosynostosis suture patency in pediatric patients (1,2). Clinicians use both 3D volumetric and surface rendered cranial bone images to evaluate intracranial tissues and skulls for patients with head trauma, while they primarily rely on 3D surface rendered cranial bone images to evaluate sutures for patients with craniosynostosis.

Unfortunately, CT exposes pediatric patients to ionizing radiation and increases their risk for cancer, especially for children younger than five years old (8-12). In addition, repeated head CT scans used as part of clinical follow-up further exacerbate the risk. The National Cancer Institute reported that radiation exposure from multiple head CT scans significantly increases the risk of leukemia and brain cancer (10). Clinicians have to balance the risk of missing certain diagnostic information versus the risk of ionizing radiation from CT. Without exposing patients to ionizing radiation, magnetic resonance imaging (MRI) is a safe alternative to CT. MRI provides superior soft-tissue contrasts, however, MRI is clinically limited for visualizing bone structures due to the low signal from bones. Previously, Eley et al. developed a “Black Bone” method to assess cranial sutures in pediatric patients with craniosynostosis using a conventional 3D gradient-echo MR sequence at a spatial resolution of  $0.94 \times 0.94 \times 2.4 \text{ mm}^3$  (13,14). In the “Black Bone” method, MR shows a low signal in bone and a high signal in the soft tissue, allowing for bone visualization. This method showed a modest accuracy in diagnosing linear fractures in young patients with cranial fractures, with a sensitivity of 67% and specificity of 88% (15). More recently, Pointwise Encoding Time Reduction with radial Acquisition (PETRA) was implemented to detect skull fractures in pediatric patients at a resolution of  $1 \text{ mm}^3$  with greater sensitivity and specificity than the early “Black Bone” method (16). The PETRA method had an

overall sensitivity of 83 percent and a specificity of 100 percent; however, in the un-sedated patients, the sensitivity dropped to 50 percent (16).

The CT Hounsfield units (HU) values for cranial bone are much higher than soft tissues and air, enabling easy separation of bone from its surrounding structures. In contrast, the MR signal intensities from air, bone, and soft tissue have significant overlap. Moreover, the MR signal is in arbitrary units and has large inter-subject variability, while CT HU is a quantitative physical unit and is consistent across patients. Thus far, all existing MR cranial bone methods rely on extensive manual processing by expert operators to delineate bone from the surrounding tissues based on MR signal intensity. Manual processing is subjective, prone to noise and artifacts, hard to reproduce, and time-consuming. As a result, these methods have not been widely utilized clinically (17).

Extensive efforts have been made to derive CT-like images from MRI for PET attenuation correction or radiation therapy planning using atlas- or segmentation-based approaches (18-22), or machine learning algorithms such as random forest (23), Gaussian mixture regression (24,25), and deep learning (26-34). Thus far, most of the deep learning methods were developed in adults and were not designated to address the need to identify small bony structures such as skull fractures or sutures. Compared to adults, the contrast between bone and soft tissue is much smaller in young pediatric patients due to their thinner and less-dense skull bones, resulting in a more challenging problem. The objective of this study was to develop a robust and fully automated deep learning method to synthesize pseudo-CT (pCT) for MRI high resolution

pediatric cranial bone imaging (MR-HiPCB) to eliminate radiation exposure for pediatric patients with head trauma, craniosynostosis, or other congenital head abnormalities.

## **2.2 Methods and Materials**

### **2.2.1 Study Cohort**

After obtaining written consents with an approved IRB from our institution, we recruited 44 pediatric participants under 18 years old with head trauma (n=26) or for cranial suture evaluation (n=18).

### **2.2.2 Image Acquisition**

All participants had a head CT scan as part of their clinical care. A multi-slice Siemens SOMATOM Definition Flash or Force CT scanner (Siemens Medical Systems, Inc., Iselin, NJ) was used with slice thickness ranging from 0.5mm to 1 mm and pixel spacing ranging from 0.31 x 0.31 mm to 0.39 x 0.39 mm for all the CT images. The CT scanning parameters were 0.5 second rotation time, 64 x 0.6 mm collimation, 220 mAs, 120 kVp, a pitch of one, and a 512 x 512 matrix with a scan time ranging from 3.5 to 10.5 seconds. The mean and standard deviation of scan time was  $5.3 \pm 2.1$  seconds.

Forty-two and two participants were scanned using a 3T (Prisma or VIDA) or a 1.5T (Aera) MR scanner (Siemens Healthineers, Erlangen, Germany), respectively. Due to its motion robustness,

a Fast Low-Angle Shot (FLASH) Golden-Angle 3D stack-of-stars radial Volumetric Interpolated Breath-hold Examination sequence (GA-VIBE) was used to acquire MR images. Imaging parameters common for both 3T and 1.5T MR scans are as follows: Field of view = 192 or 220 mm, 224 slices per slab, transverse orientation, Flip angle = 3-5°, Acquisition matrix = 320 × 320, Voxel size = 0.6 x 0.6 x 0.8 mm or 0.69 x 0.69 x 0.8 mm, and a scan duration of approximately 5 minutes. Imaging parameters that were different between the 3T and 1.5T scans were: TR/TE = 4.84 ms/2.47 ms (3T) or 7.7 ms/4.76 ms (1.5T), Bandwidth = 410 (3T) or 280 (1.5T) Hz/pixel, number of radial lines = 400 (3T) and 250 (1.5T).

As a result of brain/head development, pediatric patients have rapid changes in cortical bone density, size, and tissue MR properties in the first years of their life (35,36). MR scans should be performed as soon as possible after the CT scans. Due to MR scanner availability and the patient's schedule, we allow a time interval between CT and MR. The criteria for the allowable time were determined based on patients' age and an estimated rate of fracture healing. For trauma participants with skull fractures, the MR scan should be acquired in less than 3 weeks of the clinical CT in participants younger than 6 months and less than 12 weeks for children older than 6 months. For trauma participants without fracture, MR should be scanned less than 6 months after their CT. For patients with craniosynostosis or other congenital cranial bone abnormalities, an MR scan should be performed less than 6 months after their CT.

### **2.2.3 Image Pre-processing**

The k-space center sampled repeatedly in the GA-VIBE was first used as a navigator to detect participant motion. Subsequently, the motion-compromised stacks of spokes were excluded from the k-space data to minimize motion in the reconstructed MR images, similar to methods described previously (37-43).

All the CT and MR images were interpolated to a resolution of  $0.30 \times 0.30 \times 0.50 \text{ mm}^3$  using trilinear interpolation. A Matlab-based 3-class k-means segmentation was performed to segment the CT head images into the air, soft tissue, and bone. Moreover, suture or fracture neighborhood regions are manually outlined on CT images with a 10 mm sphere “brush” using the 3D Slicer software (44).

The inhomogeneity in MR images was removed using the N4 bias field correction method using default setting: FWHM=0.15, number of control points=4, spline order = 3, bins = 200, Wiener filter noise = 0.01, shrink factor = 2 (45).

The level-set segmentation tool in the Computational Morphometry Toolkit (CMTK) was employed to generate a whole head binary mask in both the MR and CT images using the default settings and a threshold of 0.5 (46). In addition, the FSL Brain Extractor Tool (BET) feature was employed to create a brain mask (BM) from the MRI images. A fractional intensity threshold value of 0.5 and a threshold gradient of 0 were used.

For each subject, the FMRIB’s Linear Image Registration Tool (FLIRT) in the FSL toolbox was employed to register MR images to CT images using a 12-parameter affine registration (full affine: translation, rotation, scale, and shears) with mutual information as the cost function (47).

CT segmented bone mask was used to assign a bone region 10 times the weight of other tissues to enforce a good alignment of the bone region between MR and CT.

#### **2.2.4 Manual Inverted MRI Processing (iMR)**

The bias-field corrected MR images were inverted and then masked using the head binary mask, resulting in high and low signal intensities for the bone and soft tissue, respectively. After the intensity inversion, a participant-specific global intensity threshold was manually selected to generate a binary bone mask using the 3D Slicer software. To further refine cranial bone segmentation, we manually removed small isolated regions and extra-cranial tissue. The manually segmented bone is referred to as the Bone<sub>iMR</sub>. Multiple manual editing tools were employed to construct the head/skull segmentation using the Segment Editor module in the 3D Slicer including thresholding, islands, scissors, and margin. It took 30 minutes to 2 hours to complete the manual processing for each participant using the inverted MRI (iMR) (48).

#### **2.2.5 Deep-Learning Networks for pCT**

A patch-based 3D residual U-Net (ResUNet) structure was previously developed to synthesize pCT from MR images for attenuation correction in PET/MR images in adult participants (34). ResUNet took advantage of both U-Net and residual network structures (49-51). This network allowed the use of multi-scale high-level context information by adopting a UNet structure and utilizing 3D patches to process images of different sizes. The ResUNet architecture was detailed in (34). In brief, the ResUNet consisted of 7 layers with both contraction and expanding paths similar to the conventional U-Net. ResUNet model has added extra skip connections from the

residual block feeding the output of one layer to the next layer in addition to the skip connections in the U-Net from contraction to expanding paths. The state-of-the-art U-Net deep learning method requires fixed-sized images as input. In addition, the recent residual network (ResNet) structure has proven to be necessary to train deeper network structures. Previously, novel 3D residual U-Net (ResUNet) structure for generating pCT from MRI images for the purpose of attenuation correction in PET/MR imager in adult patients was developed . The neural network input uses 3D  $64*64*64$  image patches and consists of 7 layers with both contraction and expanding paths as in the conventional U-Net. The contraction path consists of convolutional and residual blocks to capture the multiscale context information within the 3D input. Following each layer of the contraction path, the feature numbers are doubled with the size of the features is halved. Contrarily, the expanding path consists of deconvolutional and residual blocks with halved feature numbers but doubled 3D sizes after each layer. The final output of the expanding path is the estimated CT in the same size as the initial input. Besides the skip connections in the U-Net from contraction to expanding paths, ResUNet has introduced extra skip connections from the residual block feeding the output of one layer to the next (the lower layer in the contraction path and the upper layer in the expanding path). These extra skip connections ensure the information flow to tackle the gradient vanish problem commonly occurred in the training of deeper neural network structures. We adapted this ResUNet method to pediatric head images through tuning or modification of some network structure parameters such as the number of layers, and patch size.

In this study, three 3D patched-based ResUNet networks were developed to synthesize high-resolution pCT images from GA-VIBE MR images for cranial bone imaging (Figure 2.1A).

Block matching 3D (BM3D) filtering was applied to the CT images. While reducing the noise, the advanced BM3D filter preserved fine details and edge features on self-similar grouped blocks (52). The MR and BM3D filtered CT images were normalized by subtracting the mean intensity of all imaging voxels within the head mask and then dividing by their standard deviation.

The first ResUNet was trained using patches randomly sampled within the whole head mask, which was referred to as NetWH. Since the cranial bone, sutures, and air occupy a small fraction of the total head volume, they were rarely represented in the NetWH training patches. In order to overcome this issue, the second ResUNet, which is referred to as NetBA, enriched its representations in its training patches. In NetBA's training, 50%, 25%, and 25% of the patches were randomly placed within the bone, fracture/suture neighborhood, and air regions, respectively. The training inputs and targets in NetWH and NetBA were normalized 3D MR patches (64 x 64 x 64 voxels) and the corresponding BM3D filtered CT patches from the same location. The third ResUNet, which is referred to as NetBM, was trained to segment brain masks using MRI patches as the inputs and the FSL BET toolbox generated MR brain mask as the target.

3T images from the 42 patients were included in the network training, validation, and testing using five-fold cross-validation. 42 patients were randomly separated into 5 groups, with 8 or 9 patients in each group. The previously published ResUNet pCT network (34) trained using T1 MPRAGE images from adult participants was used as an initial to be retrained using the pediatric data for both NetWH and NetBA. Each time, 28-30 patients were used for training and 4 patients for validation, and 8 or 9 patients for testing. NetWH and NetBA weights evolved by



reducing the  $L_1$  loss function in mean absolute difference (MAE) between the network pCT output and the BM3D filtered CT patches via the Adam optimizer with a batch size of 10 and a learning rate was initialized at  $10^{-3}$  and empirically decreased by half after every 50,000 batches. NetWH and NetBA were trained using 200,000 iterations with 10 patches in each iteration with a total of 2 million randomly sampled 3D patches. The total number of trainable parameters was 123,984,256 for each network. The pCT MAE in NetWH and NetBA reached a steady state after approximately 100,000 iterations. NetBM used a similar ResUNet architecture, except the loss function used binary cross Entropy.

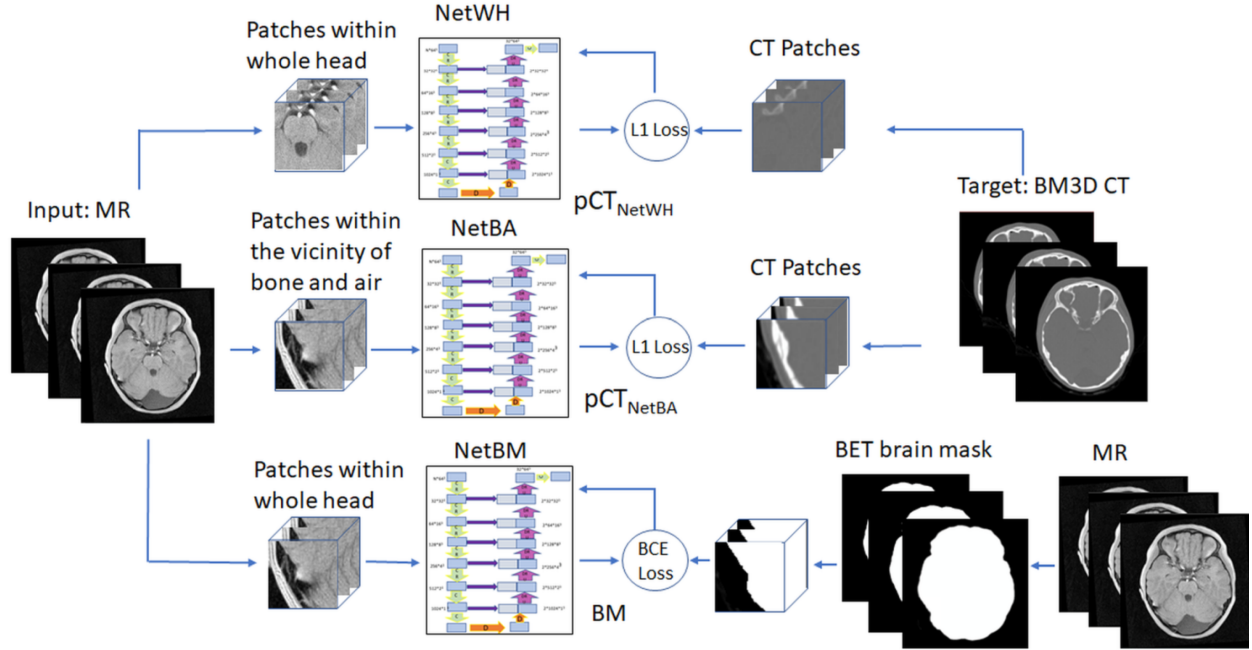
In the network deployment (Figure 2.1B), the trained network was applied to  $64 \times 64 \times 64$  patches using moving windows with a step size of 16 pixels in each direction. In pCT calculation, we only used the central  $32 \times 32 \times 32$  voxels of each patch and the pCT value was assigned as the average of the overlapped regions from different patches.  $pCT_{NetWH}$  and  $pCT_{NetBA}$  were the outputs of NetWH or NetBA, respectively. The brain mask generated by NetBM was then used to combine the brain area from  $pCT_{NetWH}$  and the non-brain area from  $pCT_{NetBA}$  to produce the final combined pCT ( $pCT_{Com}$ ), as detailed in Figure 2.1B.

The 3T MRI-trained NetWH, NetBA and NetBM were also directly applied to create the final  $pCT_{Com}$  for the two 1.5T data sets. For bone segmentation, a threshold of 200 HU was used to generate a binary mask from pCT and CT images (19,29,34,53). The pCT bone segmentation was further refined by removing isolated small islands using Matlab.

The deep ResUNet framework was implemented in PyTorch 1.8.2 (54). The training and validation process took approximately 2 days on a computer equipped with an Intel Xeon Gold 6216 Processor and an NVIDIA Tesla A100 graphics processing unit (GPU). During network deployment, it takes  $3.7 \pm 0.8$  minutes to generate the pCT images from one network using a single GPU.

A

### ResUNet Training Scheme



B

### ResUNet Deployment Scheme

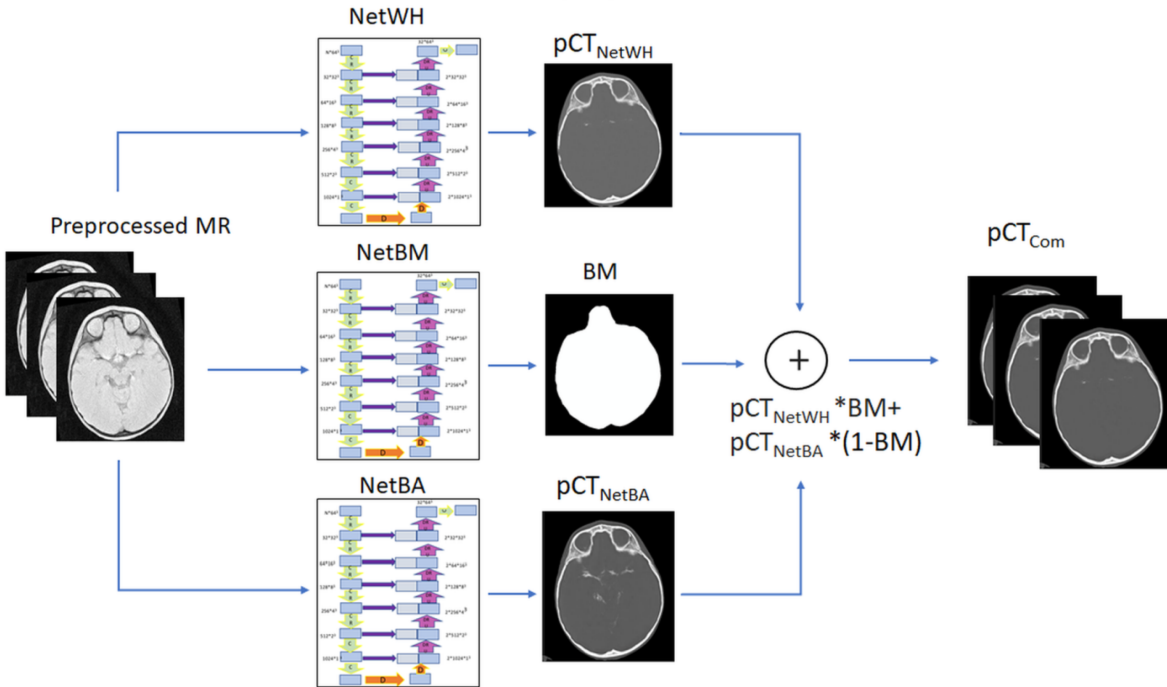


Figure 2.1. Training scheme for three ResUNet networks: Whole Head network (NetWH) Bone/Air Enriched network (NetBA) and brain mask network (NetBM) for brain mask segmentation. For the NetWH, the center voxel of patches was randomly placed within the whole head. For the NetBA, the center voxel of patches was placed within the vicinity of bone, suture, and air regions. For the NetBM, the center voxel of patches was randomly placed within the whole head to segment the brain from MR images (A). ResUNet deployment scheme. The pCT<sub>Com</sub> output was created by combining the pCT outputs from both NetWH and NetBA with a brain mask (B).

### 2.2.6 Accuracy Evaluations

The accuracy of the pCT images was evaluated using the whole head MAE, and cranial bone MAE with the acquired CT images as the gold standard reference. A threshold of 200 HU was applied to CT images to segment cranial bone (Bone<sub>CT</sub>). This CT cranial bone mask was then applied to MR-generated pCT to compute MAE within the cranial bone regions.

MAE between the pCT and the CT were computed for pCT<sub>NetWH</sub>, pCT<sub>NetBA</sub>, or pCT<sub>Com</sub> as

$$MAE = \frac{\sum_{i=1}^n |pCT_i - CT_i|}{n}, \quad (1)$$

where  $i$  is the voxel index and  $n$  is the total number of voxels in the whole head or cranial bone regions.

Bland-Altman tests were performed to evaluate the differences between pCT and CT images in the whole head as well as within CT-defined cranial bone regions.

A threshold of 200 HU was also applied to all pCT images to segment cranial bone (Bone<sub>pCT</sub>).

DSC of the segmented bone between CT and pCT<sub>NetWH</sub>, pCT<sub>NetBA</sub>, pCT<sub>Com</sub>, or iMR was computed as

$$DSC = \frac{2(Bone_{pCT} \cap Bone_{CT})}{Bone_{pCT} + Bone_{CT}} \text{ or } \frac{2(Bone_{iMR} \cap Bone_{CT})}{Bone_{iMR} + Bone_{CT}}, \quad (2)$$

where Bone<sub>CT</sub> is the segmented bone from CT images, while Bone<sub>pCT</sub> or Bone<sub>iMR</sub> is the segmented bone from the pCT<sub>NetWH</sub>, pCT<sub>NetBA</sub>, pCT<sub>Com</sub>, or iMR method.

One-way ANOVA followed by Dunnett's multiple comparisons test was performed to compare whole head MAE and cranial bone MAE of pCT<sub>NetWH</sub>, pCT<sub>NetBA</sub>, and pCT<sub>Com</sub> using GraphPad Prism (version 9.0.0, GraphPad Software, San Diego, California USA). One-way ANOVA followed by Dunnett's multiple comparisons tests was also performed to compare Bone DSC of pCT<sub>NetWH</sub>, pCT<sub>NetBA</sub>, pCT<sub>Com</sub>, and iMR. Linear regressions were employed to investigate whether bone DSC of pCT<sub>Com</sub> or iMR were significantly dependent on age using GraphPad Prism. Moreover, DSC's age dependence was compared between pCT<sub>Com</sub> and iMR using an Analysis of Covariance (ANCOVA). In all statistical analyses,  $P < 0.05$  is considered significant.

## 2.3 Results

The demographic information of all participants is shown in Table 2.1. Of the 42 participants who had a 3T MR scan, 24 had head trauma, and 18 had cranial suture evaluation. The two

participants who were scanned using a 1.5T MR had head trauma. Nine patients of the total 44 participants were sedated.

Table 2.1. Patient demographics

MR field strength	3T (n=42)		1.5T (n=2)
Patient groups	Suture Evaluation (n = 18)	Head Trauma (n = 24)	Head Trauma (n=2)
Age in years (median, IQR)	2.5 (1.5 – 7.2)	11.75 (6.6 – 15.2)	1.5 and 0.4
Female (n, %)	4 (22%)	12 (50%)	1 (50%)
CT to MR in days (median, IQR)	37.5 (12 - 100)	27 (18-102)	0 and 36
Sedation (n)	7	1	1

### 2.3.1 MAE and Bone DSC

The whole head MAE of the pCT<sub>Com</sub> ( $68.01 \pm 14.86$  HU) was significantly smaller than the MAE of the pCT<sub>NetWH</sub> ( $82.58 \pm 16.98$  HU,  $P < 0.0001$ ) and pCT<sub>NetBA</sub> ( $91.32 \pm 17.2$  HU,  $P < 0.0001$ ) (Figure 2.2A). Moreover, the cranial bone MAE of the pCT<sub>Com</sub> ( $227.92 \pm 46.88$  HU) was significantly smaller than the MAE of the pCT<sub>NetWH</sub> ( $287.85 \pm 59.46$  HU,  $P < 0.0001$ ), and it was similar to pCT<sub>NetBA</sub> ( $230.20 \pm 46.17$  HU, ns) (Figure 2.2B).

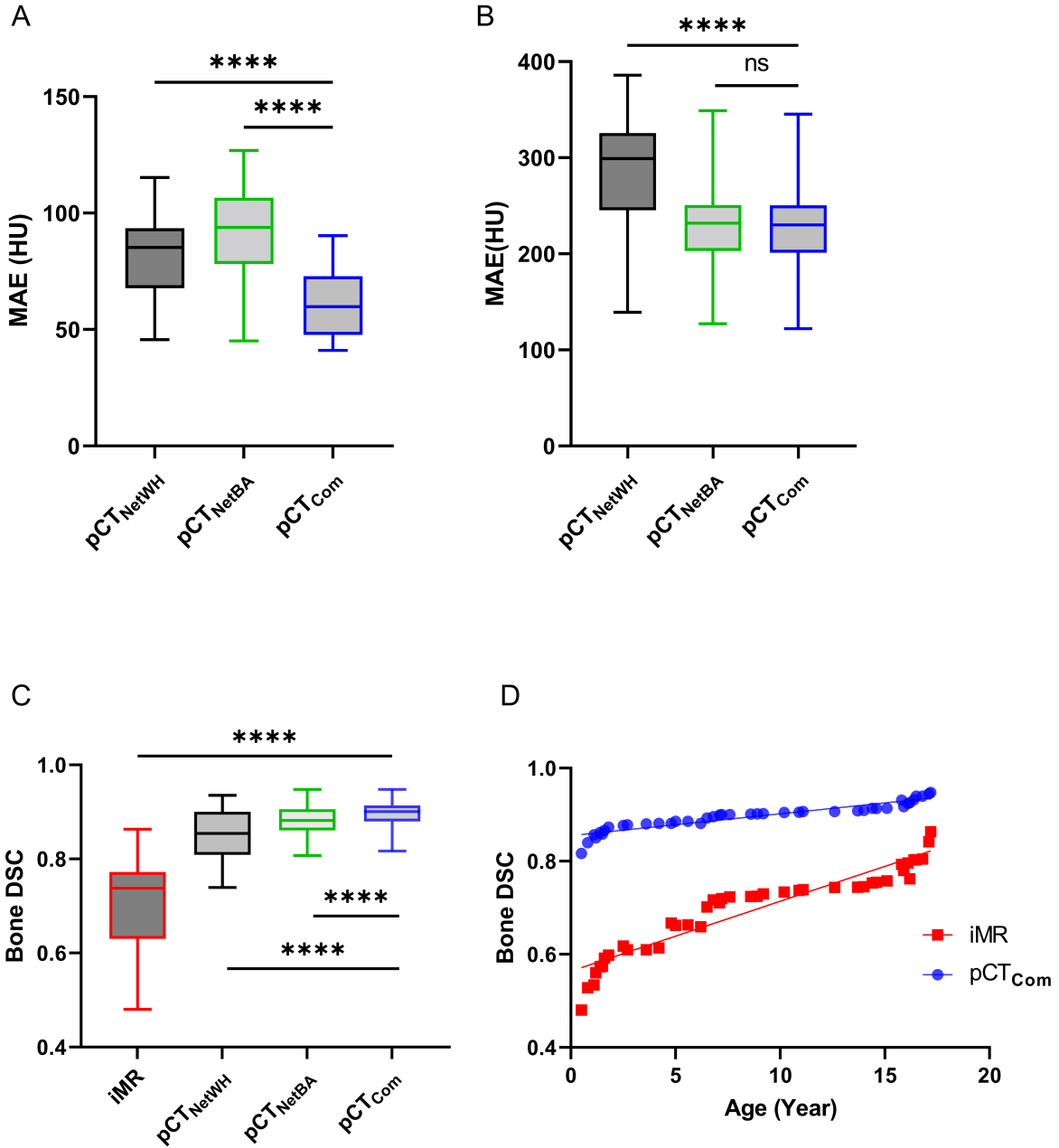


Figure 2.2. Mean Absolute Error (MAE) for pCT<sub>NetWH</sub>, pCT<sub>NetBA</sub>, and pCT<sub>Com</sub> (A). Mean Absolute Error (MAE) for pCT<sub>NetWH</sub>, pCT<sub>NetBA</sub>, and pCT<sub>Com</sub> within the cranial bone mask (B). Dice Similarity Coefficient (DSC) box plots for manual inverted MRI (iMR), pCT<sub>NetWH</sub>, pCT<sub>NetBA</sub>, and pCT<sub>Com</sub> (C). pCT<sub>Com</sub> and iMR bone DSC as a function of age for all participants (D). The

fitted lines from linear regression are shown for both pCT<sub>Com</sub> ( $DSC = 0.005 \times age + 0.85$ ,  $P < 0.001$ ) and iMR ( $DSC = 0.015 \times age + 0.56$ ,  $P < 0.001$ ). An Analysis of Covariance (ANCOVA) test showed that the linear regression slope of pCT<sub>Com</sub> DSC is significantly smaller than iMR DSC ( $P < 0.001$ ).

Bone DSC of pCT<sub>Com</sub> ( $0.90 \pm 0.02$ ) was significantly higher than those of pCT<sub>NetWH</sub> ( $0.86 \pm 0.04$ ,  $P < 0.0001$ ), pCT<sub>NetBA</sub> ( $0.88 \pm 0.03$ ,  $P < 0.0001$ ), and iMR ( $0.71 \pm 0.09$ ,  $P < 0.0001$ ) (Figure 2.2C). Bone DSC of iMR showed a significant age dependence with lower DSC in participants with younger ages ( $DSC = 0.015 \times age + 0.56$ ,  $P < 0.001$ ) (Figure 2.2D). The diminished MR signal contrast between bone and soft tissue in young participants may explain this finding. The proposed pCT<sub>Com</sub> method also had an age dependence in bone DSC ( $DSC = 0.005 \times age + 0.85$ ,  $P < 0.001$ ). However, the age dependence is significantly smaller in pCT<sub>Com</sub> than in iMR ( $P < 0.001$ ).

### 2.3.2 Quantitative Difference between pCT and CT

Bland Altman plots were shown in Figure 2.3 for the whole head (upper row) and cranial bone (lower row) between pCT (pCT<sub>NetWH</sub>, pCT<sub>NetBA</sub>, or pCT<sub>Com</sub>) and CT. The mean and standard deviation of differences between pCT and CT (pCT-CT) were  $-13.80 \pm 30.90$  HU for pCT<sub>NetWH</sub> (A),  $-17.40 \pm 65.80$  HU for pCT<sub>NetBA</sub> (B),  $-6.92 \pm 20.58$  HU for pCT<sub>Com</sub> (C) in the whole head (upper row), and  $-132.39 \pm 254.25$  HU for pCT<sub>NetWH</sub> (D),  $-88.50 \pm 211.66$  HU for pCT<sub>NetBA</sub> (E),  $-85.19 \pm 209.34$  HU for pCT<sub>Com</sub> (F) in the cranial bone regions (lower row). All pCT images,



including  $pCT_{NetWH}$ ,  $pCT_{NetBA}$ ,  $pCT_{Com}$ , have lower HU than CT.  $pCT_{Com}$  showed the smallest mean and standard deviation in the difference between the pCT and CT.

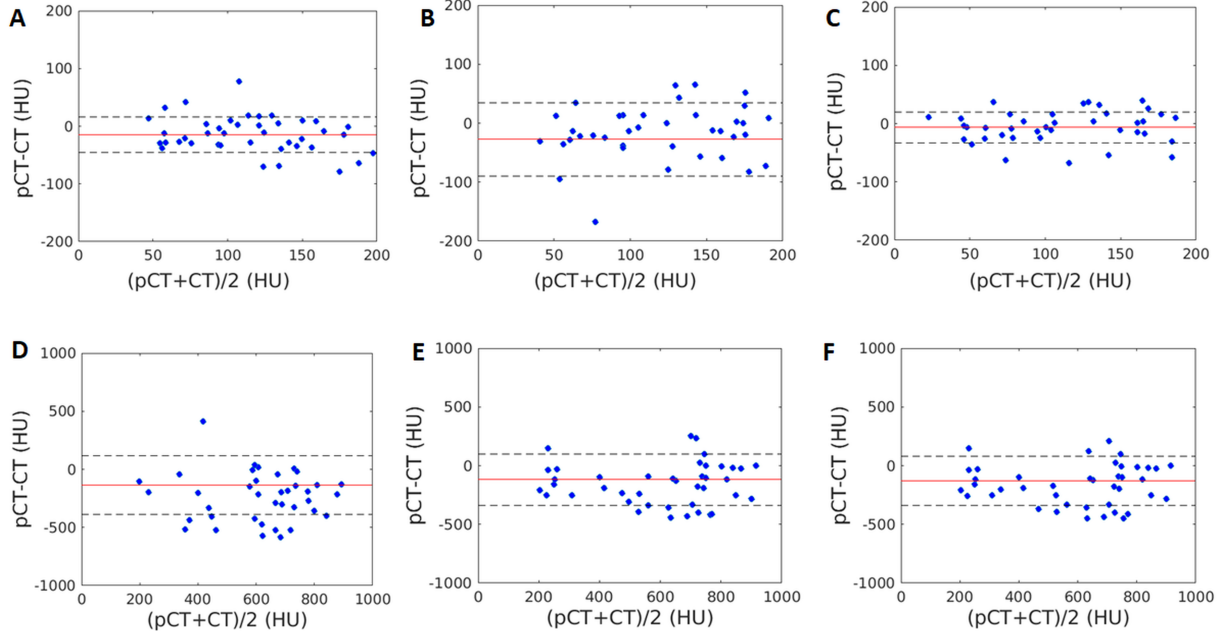


Figure 2.3. Representative Bland-Altman plots between CT and  $pCT_{NetWH}$  (A and D),  $pCT_{NetBA}$  (B and E), and  $pCT_{Com}$  (C and F) within the whole head (A-C), and within the cranial bone mask (D-F). The red horizontal line and the dotted black horizontal lines represent the mean and SD of the differences.

### 2.3.3 Qualitative Comparisons

Representative images from a 4.8-year-old male participant were provided in Figure 2.4. The skull sutures were enhanced after the BM3D filtering (Figure 2.4C) compared to the original CT (Figure 2.4B).  $pCT_{NetWH}$  (Figure 2.4D) provides a more accurate pCT signal in soft tissue than  $pCT_{NetBA}$  (Figure 2.4E). Compared to  $pCT_{NetWH}$ ,  $pCT_{NetBA}$  demonstrated more distinguished

bony structures. pCT<sub>Com</sub> (Figure 2.4F) demonstrated accuracy in soft tissues and high visibility of small bony structures. Difference maps between pCT<sub>NetWH</sub> and CT (Figure 2.4G), pCT<sub>NetBA</sub> and CT (Figure 2.4H), and pCT<sub>Com</sub> and CT (Figure 2.4I) in HU were displayed. The corresponding surface rendered cranial bone images from the same participant were displayed in Figure 2.5. Similar to Figure 2.4, Figure 2.5 confirmed that pCT<sub>NetBA</sub> (Figure 2.5E) improved sutures visibility compared to pCT<sub>NetWH</sub> (Figure 2.5D). Since pCT<sub>Com</sub> (Figure 2.5F) uses the bone regions of pCT<sub>NetBA</sub>, surface rendered cranial bone looks similar between pCT<sub>Com</sub> (Figure 2.5F) and pCT<sub>NetBA</sub> (Figure 2.5E).

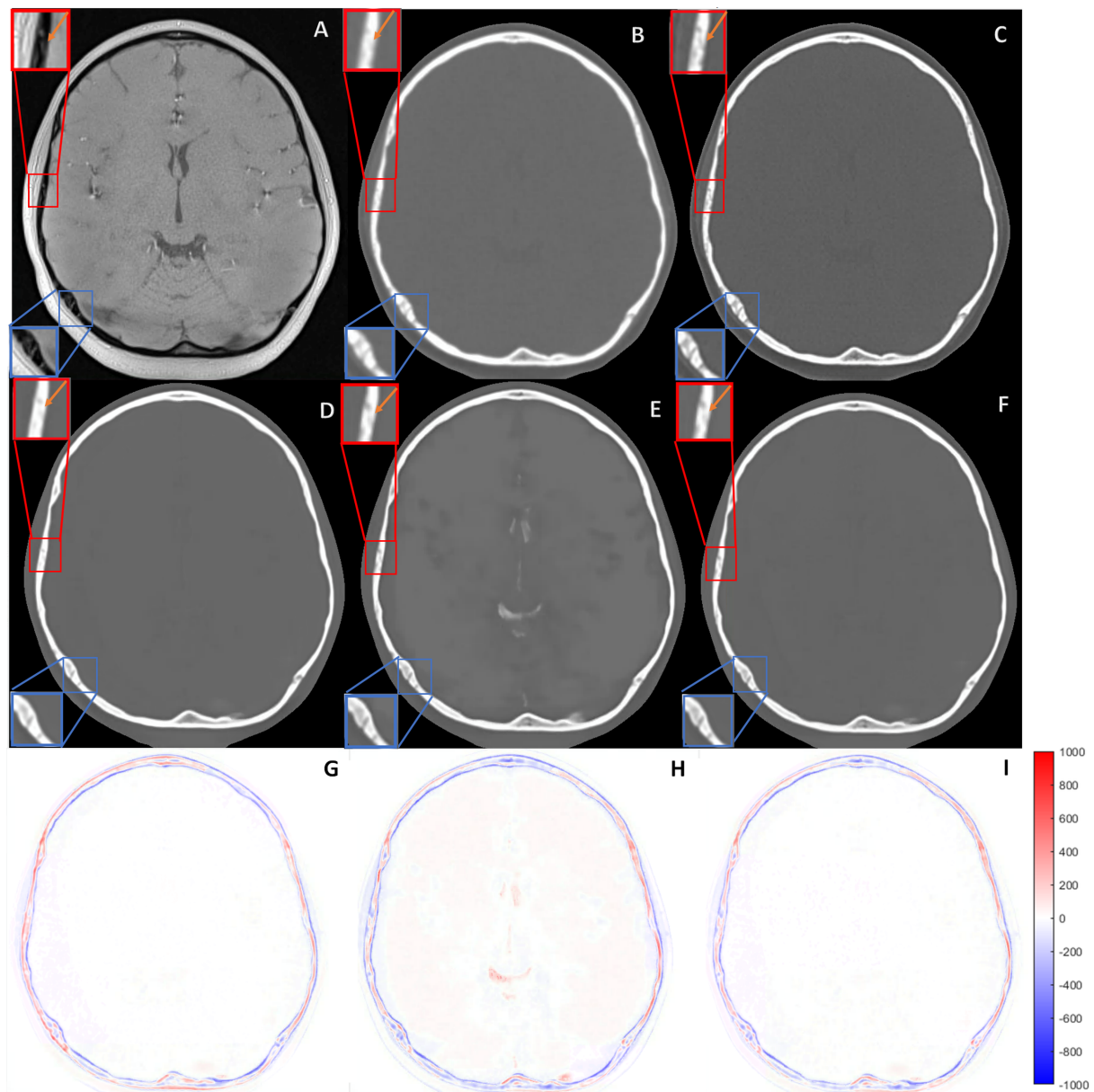


Figure 2.4. Representative Images from a patient (4.8-year-old, male). The blue squares mark the lambdoid suture, while the red squares mark the coronal suture. MR images (A), CT (B), BM3D filtered CT (C),  $pCT_{NetWH}$  (D),  $pCT_{NetBA}$  (E),  $pCT_{Com}$  (F), and the corresponding difference images ( $pCT_{NetWH}-CT$ ) (G), ( $pCT_{NetBA}-CT$ ) (H), and ( $pCT_{Com}-CT$ ) (I)

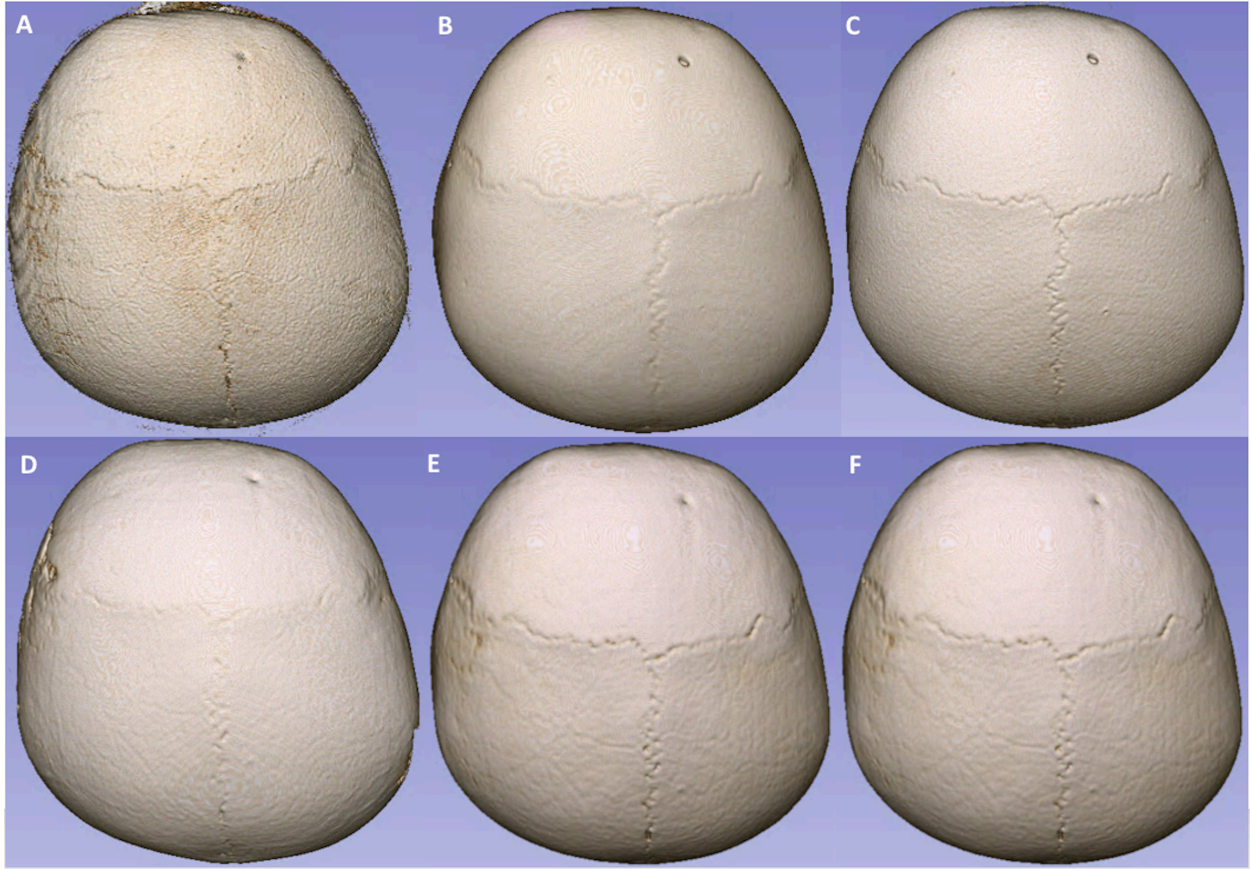


Figure 2.5. 3D surface rendered cranial bone image from a participant (4.8-year-old, male) using iMR (A), CT (B), BM3D filtered CT (C), pCT<sub>NetWH</sub> (D), pCT<sub>NetBA</sub> (E), and the pCT<sub>Com</sub> (F).

Example MR, pCT<sub>Com</sub>, and CT volumetric and 3D rendered cranial bone images from a 14-years-old participant were displayed in Figure 2.6. High-resolution pCT<sub>Com</sub> generated by the proposed MR-HiPCB method produced similar suture visibility for the coronal and sagittal sutures compared to CT. Another example from a 1.8 year old participant with craniosynostosis was shown in Figure 2.7. Similar to CT, pCT<sub>Com</sub> demonstrated that this participant had an open coronal suture (Figure 2.7D, E, and F, marked by blue arrows) but a closed sagittal suture (Figure 2.7D, E, and F, marked by red arrows). Figure 2.8 shows an example of MRI, pCT<sub>Com</sub>,

and CT volumetric and 3D rendered cranial bone images from a trauma participant with fractures (marked by yellow arrowed and red ovals). The skull fractures can be readily identified on pCT<sub>Com</sub> images similar to CT. Moreover, the surface rendered cranial bone images from pCT<sub>Com</sub> showed much less noise than iMR (Figure 2.8D, E, and F, marked by red arrows), suggesting the proposed MR-HiPCB method can reduce noise.

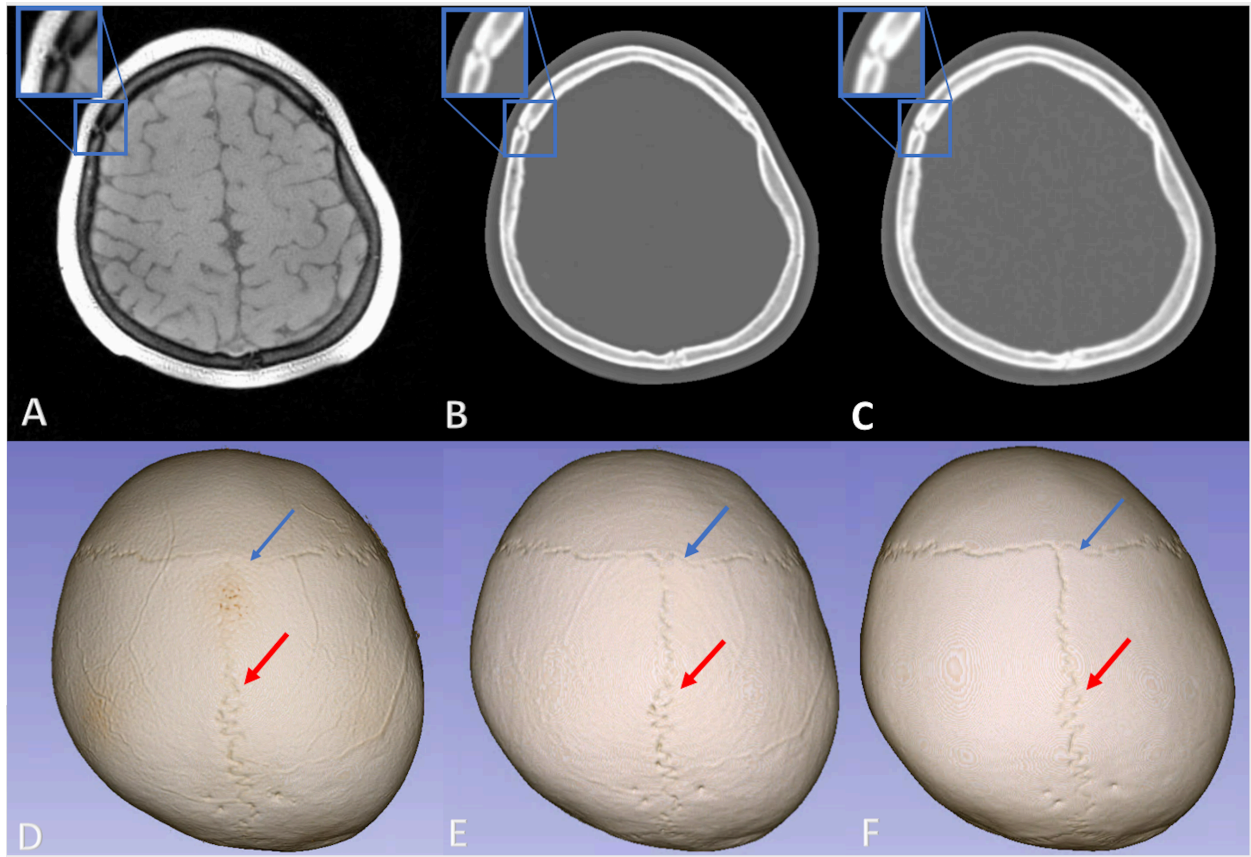


Figure 2.6. Representative volumetric MR (A), pCT<sub>Com</sub> (B), and CT (C) images from a patient (14-year-old, female) with a suture marked in the blue square, and the corresponding 3D surface rendered cranial bone images of manual inverted MR images (iMR) (D), pCT<sub>Com</sub> (E), and CT (F). The blue and red arrows indicate the presence of the coronal and the sagittal sutures, respectively.



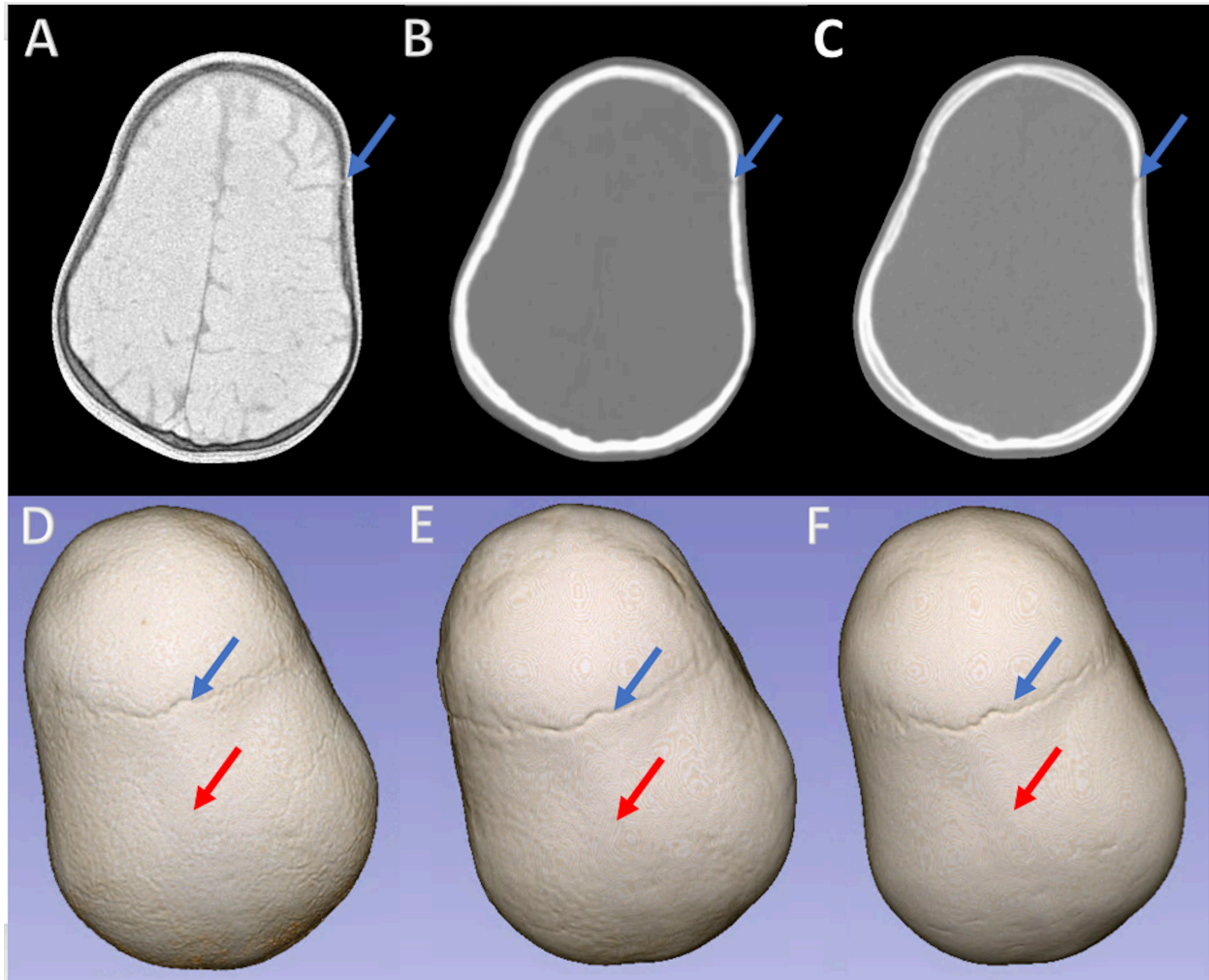


Figure 2.7. Representative MR (A), pCT<sub>Com</sub> (B), and CT (C) images from a craniosynostosis patient (1.8 year old, female), and the corresponding 3D surface rendered cranial bone images using iMR (D), pCT<sub>Com</sub> (E), and CT (F). Blue arrows indicate the presence of a coronal suture, and the red arrows indicate the absence of a sagittal suture.

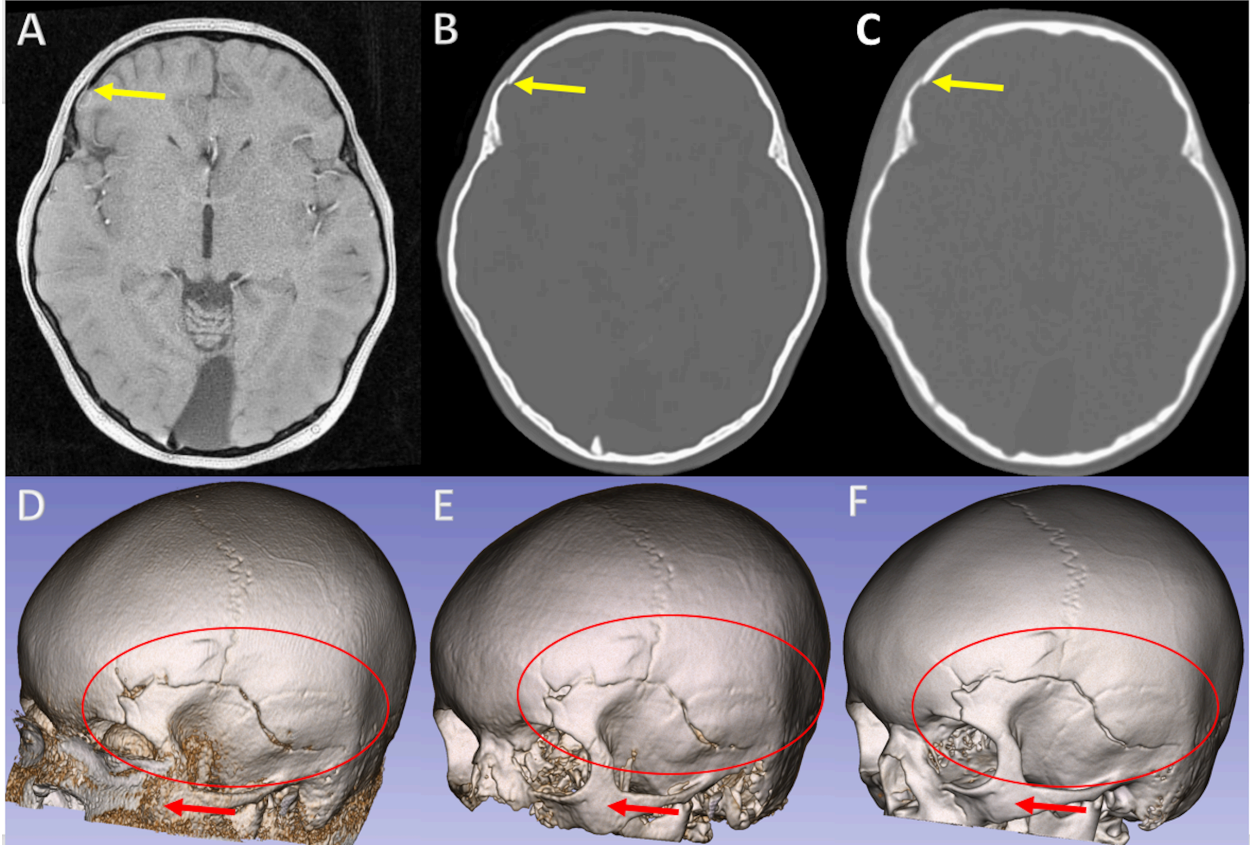


Figure 2.8. Representative MR (A), pCT<sub>Com</sub> (B), and CT (C) images from a trauma patient (5.6-year-old, male) with a fracture marked by yellow arrows, and the corresponding 3D surface rendered cranial bone images from iMR (D), pCT<sub>Com</sub> (E) and CT (F). A fracture is marked by a red circle. The proposed deep learning method reduced the noise in the pCT-rendered bone images (E) compared to that of the iMR image (D) (marked by red arrows).

### 2.3.4 pCT<sub>Com</sub> at Two MR Field Strengths

The proposed networks were trained using images acquired on 3T MR scanners. Two participants scanned on the 1.5T scanners were not included in the network training due to low SNR and slightly different image parameters. To test the feasibility of across magnetic field-

strength application of our proposed approach, we directly applied the 3T trained networks to the two 1.5T image sets. In an example demonstrated in Figure 2.9, skull fractures can be readily distinguished (marked by yellow arrows and red ovals). The noise in the facial region in pCT<sub>Com</sub> (Figure 2.9E) is much less than in iMR (Figure 2.9D). For this patient, the pCT<sub>Com</sub> MAEs were 83.61 HU and 169.02 HU in the whole head and cranial bone regions, respectively. The bone DSC of pCT<sub>Com</sub> and iMR were 0.84 and 0.73, respectively. For another participant scanned at 1.5T, the pCT<sub>Com</sub> MAEs were 71.15 HU and 164.41 HU in the whole head and cranial bone regions, respectively. The DSC of pCT<sub>Com</sub> and iMR were 0.83 and 0.65, respectively.

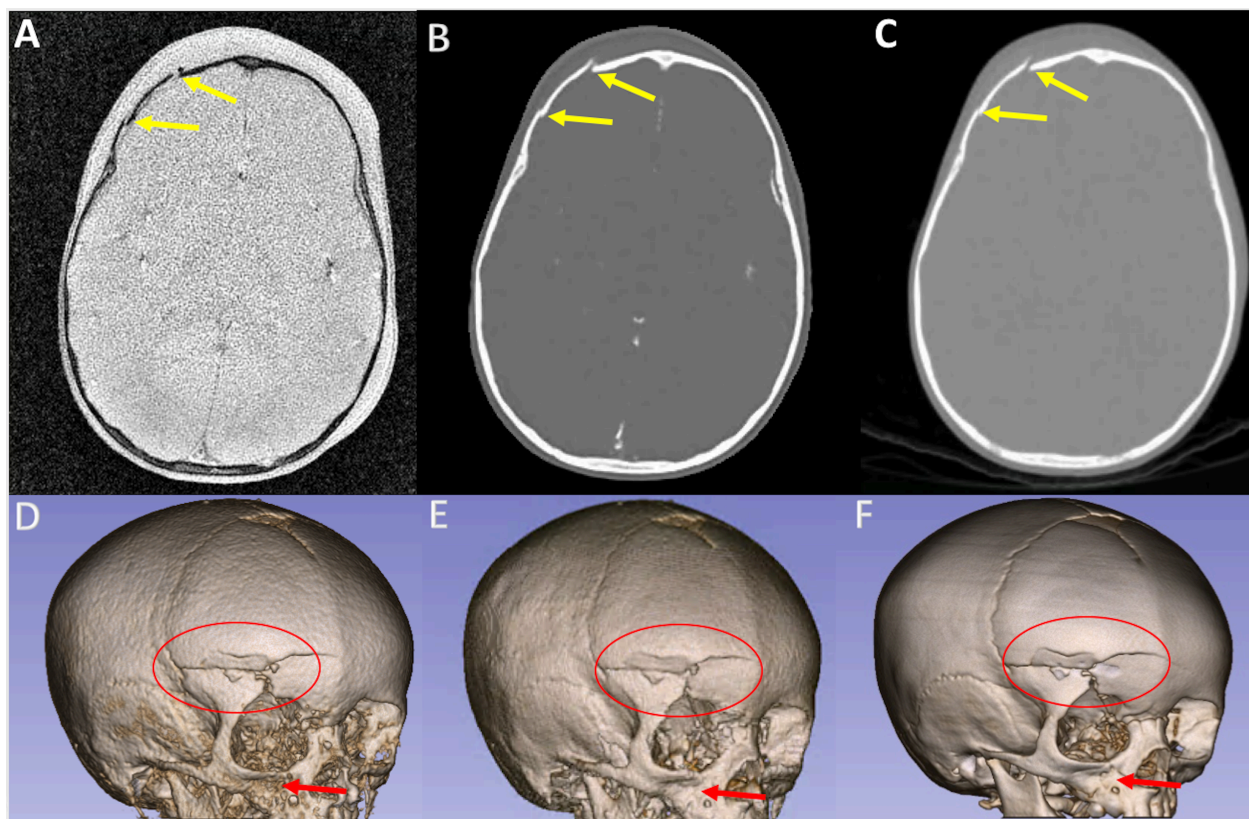


Figure 2.9. Example MR (A), pCT<sub>Com</sub> (B), and CT (C) images from a trauma patient (1.6-year-old, female) with fractures marked by yellow arrows, and the corresponding 3D surface rendered cranial bone images of iMR (D), pCT<sub>Com</sub> (E), and CT (F). A fracture is marked by a red circle. The



proposed MR-HiPCB reduced the noise in the surface-rendered bone images (E) compared to that of the iMR image (D) (marked by red arrows).

## 2.4 Discussion and Summary

Previously developed deep learning pCT methods have been primarily focused on generating pCT for adults without a need to resolve fine bony structures (26-34). To our knowledge, the proposed MR-HiPCB is the first method to create pCT from MRI at sub-millimeter resolution ( $0.3 \times 0.3 \times 0.5 \text{ mm}^3$ ) to identify small bony structures for diagnosing cranial bone abnormality in pediatric participants with head trauma or craniosynostosis. The proposed MR-HiPCB method consists of three ResUNet networks to achieve high accuracy in both bones and soft tissues.

The network structures of NetWH and NetBA are identical. The differences are the training samples used in training these two networks (Figure 2.1). Since bone and air regions only occupy a small fraction of the total head volume, their representations were enriched in NetBA to improve pCT in these regions at the expense of reducing performance in brain regions. We have demonstrated that  $\text{pCT}_{\text{NetWH}}$  performed better in the intracranial regions, while  $\text{pCT}_{\text{NetBA}}$  was more accurate in cranial bone regions.  $\text{pCT}_{\text{Com}}$  takes advantage of these two networks by combining the brain regions from  $\text{pCT}_{\text{NetWH}}$  and non-brain regions from  $\text{pCT}_{\text{NetBA}}$ .  $\text{pCT}_{\text{Com}}$  allows us to discern detail of bony structures at high resolution while maintaining overall accuracy. The  $\text{pCT}_{\text{Com}}$  has the lowest MAE in the whole head. Moreover, MAE of  $\text{pCT}_{\text{Com}}$  is lower than  $\text{pCT}_{\text{NetWH}}$ , but similar to  $\text{pCT}_{\text{NetBA}}$  within the cranial bone. The  $\text{pCT}_{\text{Com}}$  has a significantly higher bone DSC than  $\text{pCT}_{\text{NetWH}}$ ,  $\text{pCT}_{\text{NetBA}}$ , and iMR. The  $\text{pCT}_{\text{Com}}$  demonstrated

similar visibility of sutures and fractures compared to CT. Moreover, it took several minutes to generate high-resolution pCT after the neural networks were trained.

When compared to adults, young children have thinner and less dense cranial bone, resulting in diminishing image contrast between bone and surrounding soft tissues. Moreover, cranial bone density and size changes rapidly due to growth during the early years of life. The cranial bone volume doubles in size by the first 6 months, triples by 2.5 years of age, and is 90% complete by 5 years of age (35,36). Despite manually choosing a participant-specific signal threshold, a signal intensity-based approach iMR performed poorly in segmenting bone, particularly in younger participants (Figure 2.2D). In contrast, MR-HiPCB used not only signal intensities but also multi-scale high-level context information offered by ResUNet to address these challenges. pCT<sub>Com</sub> improved bone segmentation across all ages with more pronounced improvement in young children. Notably, DSC of pCT<sub>Com</sub> was still lower in younger participants than in older participants. It may be explained by fewer training samples from participants younger than 5 years old. Separate networks for different age groups can be trained independently; however, each network training needs a large sample size. Alternatively, general pCT networks may be trained using images across a wide age range followed by transfer learning to provide age-specific networks to further improve performance (55).

In this study, most participants (80%) were not sedated. We have demonstrated that high-quality pCT can be achieved in pediatric patients without sedation. Figure 2.9 showed that pCT networks trained on images from 3T scanners might be generalized to images acquired using a

1.5T MR scanner. Good quality pCT<sub>Com</sub> images were generated despite using the low-quality 1.5T MR images as the input. DSC and MAE from the 1.5T pCT<sub>Com</sub> were comparable to those from the 3T in participants with a similar age range, supporting the feasibility of MR-HiPCB at 1.5T. More data will be needed in the future to further examine the performance of MR-HiPCB at 1.5T MR scanner.

Our study had several limitations. First, MR images were interpolated to match the higher spatial resolution of the CT images (0.30 x 0.30 x 0.50 mm<sup>3</sup>). The original lower resolution MR image may result in blurrier pCT images than CT. Moreover, despite using NetBA to improve estimation in bone, a deep learning-based approach may result in additional blurriness in the pCT images. Second, the MRI acquisition time (~5 minutes) is much longer than that of the CT scan (seconds), which may negatively impact the clinical adoption of the proposed method. Last, the choice of segmentation algorithm may affect DSC. We used a threshold of 200 HU to segment bone from the CT and all pCT images. Other bone segmentation methods, for example K-means clustering, might change the cranial bone masks, leading to different DSC values.

The long-term goal of this study is to develop an MR-based cranial bone imaging method as a radiation-free alternative to CT imaging for evaluating cranial fractures and cranial suture patency in a clinical setting. A clinical evaluation will need to be performed to assess the clinical utility of the pCT images in the future. New methods to accelerate MR acquisition should also be developed to facilitate clinical translation.

In conclusion, we have developed a fast, robust, and fully automated method to synthesize 3D high-resolution pCT using MR images for pediatric patients. The proposed MR-HiPCB method is promising in providing CT-equivalent information for clinical diagnosis and post-treatment follow-up for pediatric patients with head trauma or craniosynostosis. This MR-HiPCB method may profoundly impact pediatric health by minimizing patient risks caused by ionizing radiation from CT imaging.

## **References**

1. Dorfman AL, Fazel R, Einstein AJ, Applegate KE, Krumholz HM, Wang Y, Christodoulou E, Chen J, Sanchez R, Nallamothu BK. Use of medical imaging procedures with ionizing radiation in children: a population-based study. *Archives of pediatrics & adolescent medicine* 2011;165(5):458-464.
2. Miglioretti DL, Johnson E, Williams A, Greenlee RT, Weinmann S, Solberg LI, Feigelson HS, Roblin D, Flynn MJ, Vanneman N. The use of computed tomography in pediatrics and the associated radiation exposure and estimated cancer risk. *JAMA pediatrics* 2013;167(8):700-707.
3. Lindberg DM, Stence NV, Grubenhoff JA, Lewis T, Mirsky DM, Miller AL, O'Neill BR, Grice K, Mourani PM, Runyan DK. Feasibility and accuracy of fast MRI versus CT for traumatic brain injury in young children. *Pediatrics* 2019; 144(4):20190419.
4. Burstein B, Upton JE, Terra HF, Neuman MI. Use of CT for head trauma: 2007–2015. *Pediatrics* 2018;142(4):20180814.
5. Schneier AJ, Shields BJ, Hostetler SG, Xiang H, Smith GA. Incidence of pediatric traumatic brain injury and associated hospital resource utilization in the United States. *Pediatrics* 2006;118(2):483-492.
6. French LR, Jackson IT, Melton III LJ. A population-based study of craniosynostosis. *Journal of clinical epidemiology* 1990;43(1):69-73.
7. Mitchell L, Kitley C, Armitage T, Krasnokutsky M, Rooks V. Normal sagittal and coronal suture widths by using CT imaging. *American journal of neuroradiology* 2011;32(10):1801-1805.
8. Brenner DJ, Elliston CD, Hall EJ, Berdon WE. Estimates of the cancer risks from pediatric CT radiation are not merely theoretical: Comment on “Point/Counterpoint: In x-ray computed tomography, technique factors should be selected appropriate to patient size. Against the Proposition”[*Med. Phys.* 28, 1543–1545 (2001)]. *Medical physics* 2001;28(11):2387-2388.
9. Parker L. Computed tomography scanning in children: radiation risks. *Pediatric hematology and oncology* 2001;18(5):307-308.
10. Pearce MS, Salotti JA, Little MP, McHugh K, Lee C, Kim KP, Howe NL, Ronckers CM, Rajaraman P, Craft AW. Radiation exposure from CT scans in childhood and subsequent risk of leukaemia and brain tumours: a retrospective cohort study. *The Lancet* 2012;380(9840):499-505.
11. Smyth MD, Narayan P, Tubbs RS, Leonard JR, Park T, Loukas M, Grabb PA. Cumulative diagnostic radiation exposure in children with ventriculoperitoneal shunts: a review. *Child's Nervous System* 2008;24(4):493-497.

12. Brenner DJ, Eric J. Hall." Computed tomography—an increasing source of radiation exposure.". *New England Journal of Medicine* 2007;357(22):2277-2284.
13. Eley KA, McIntyre A, Watt-Smith SR, Golding SJ. "Black bone" MRI: a partial flip angle technique for radiation reduction in craniofacial imaging. *The British journal of radiology* 2012;85(1011):272-278.
14. Eley KA, Watt-Smith SR, Sheerin F, Golding SJ. "Black Bone" MRI: a potential alternative to CT with three-dimensional reconstruction of the craniofacial skeleton in the diagnosis of craniosynostosis. *European radiology* 2014;24(10):2417-2426.
15. Dremmen M, Wagner M, Bosemani T, Tekes A, Agostino D, Day E, Soares B, Huisman T. Does the addition of a "black bone" sequence to a fast multisequence trauma MR protocol allow MRI to replace CT after traumatic brain injury in children? *American Journal of Neuroradiology* 2017;38(11):2187-2192.
16. Kralik SF, Supakul N, Wu IC, Delso G, Radhakrishnan R, Ho CY, Eley KA. Black bone MRI with 3D reconstruction for the detection of skull fractures in children with suspected abusive head trauma. *Neuroradiology* 2019;61(1):81-87.
17. Eley KA, Watt-Smith SR, Golding SJ. Three-dimensional reconstruction of the craniofacial skeleton with gradient echo magnetic resonance imaging ("black bone"): what is currently possible? *Journal of Craniofacial Surgery* 2017;28(2):463-467.
18. Chen Y, Juttukonda M, Su Y, Benzinger T, Rubin BG, Lee YZ, Lin W, Shen D, Lalush D, An H. Probabilistic air segmentation and sparse regression estimated pseudo CT for PET/MR attenuation correction. *Radiology* 2015;275(2):562-569.
19. Juttukonda MR, Mersereau BG, Chen Y, Su Y, Rubin BG, Benzinger TL, Lalush DS, An H. MR-based attenuation correction for PET/MRI neurological studies with continuous-valued attenuation coefficients for bone through a conversion from R2\* to CT-Hounsfield units. *Neuroimage* 2015;112:160-168.
20. Hofmann M, Steinke F, Scheel V, Charpiat G, Farquhar J, Aschoff P, Brady M, Schölkopf B, Pichler BJ. MRI-based attenuation correction for PET/MRI: a novel approach combining pattern recognition and atlas registration. *Journal of nuclear medicine* 2008;49(11):1875-1883.
21. Larsson A, Johansson A, Axelsson J, Nyholm T, Asklund T, Riklund K, Karlsson M. Evaluation of an attenuation correction method for PET/MR imaging of the head based on substitute CT images. *Magnetic Resonance Materials in Physics, Biology and Medicine* 2013;26(1):127-136.
22. Navalpakkam BK, Braun H, Kuwert T, Quick HH. Magnetic resonance-based attenuation correction for PET/MR hybrid imaging using continuous valued attenuation maps. *Investigative radiology* 2013;48(5):323-332.

23. Huynh T, Gao Y, Kang J, Wang L, Zhang P, Lian J, Shen D. Estimating CT image from MRI data using structured random forest and auto-context model. *IEEE transactions on medical imaging* 2015;35(1):174-183.
24. Johansson A, Karlsson M, Nyholm T. CT substitute derived from MRI sequences with ultrashort echo time. *Medical physics* 2011;38(5):2708-2714.
25. Johansson A, Garpebring A, Asklund T, Nyholm T. CT substitutes derived from MR images reconstructed with parallel imaging. *Medical physics* 2014;41(8Part1):082302.
26. Liu F, Jang H, Kijowski R, Bradshaw T, McMillan AB. Deep learning MR imaging-based attenuation correction for PET/MR imaging. *Radiology* 2018;286(2):676-684.
27. Jang H, Liu F, Zhao G, Bradshaw T, McMillan AB. Deep learning based MRAC using rapid ultrashort echo time imaging. *Medical physics* 2018;45(8):3697-3704.
28. Gong K, Yang J, Kim K, El Fakhri G, Seo Y, Li Q. Attenuation correction for brain PET imaging using deep neural network based on Dixon and ZTE MR images. *Physics in Medicine & Biology* 2018;63(12):125011.
29. Blanc-Durand P, Khalifé M, Sgard B, Kaushik S, Soret M, Tiss A, El Fakhri G, Habert M-O, Wiesinger F, Kas A. Attenuation correction using 3D deep convolutional neural network for brain 18F-FDG PET/MR: Comparison with Atlas, ZTE and CT based attenuation correction. *PloS one* 2019;14(10):e0223141.
30. Ladefoged CN, Marner L, Hindsholm A, Law I, Højgaard L, Andersen FL. Deep learning based attenuation correction of PET/MRI in pediatric brain tumor patients: evaluation in a clinical setting. *Frontiers in neuroscience* 2019;12:1005.
31. Nie D, Trullo R, Lian J, Wang L, Petitjean C, Ruan S, Wang Q, Shen D. Medical image synthesis with deep convolutional adversarial networks. *IEEE Transactions on Biomedical Engineering* 2018;65(12):2720-2730.
32. Han X. MR-based synthetic CT generation using a deep convolutional neural network method. *Medical physics* 2017;44(4):1408-1419.
33. Arabi H, Zeng G, Zheng G, Zaidi H. Novel adversarial semantic structure deep learning for MRI-guided attenuation correction in brain PET/MRI. *European journal of nuclear medicine and molecular imaging* 2019;46(13):2746-2759.
34. Chen Y, Ying C, Binkley MM, Juttukonda MR, Flores S, Laforest R, Benzinger TL, An H. Deep learning-based T1-enhanced selection of linear attenuation coefficients (DL-TESLA) for PET/MR attenuation correction in dementia neuroimaging. *Magnetic resonance in medicine* 2021;86(1):499-513.

35. Kamdar MR, Gomez RA, Ascherman JA. Intracranial volumes in a large series of healthy children. *Plastic and reconstructive surgery* 2009;124(6):2072-2075.
36. Ghosh TD, Skolnick G, Nguyen DC, Sun H, Patel K, Smyth MD, Woo AS. Calvarial thickness and diploic space development in children with sagittal synostosis as assessed by computed tomography. *Journal of Craniofacial Surgery* 2014;25(3):1050-1055.
37. Pipe JG. Motion correction with PROPELLER MRI: application to head motion and free-breathing cardiac imaging. *Magnetic Resonance in Medicine: An Official Journal of the International Society for Magnetic Resonance in Medicine* 1999;42(5):963-969.
38. Vaillant G, Prieto C, Kolbitsch C, Penney G, Schaeffter T. Retrospective rigid motion correction in k-space for segmented radial MRI. *IEEE transactions on medical imaging* 2013;33(1):1-10.
39. Grimm R, Fürst S, Souvatzoglou M, Forman C, Hutter J, Dregely I, Ziegler SI, Kiefer B, Hornegger J, Block KT. Self-gated MRI motion modeling for respiratory motion compensation in integrated PET/MRI. *Medical image analysis* 2015;19(1):110-120.
40. Feng L, Axel L, Chandarana H, Block KT, Sodickson DK, Otazo R. XD-GRASP: golden-angle radial MRI with reconstruction of extra motion-state dimensions using compressed sensing. *Magnetic resonance in medicine* 2016;75(2):775-788.
41. Eldeniz C, Fraum T, Salter A, Chen Y, Gach HM, Parikh PJ, Fowler KJ, An H. Consistently-Acquired Projections for Tuned and Robust Estimation—A self-navigated respiratory motion correction approach. *Investigative radiology* 2018;53(5):293.
42. Paul J, Divkovic E, Wundrak S, Bernhardt P, Rottbauer W, Neumann H, Rasche V. High-resolution respiratory self-gated golden angle cardiac MRI: comparison of self-gating methods in combination with k-t SPARSE SENSE. *Magnetic Resonance in Medicine* 2015;73(1):292-298.
43. Haacke EM, Patrick JL. Reducing motion artifacts in two-dimensional Fourier transform imaging. *Magnetic resonance imaging* 1986;4(4):359-376.
44. Fedorov A, Beichel R, Kalpathy-Cramer J, Finet J, Fillion-Robin J-C, Pujol S, Bauer C, Jennings D, Fennessy F, Sonka M. 3D Slicer as an image computing platform for the Quantitative Imaging Network. *Magnetic resonance imaging* 2012;30(9):1323-1341.
45. Tustison N, Avants B, Cook Pea. N4ITK: improved N3 bias correction. *IEEE Trans Med Imaging* 2010;1310-1320.
46. Vese LA, Chan TF. A multiphase level set framework for image segmentation using the Mumford and Shah model. *International journal of computer vision* 2002;50(3):271-293.



47. Jenkinson M, Smith S. A global optimisation method for robust affine registration of brain images. *Medical image analysis* 2001;5(2):143-156.
48. Patel KB, Eldeniz C, Skolnick GB, Jammalamadaka U, Commean PK, Goyal MS, Smyth MD, An H. 3D pediatric cranial bone imaging using high-resolution MRI for visualizing cranial sutures: a pilot study. *Journal of Neurosurgery: Pediatrics* 2020;26(3):311-317.
49. Ronneberger O, Fischer P, Brox T. U-net: Convolutional networks for biomedical image segmentation. 2015:234-241.
50. He K, Zhang X, Ren S, Sun J. Deep residual learning for image recognition. *IEEE Conference on Computer Vision and Pattern Recognition* 2016:770-778.
51. Zhang Z, Liu Q, Wang Y. Road extraction by deep residual u-net. *IEEE Geoscience and Remote Sensing Letters* 2018;15(5):749-753.
52. Dabov K, Foi A, Katkovnik V, Egiazarian K. Image denoising by sparse 3-D transform-domain collaborative filtering. *IEEE Transactions on image processing* 2007;16(8):2080-2095.
53. Ladefoged C, Benoit D, Law I, Holm S, Hojgaard L, Hansen AE, Andersen FL. PET/MR attenuation correction in brain imaging using a continuous bone signal derived from UTE. *EJNMMI Phys* 2015;2(Suppl 1):A39.
54. Paszke A, Gross S, Massa F. Pytorch: An imperative style, high-performance deep learning library. *Advances in Neural Information Processing Systems* 2019:8024-8035
55. Ladefoged CN, Hansen AE, Henriksen OM, Bruun FJ, Eikenes L, Oen SK, Karlberg A, Hojgaard L, Law I, Andersen FL. AI-driven attenuation correction for brain PET/MRI: Clinical evaluation of a dementia cohort and importance of the training group size. *NeuroImage* 2020;222:117221.

# **Chapter 3: Self-Supervised and Physics-Guided Deep Learning MR Reconstruction: Weighting k-Space Sampling Density in Network Training Loss (wkDeLo) in an Unrolled Network**

## **3.1 Introduction**

High-resolution MRI acquisition with sub-millimeter voxel size and whole head coverage takes several minutes to acquire (2-4). 3D high-resolution cranial MRI is a safe alternative to CT for pediatric patients with cranial anomalies without ionizing radiation (5-11). The long acquisition time is challenging for the pediatric patient due to the high likelihood of motion for children young children and limits clinical adoption of MR cranial bone imaging. However, a short MRI acquisition cannot meet the Nyquist k-space acquisition criterion, resulting in reconstruction artifacts and high noise. Hence, an imaging reconstruction method to provide high-quality images using under-sampled data is desired to reduce MR acquisition time.

To overcome these challenges, compressed sensing (CS) reconstruction has been employed to reconstruct undersampled MR data (12,13). A CS method utilizes an iterative algorithm by minimizing a cost function consisting of a data consistency term and prior-based regularization.

(14-23). However, CS becomes less effective when data is severely under-sampled (24,25). Furthermore, CS reconstruction is computationally time-consuming and usually necessitates empirical fine-tuning of regularization parameters. Emerging techniques based on fast self-tuning show promise for principled parameter selection (26,27). More recently, deep learning (DL) has been explored for MR image reconstruction (28-39). Iterative-based algorithms that alternate between data-consistency enforcement and pre-trained convolutional neural network (CNN) denoisers are an alternative to the direct inversion approach (40-44). More recently, Model-based reconstruction with Deep Learned Priors (MoDL) combines the strength of model-based reconstruction approaches with the power of deep learning (25,32,45-52). The network is made up of a combination of CNN blocks that capture information about the data set and data consistency (DC) blocks that promote measurement consistency. The end-to-end training technique gives a significant boost in performance over using pre-trained denoisers since the network parameters are trained for the specific task of image recovery. These methods use an iterative reconstruction process to solve the objective method for a set number of iterations. The unrolled network alternates between data consistency (DC) and regularization, with the regularization being done implicitly via a neural network (32,33). These unrolled networks are then trained end-to-end with a loss function that measures similarity to a reference image and parameters may differ over unrolled iterations (32,45,48) or may be shared among them (46,50,55). Recently, the Self-supervised learning via data under-sampling (SSDU) method is introduced for physics-guided deep learning reconstruction divides available kspace data into two disjoint sets, one of which is used in the data consistency (DC) units in the unrolled network and the other is used to define the loss for training. SSDU method achieved comparable results to

the supervised approach trained on fully sampled data, despite having only been trained on under sampled data.

In many accelerated MR imaging approaches, variable density k-space samplings have been widely utilized. For example, k-space center are usually fully acquired as auto-calibrated signal (ACS) lines, while outer k-space were covered sparsely in Cartesian sampling scheme .

Moreover, radial and spiral k-space coverage, which cover k-space center more densely than outer k-space, have also been widely used in MRI . However, existing DL reconstruction-based methods, including SSDU, have not accounted for k-space density variations in physics-guided deep learning MRI reconstruction.

In this study, we developed a self-supervised and physics-guided deep learning method by weighting k-space sampling Density in network training Loss (wkDeLo). The goal was to regularize the forward Fourier model by using the weighted k-space deep learning prior with unrolling structure to shorten the MRI acquisition time by using a 16% Nyquist rate (1 minute) (an acceleration rate of 6.25).

We have applied our proposed wkDeLo method to MR data acquired using a golden angle stack-of-stars sequence to accelerate MR acquisition. Moreover, we have also reconstructed images using the same unrolled network structure but without accounting for the k-space sampling density variations using a uniform weighted k-space in the training loss (un-wkDeLo) for comparison. Furthermore, we adopted the well-accepted SSDU as a baseline method reference. Using the images reconstructed from a 5-min scan as the gold standard, we computed the structural similarity index measure (SSIM) and peak signal-to-noise ratio (PSNR) for reconstructed images from 1-min k-space data using SSDU, un-wkDeLo, and wkDeLo. 3D MR

cranial bone imaging were generated using images reconstructed using the SSDU, un-wkDeLo, and wkDeLo methods.

## **3.2 MATERIALS AND METHODS**

### **3.2.1 Study Cohort**

St. Louis Children's Hospital pediatric patients (ages three days to 17 years old) diagnosed with head trauma or craniosynostosis were recruited for this study.

### **3.2.2 Image Acquisition**

A 3T (Prisma or VIDA) MR scanner (Siemens Healthineers, Erlangen, Germany) was used to scan 32 participants. A Fast Low-Angle Shot (FLASH) Golden-Angle 3D stack-of-stars radial Volumetric Interpolated Breath-hold Examination sequence (GA-VIBE) was utilized to obtain the MR images because of its motion resilience. The following imaging characteristics were used: TR/TE = 4.84ms/2.47 ms, field of view = 192 mm, Bandwidth = 410 Hz/pixel, 224 slices per slab, transverse orientation, Flip angle = 3°, acquisition matrix = 320 × 320, voxel size 0.6 x 0.6 x 0.8 mm<sup>3</sup> and total number of radial lines = 400 for a scan duration of 5 minutes and 4 seconds.

### **3.2.3 Self-Supervised and Physics-Guided Deep Learning Reconstruction Using an Unrolled Network**

A physics-guided reconstruction regularized by a deep learning prior can be employed to reconstruct under-sampled MR k-space data. This method reconstructs images by iteratively minimizing a loss function as depicted below:

$$I = \operatorname{argmin}_I \sum_i \sum_j \left\| H_{i,j} \cdot I - K_{i,j} \right\|_2^2 + h(I) \quad (1)$$

$$h(I) = \lambda_m / 2 \|I^T (I - R_\theta(I))\|_1. \quad (2)$$

where the operator  $H_{i,j} = F \cdot C_j$ ;  $F$  is the forward Fourier (NUFFT) operator;  $C_j$  is the coil sensitivity for Coil  $j$ ;  $I$  is the to-be-determined image;  $K_{i,j}$  is the acquired k-space data for spoke  $i$  with coil  $j$ .

The first term of the cost function is to ensure data consistency (DC), while the second term  $h(I)$  in Eq (2) is a regularization term using a convolution neural network  $R_\theta(I)$ .  $I^T$  is the transpose of  $I$  and  $\lambda_m$  is the regularization coefficient that balances the tradeoff between data consistency and regularization.  $\lambda_m$  is learned during the training of the unrolled network.  $R_\theta$  is a convolution neural network with dual-channel inputs for real and imaginary parts of the complex images. The complex inputs are used because noise has a zero-mean Gaussian distribution.

The unrolled network architecture is demonstrated which consists of the DC and  $D_\theta(I) = I - R_\theta(I)$  blocks in Fig. 3.1. During the training, the k-space data of a 400 radial spokes (5 min scan) can be divided into two disjoint data sets: the first 80 radial spokes (1 min) as  $K_{\text{input}}$  and the remaining 320 spokes (4 minutes) as  $K_{\text{target}}$ . The full Nyquist sampling rate for the radial scan needs 502 spokes. 80 and 320 spokes correspond to 16% and 64% of the Nyquist sampling rate, respectively.  $K_{\text{input}}$  is transformed into the spatial domain ( $I_{\text{input}}$ ) via an inverse Fourier transform  $H^\dagger$ . The complex  $K_{\text{input}}$  and  $I_{\text{input}}$  were then fed into the unrolled network for  $P$  iterations.  $I^P$  is the output of the unrolled network. A Forward Fourier transform  $H$  is applied to  $I^P$  to transform it to k-space and sampled it at the same k-space locations as  $K_{\text{target}}$ .

### 3.2.4 weighting k-Space Sampling Density in the Training Loss Function

A L1-loss is constructed as the difference between  $H I^P$  and  $K_{\text{target}}$  and then weighted by k-space sampling density as depicted in Equation (3).

$$\text{argmin} \sum || H_j I^P - K_{\text{target}} ||_W \quad (3)$$

where  $W$  is the weighting to account for k-space sampling density variations.  $H_j = S F C_j$  where  $F$  is the forward Fourier (NUFFT) operator;  $C_j$  is the coil sensitivity for Coil  $j$  and  $S$  is the sampling function.  $S^n$  is normalized of  $S$  which is  $S_i^n = S_i / \sum_N S_i$ , and then we define  $W$  with each elements of  $W_i = 1/S_i^n$  at each sampling location  $i$ ,  $N$  is the total number of radial sampling. We apply small weights in the low k-space and large weights in the outer k-space. This weighted L1-loss is minimized through training.

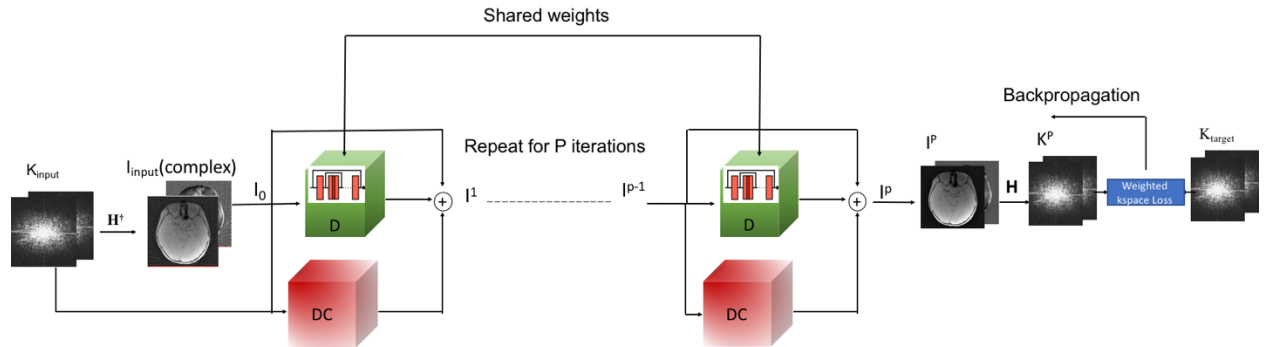


Fig1.Unfolding network structure

Fig 3.1. Unfolding network structure

### 3.2.5 Network and Training Details

The data consistency in the unrolled network was implemented with the conjugate gradient method for solving Equation 2, which itself was unrolled for 5 iterations ( $P=5$  in Fig. 3.1). The neural network in Equation 2 was implemented using a CNN based on a ResUNet structure similar to the previously introduced U-RED (55,56). The learned operator blocks within U-RED ( $R_\theta$ ) share their weights across iterations. They are trained in an end-to-end manner by accounting for the data consistency layers. This CNN consists of a layer of input and output convolution layers, and 7 residual blocks with skip connections that facilitate information flow during network training. Each residual block consisted of convolutional layers, followed by a rectified linear (RELU) unit (55,56). All layers had a kernel size of  $3 \times 3$  and 64 channels. This ResUNet CNN had a total of 1,166,820 trainable parameters, which were shared across the unrolled iterations. In total we had 32 subjects, each time 10 subjects were randomly selected for training, and 4 subjects were used for validation and the remaining were used for testing,

PyTorch 1.8.2 was used to implement the deep ResUNet unrolled framework using a computer with an Intel Xeon Gold 6216 processor and an NVIDIA Tesla A100 graphics processing unit. The training and validation procedure took about two days (GPU). Using a single GPU, testing took less than a minute.

### 3.2.6 Baseline Methods

We compared the wkDeLo to two other DL-based reconstruction methods. To evaluate the effect of k-space sampling density weighted, we used the exactly same unrolling network but without accounting for k-space sampling density in network training Loss. In other words, a uniform



weighted is used in the training loss (un-wkDeLo).  $W$  is equal to the identity matrix ( $I$ ) in Equation (3).

We adopted and implemented the SSDU method as another baseline method. SSDU is a self-supervised method using a deep unrolling network. Similar to the published SSDU method, we divided k-space MRI data into two disjoint subsets and uses one set with 32 spokes for data consistency layer and the other set with 48 spokes in the regularization layer (57).

### **3.2.7 Cranial Bone 3D Reconstruction**

The bias-field corrected MR images were inverted and masked with the head binary mask, resulting in high and low signal intensities for skull bone and soft tissue, respectively. Using the 3D Slicer software, a global intensity threshold was manually determined after the intensity inversion to create a 3D skull bone rendering (10,11).

### **3.2.8 Performance Evaluations**

The 5-minute data (400 spokes) reconstructed using multi-coil non-uniform fast Fourier transformation (MCNUFFT) was used as the gold standard. The first 1-minute of MR data from each subject was reconstructed using the wkDeLo, un-wkDeLo, and SSDU methods. Using the 5-min MCNUFFT scan as the gold standard, we calculated the structural similarity index measure (SSIM) and peak signal to noise ratio (PSNR) for the 1-min wkDeLo, 1-min un-wkDeLo, and the 1-min SSDU reconstructed images.

One-way ANOVA followed by Dunnett's multiple comparisons test was performed to compare the SSIM and PSNR for the 1-min SSDU, 1-min un-wkDeLo, and 1-min wkDeLo, using GraphPad Prism (version 9.0.0, GraphPad Software, San Diego, California USA).

### 3.3 Results

MCNUFFT, SSDU, un-wkDeLo, and wkDeLo were used to reconstruct 1-minute k-space data.

The 5-min MCNUFFT images (3.2E) were considered as the gold standard reference. 1-min MCNUFFT has high noise and reconstruction artifacts (Figure 3.2A), 1-min SSDU reduced noise and artifacts compared to 1-min MCNUFFT, but there are still visible artifacts compared to 5-min MCNUFFT marked by the red arrow. 1-min un-wkDeLo has further reduced noise and artifacts but at the expense of image sharpness, resulting in less visibility of small structures (Figure 3.2C). The proposed wkDeLo is effective in reducing artifacts and noise, while still preserving fine details of the structures (Figure 3.2D). Difference images compared to the reference image are shown in the second row (Figure 3.2 F, G, H, and I)

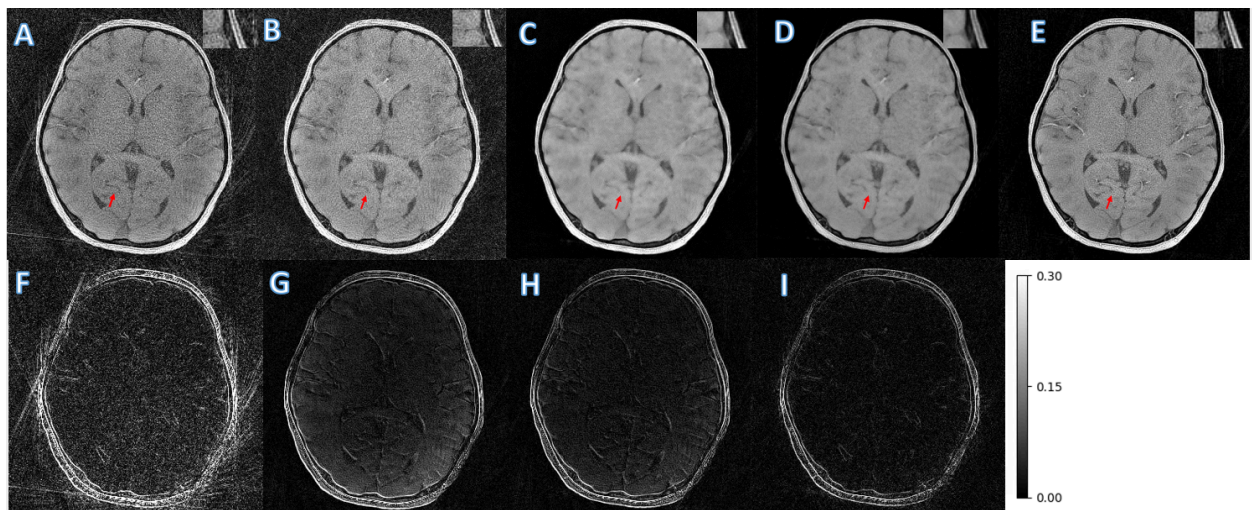


Fig 3.2. MR images 1 min MCNUFFT (A) , 1 min SSDU (B), 1 min un-wkDeLo (C), 1 min wkDeLo (D), and 5 min MCNUFFT reconstruction for 5.6 years old trauma patient, and the corresponding difference images ( $|1 \text{ min MCNUFFT} - 5 \text{ min MCNUFFT}|$ ) (F), ( $|1 \text{ min SSDU} - 5 \text{ min MCNUFFT}|$ ) (G), and ( $|1 \text{ min un-wkDeLo} - 5 \text{ min MCNUFFT}|$ ) (H), ( $|1 \text{ min wkDeLo} - 5 \text{ min MCNUFFT}|$ ) (I). The difference is  $\times 10$  times.

Similar to Figure 3.2, representative 1-min MCNUFFT (Figure 3.3,3.4A), 1-min SSDU (Figure 3.3,3.4 B), 1-min un-wkDeLo (3.3,3.4 C), 1-min wkDeLo (3.3,3.4 D), 5 min MCNUFFT (3.3,3.4 E) and their difference (second row) images from a 10.1-year-old female and 16.8-year-old male participants were displayed in Figure 3.3 and 3.4. 1-min wkDeLo closely resembled the 5-min MCNUFFT images, and the difference between these two was small. The SSDU approach suffers from visible residual artifacts, with the un-wkDeLo and wkDeLo having fewer artifacts. The un-wkDeLo blurred suture regions (marked in the zoomed-in region in the red rectangular). The wkDeLo image has improved suture visibility compared to un-wkDeLo. The wkDeLo successfully performs reconstruction with an acceleration rate of 6.25x at 16% Nyquist sampling rate.

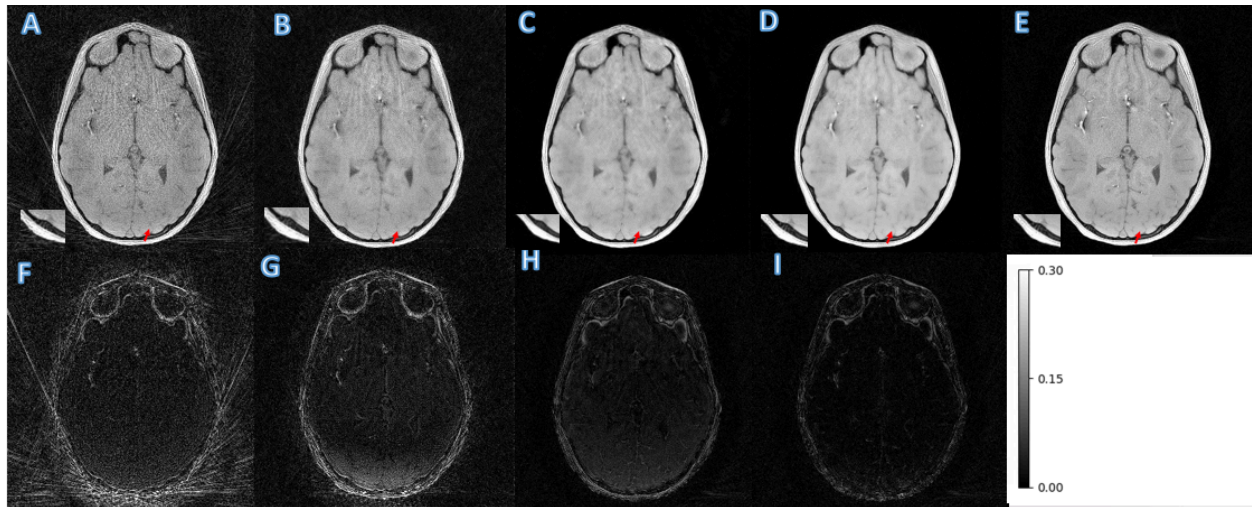


Fig 3.3. MR images 1 min MCNUFFT (A), 1 min SSDU (B), 1 min un-wkDeLo (C), 1 min wkDeLo (D), and 5 min MCNUFFT reconstruction for 10. 1 years old trauma patient, and the corresponding difference images ( $|1 \text{ min MCNUFFT} - 5 \text{ min MCNUFFT}|$ ) (F), ( $|1 \text{ min SSDU} - 5 \text{ min MCNUFFT}|$ ) (G), and ( $|1 \text{ min un-wkDeLo} - 5 \text{ min MCNUFFT}|$ ) (H), ( $|1 \text{ min wkDeLo} - 5 \text{ min MCNUFFT}|$ ) (I). The difference is  $\times 10$  times.

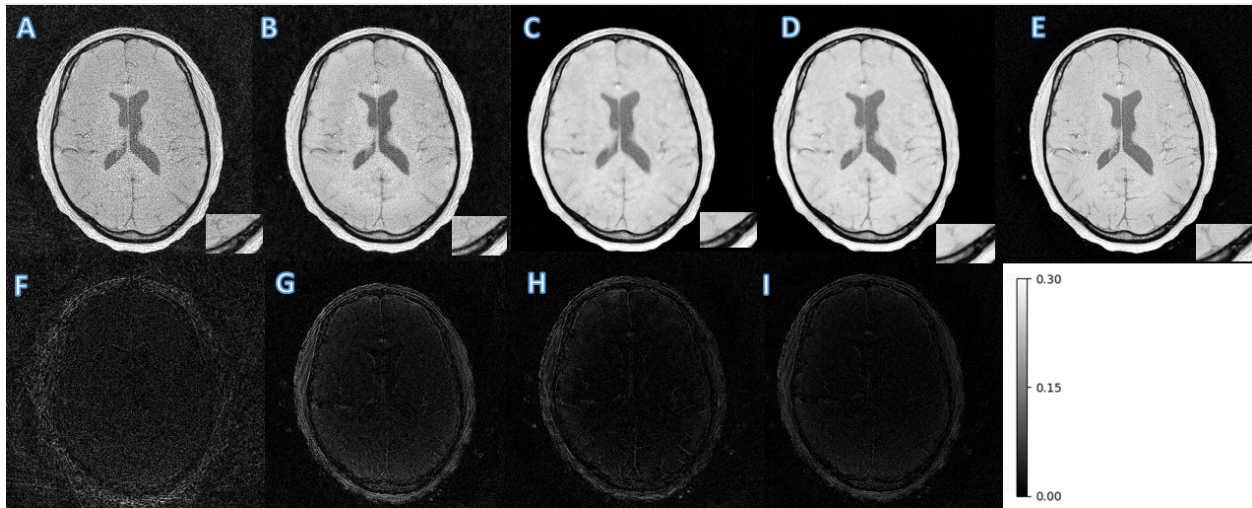


Fig 3.4. MR images 1 min MCNUFFT (A) , 1 min SSDU (B), 1 min un-wkDeLo (C), 1 min wkDeLo (D), and 5 min MCNUFFT reconstruction for 16.8 years old patient, and the



corresponding difference images ( $|1 \text{ min MCNUFFT} - 5 \text{ min MCNUFFT}|$ ) (F), ( $|1 \text{ min SSDU} - 5 \text{ min MCNUFFT}|$ ) (G), and ( $|1 \text{ min un-wkDeLo} - 5 \text{ min MCNUFFT}|$ ) (H), ( $|1 \text{ min wkDeLo} - 5 \text{ min MCNUFFT}|$ ) (I) The difference is  $\times 10$  times.

Volumetric and 3D rendered cranial images from a 4.2 years old female patient with lambdoid and sagittal sutures (Fig 3.5), a 1.8-year-old craniosynostosis participant with an open coronal suture but a closed sagittal suture (Fig 3.6) are shown. The 3D rendered images were created from inverted MR images using 3D Slicer. High-resolution 1-min MR inverted images generated by our proposed method produced similar suture visibility for the coronal and sagittal sutures compared to 5-min MCNUFFT.

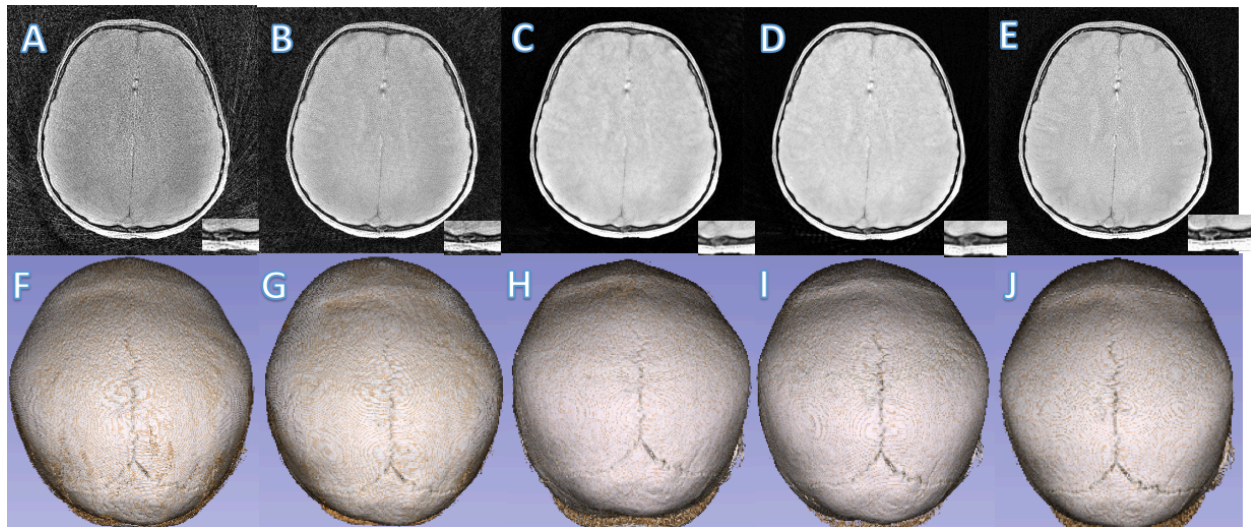


Fig 3.5. MR and rendered images from 1 min MCNUFFT (A, F , 1 min SSDU (B, G), 1 min un-wkDeLo (C, H), 1 min wkDeLo (D,I) , and 5 min MCNUFFT (E, J) reconstruction for craniosynostosis patient.

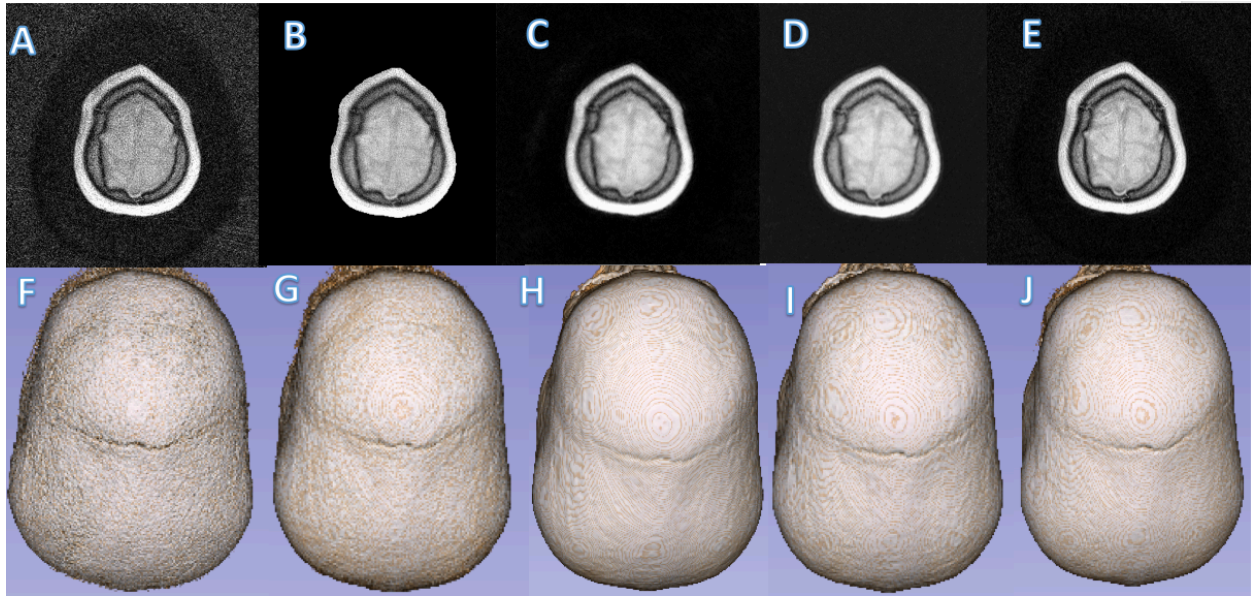


Fig 3.6. MR and rendered images from 1 min MCNUFFT (A, F , 1 min SSDU (B, G), 1 min un-wkDeLo (C, H), 1 min wkDeLo (D,I) , and 5 min MCNUFFT (E, J) reconstruction for craniosynostosis patient.

Figure 3.7 demonstrated an example of volumetric and 3D rendered cranial bone images from a trauma participant with fractures (marked by yellow arrowed and red circles). The skull fractures can be readily identified on 1 min wkDeLo images similar to 5 min MCNUFFT. Moreover, the surface rendered cranial bone images from 1 min s wkDeLo showed much less noise than 1 min SSDU (marked by red arrows), better suture and fracture visualization than 1 min un-wkDeLo

(marked in red circle), and suggesting the proposed method can reduce noise while preserving detailed tiny structures.

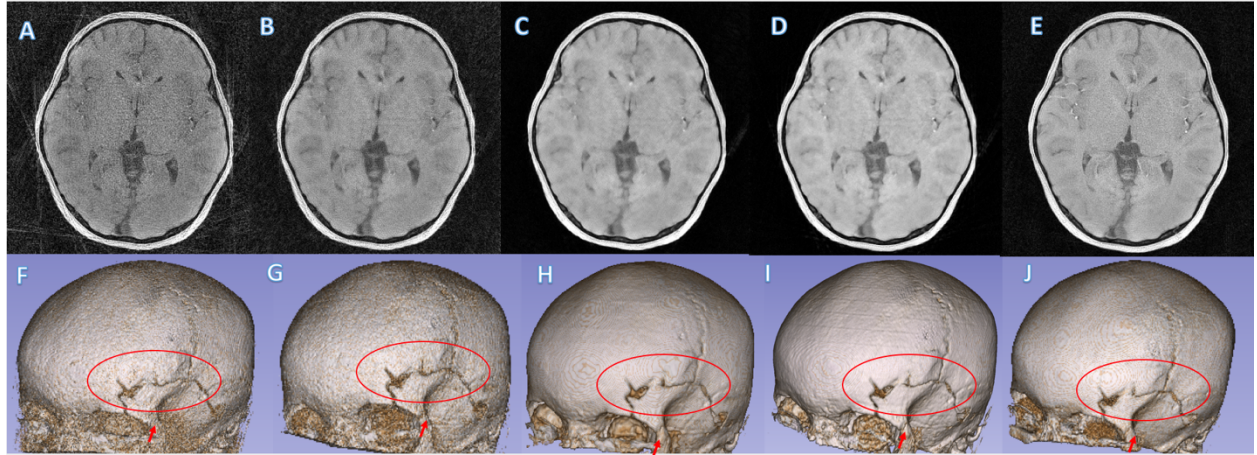


Fig 3.7. MR and rendered images from 1 min MCNUFFT (A, F , 1 min SSDU (B, G), 1 min un-wkDeLo (C, H), 1 min wkDeLo (D,I) , and 5 min MCNUFFTA (E, J) reconstruction for trauma patient. Fracture marked in red circle. The proposed wkDeLo reduced the noise in the surface rendered bone images (I) compared to the un-wkDeLo (H) and SSDU images (G) (marked by red arrows).

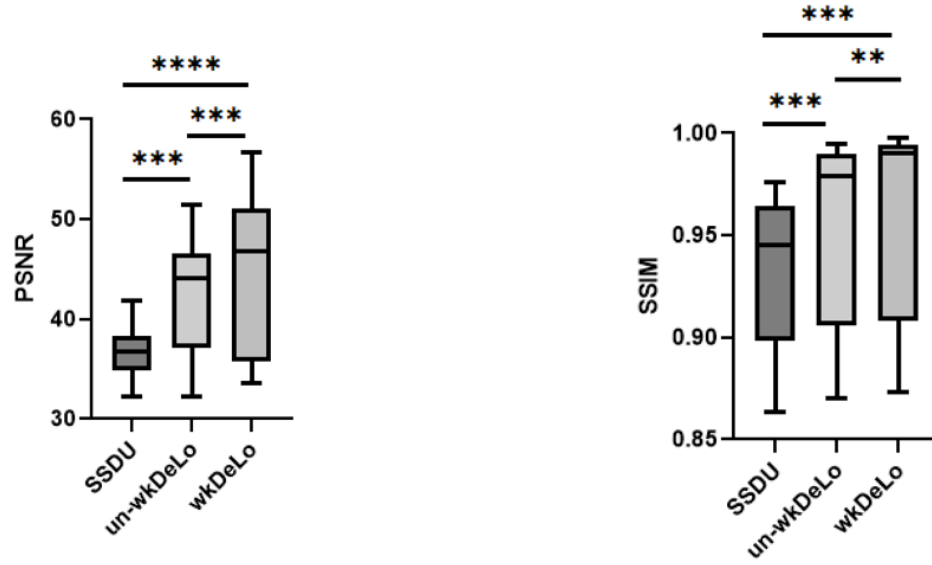


Fig 3.8. PSNR and SSIM using the un-wkDeLo, SSDU and the proposed wkDeLo reconstructions.

The SSIM and PSNR for SSIM, un-wkDeLo, and wkDeLo for all subjects were summarized in a box plot shown in Figure 3.8. The wkDeLo has significantly higher PSNR and SSIM than SSDU and un-wkDeLo ( $P < 0.001$ ).

### 3.4 Discussion and Summary

High-resolution MRI acquisition with sub-millimeter voxel size and whole head coverage may be lengthy. Our current Golden-angle radial MR scan has an acquisition time of 5 minutes. A



long scan reduces compliance in unsedated pediatric patients. However, a short MR acquisition results in under-sampled data, leading to artifacts and high noise. The full Nyquist sampling rate for the radial scan needs 502 spokes. The 5 min (400 spokes) and 1 min (80 spokes) scans correspond to 80% and 16% of Nyquist data, respectively. We developed an MRI reconstruction method using wkDeLo to reduce MR acquisition time. The MR one-minute scan can be used to generate high-resolution images for the application of identifying skull fractures and sutures for pediatric patients. The wkDeLo one-minute scan closely resembled the five minutes MRI scan in terms of image quality. Our results showed that the wkDeLo approach outperforms SSDU and un-wkDeLo, a method without accounting for k-space sampling density. Our results demonstrated that k-space sampling density variation should be considered in network training loss to achieve better MR reconstructions. wkDeLo has the highest SSIM and PSNR. Moreover, wkDeLo images preserve image sharpness, which allows discerning small structure. In this study, all MR scans were acquired using a golden angle stack-of-stars radial acquisitions. Compared to the k-space center, the outer k-space is sparsely covered. The weighted loss function compensated this k-space sampling density variations by giving more weight to high k space in the unrolled network training. The principle of the proposed wkDeLo method can be extended to other k-space sampling schemes, such as spiral or variable density Cartesian acquisitions.

The conventional MCNUFFT reconstruction of a radial k-space usually applies a density compensation of the k-space data before regridding and Fourier transform. Despite a conceptual similarity, the wkDeLo is fundamentally different from the density compensation in the MCNUFFT approach. In MCNUFFT, k-space density weights are applied to the acquired k-

space data directly. In contrast, the k-space density weights are only included in the unrolled network training loss without changing the acquired k-space data.

Our study has a few limitations. The 100% Nyquist fully sampled data were not available in our study. We use 80% Nyquist rate images as an alternative good standard. Due to a lack of ground truth, we did not compare our results to a supervised deep learning-based method. When compared to the 5 minutes data, the 1 min wkDeLo images are still more blurry.

In conclusion, we have developed a fast, robust, and fully automated method to achieve high-resolution MR ( $0.6 \times 0.6 \times 0.8$  mm<sup>3</sup>) with a 1 min acquisition time for pediatric patients. The proposed wkDeLo method is promising in providing high-resolution MR images for clinical diagnosis and post-treatment follow-up for pediatric patients with head trauma or craniosynostosis.

# References

1. Block KT, Uecker M, Frahm J. Undersampled radial MRI with multiple coils. Iterative image reconstruction using a total variation constraint. *Magnetic Resonance in Medicine: An Official Journal of the International Society for Magnetic Resonance in Medicine* 2007;57(6):1086-1098.
2. Griswold MA, Jakob PM, Heidemann RM, Nittka M, Jellus V, Wang J, Kiefer B, Haase A. Generalized autocalibrating partially parallel acquisitions (GRAPPA). *Magnetic Resonance in Medicine: An Official Journal of the International Society for Magnetic Resonance in Medicine* 2002;47(6):1202-1210.
3. Pruessmann KP, Weiger M, Scheidegger MB, Boesiger P. SENSE: sensitivity encoding for fast MRI. *Magnetic Resonance in Medicine: An Official Journal of the International Society for Magnetic Resonance in Medicine* 1999;42(5):952-962.
4. Lustig M, Pauly JM. SPIRiT: iterative self-consistent parallel imaging reconstruction from arbitrary k-space. *Magnetic resonance in medicine* 2010;64(2):457-471.
5. Kralik SF, Supakul N, Wu IC, Delso G, Radhakrishnan R, Ho CY, Eley KA. Black bone MRI with 3D reconstruction for the detection of skull fractures in children with suspected abusive head trauma. *Neuroradiology* 2019;61(1):81-87.
7. Dremmen M, Wagner M, Bosemani T, Tekes A, Agostino D, Day E, Soares B, Huisman T. Does the addition of a “black bone” sequence to a fast multisequence trauma MR protocol allow MRI to replace CT after traumatic brain injury in children? *American Journal of Neuroradiology* 2017;38(11):2187-2192.
8. Eley K, McIntyre A, Watt-Smith S, Golding S. “Black bone” MRI: a partial flip angle technique for radiation reduction in craniofacial imaging. *The British Journal of Radiology* 2012;85(1011):272-278.
9. Eley KA, Watt-Smith SR, Sheerin F, Golding SJ. “Black Bone” MRI: a potential alternative to CT with three-dimensional reconstruction of the craniofacial skeleton in the diagnosis of craniosynostosis. *European radiology* 2014;24(10):2417-2426.
10. Eley KA, Watt-Smith SR, Golding SJ. Three-dimensional reconstruction of the craniofacial skeleton with gradient echo magnetic resonance imaging (“black bone”): what is currently possible? *Journal of Craniofacial Surgery* 2017;28(2):463-467.
11. Patel KB, Eldeniz C, Skolnick GB, Commean PK, Boroojeni PE, Jammalamadaka U, Merrill C, Smyth MD, Goyal MS, An H. Cranial vault imaging for pediatric head trauma using a radial VIBE MRI sequence. *Journal of Neurosurgery: Pediatrics* 2022;1(aop):1-6.

12. Patel KB, Eldeniz C, Skolnick GB, Jammalamadaka U, Commean PK, Goyal MS, Smyth MD, An H. 3D pediatric cranial bone imaging using high-resolution MRI for visualizing cranial sutures: a pilot study. *Journal of Neurosurgery: Pediatrics* 2020;26(3):311-317.
13. Donoho DL. Compressed sensing. *IEEE Transactions on information theory* 2006;52(4):1289-1306.
14. Lustig M, Donoho D, Pauly JM. Sparse MRI: The application of compressed sensing for rapid MR imaging. *Magnetic Resonance in Medicine: An Official Journal of the International Society for Magnetic Resonance in Medicine* 2007;58(6):1182-1195.
15. Haldar JP, Hernando D, Liang Z-P. Compressed-sensing MRI with random encoding. *IEEE transactions on Medical Imaging* 2010;30(4):893-903.
16. Trzasko J, Manduca A. Highly Undersampled Magnetic Resonance Image Reconstruction via Homotopic  $\ell_0$ -Minimization. *IEEE Transactions on Medical imaging* 2008;28(1):106-121.
17. Knoll F, Bredies K, Pock T, Stollberger R. Second order total generalized variation (TGV) for MRI. *Magnetic resonance in medicine* 2011;65(2):480-491.
18. Akçakaya M, Nam S, Hu P, Moghari MH, Ngo LH, Tarokh V, Manning WJ, Nezafat R. Compressed sensing with wavelet domain dependencies for coronary MRI: a retrospective study. *IEEE Transactions on Medical Imaging* 2010;30(5):1090-1099.
19. Akçakaya M, Basha TA, Goddu B, Goepfert LA, Kissinger KV, Tarokh V, Manning WJ, Nezafat R. Low-dimensional-structure self-learning and thresholding: regularization beyond compressed sensing for MRI reconstruction. *Magnetic Resonance in Medicine* 2011;66(3):756-767.
20. Liang D, Liu B, Wang J, Ying L. Accelerating SENSE using compressed sensing. *Magnetic Resonance in Medicine: An Official Journal of the International Society for Magnetic Resonance in Medicine* 2009;62(6):1574-1584.
21. Otazo R, Kim D, Axel L, Sodickson DK. Combination of compressed sensing and parallel imaging for highly accelerated first-pass cardiac perfusion MRI. *Magnetic resonance in medicine* 2010;64(3):767-776.
22. Robson PM, Grant AK, Madhuranthakam AJ, Lattanzi R, Sodickson DK, McKenzie CA. Comprehensive quantification of signal-to-noise ratio and g-factor for image-based and k-space-based parallel imaging reconstructions. *Magnetic Resonance in Medicine: An Official Journal of the International Society for Magnetic Resonance in Medicine* 2008;60(4):895-907.
23. Chang Y, Liang D, Ying L. Nonlinear GRAPPA: A kernel approach to parallel MRI reconstruction. *Magnetic Resonance in Medicine* 2012;68(3):730-740.

24. Madore B. UNFOLD-SENSE: a parallel MRI method with self-calibration and artifact suppression. *Magnetic Resonance in Medicine: An Official Journal of the International Society for Magnetic Resonance in Medicine* 2004;52(2):310-320.
25. Sung K, Hargreaves BA. High-frequency subband compressed sensing MRI using quadruplet sampling. *Magnetic resonance in medicine* 2013;70(5):1306-1318.
26. Yang Y, Sun J, Li H, Xu Z. ADMM-CSNet: A deep learning approach for image compressive sensing. *IEEE transactions on pattern analysis and machine intelligence* 2018;42(3):521-538.
27. Shahdloo M, Ilıcak E, Tofighi M, Saritas EU, Çetin AE, Çukur T. Projection onto epigraph sets for rapid self-tuning compressed sensing MRI. *IEEE transactions on medical imaging* 2018;38(7):1677-1689.
28. Ramani S, Liu Z, Rosen J, Nielsen J-F, Fessler JA. Regularization parameter selection for nonlinear iterative image restoration and MRI reconstruction using GCV and SURE-based methods. *IEEE Transactions on Image Processing* 2012;21(8):3659-3672.
29. Wang S, Su Z, Ying L, Peng X, Zhu S, Liang F, Feng D, Liang D. Accelerating magnetic resonance imaging via deep learning. 2016. IEEE. p 514-517.
30. Lee D, Yoo J, Tak S, Ye JC. Deep Residual Learning for Accelerated MRI Using Magnitude and Phase Networks. *IEEE Transactions on Biomedical Engineering* 2018;65(9):1985-1995.
31. Lehtinen J, Munkberg J, Hasselgren J, Laine S, Karras T, Aittala M, Aila T. Noise2Noise: Learning image restoration without clean data. *arXiv preprint arXiv:180304189* 2018.
32. Liu J, Sun Y, Eldeniz C, Gan W, An H, Kamilov US. Rare: Image reconstruction using deep priors learned without groundtruth. *IEEE Journal of Selected Topics in Signal Processing* 2020;14(6):1088-1099.
33. McCann MT, Jin KH, Unser M. Convolutional neural networks for inverse problems in imaging: A review. *IEEE Signal Processing Magazine* 2017;34(6):85-95.
34. Lucas A, Iliadis M, Molina R, Katsaggelos AK. Using deep neural networks for inverse problems in imaging: beyond analytical methods. *IEEE Signal Processing Magazine* 2018;35(1):20-36.
35. Knoll F, Hammernik K, Zhang C, Moeller S, Pock T, Sodickson DK, Akcakaya M. Deep-learning methods for parallel magnetic resonance imaging reconstruction: A survey of the current approaches, trends, and issues. *IEEE signal processing magazine* 2020;37(1):128-140.
36. Liang D, Cheng J, Ke Z, Ying L. Deep magnetic resonance image reconstruction: Inverse problems meet neural networks. *IEEE Signal Processing Magazine* 2020;37(1):141-151.

37. Akçakaya M, Moeller S, Weingärtner S, Uğurbil K. Scan-specific robust artificial-neural-networks for k-space interpolation (RAKI) reconstruction: Database-free deep learning for fast imaging. *Magnetic resonance in medicine* 2019;81(1):439-453.
38. Zhu B, Liu JZ, Cauley SF, Rosen BR, Rosen MS. Image reconstruction by domain-transform manifold learning. *Nature* 2018;555(7697):487-492.
39. Mardani M, Gong E, Cheng JY, Vasanawala SS, Zaharchuk G, Xing L, Pauly JM. Deep generative adversarial neural networks for compressive sensing MRI. *IEEE transactions on medical imaging* 2018;38(1):167-179.
40. Han Y, Sunwoo L, Ye JC. e deep learning for accelerated MRI. *IEEE transactions on medical imaging* 2019;39(2):377-386.
41. Liu J, Sun Y, Xu X, Kamilov US. Image restoration using total variation regularized deep image prior. 2019. *Ieee*. p 7715-7719.
42. Romano Y, Elad M, Milanfar P. The little engine that could: Regularization by denoising (RED). *SIAM Journal on Imaging Sciences* 2017;10(4):1804-1844.
43. Mataev G, Milanfar P, Elad M. Deepred: Deep image prior powered by red. 2019. p 0-0.
44. Reehorst ET, Schniter P. Regularization by denoising: Clarifications and new interpretations. *IEEE transactions on computational imaging* 2018;5(1):52-67.
45. Yoo J, Jin KH, Gupta H, Yerly J, Stuber M, Unser M. Time-dependent deep image prior for dynamic MRI. *IEEE Transactions on Medical Imaging* 2021;40(12):3337-3348.
46. Hammernik K, Klatzer T, Kobler E, Recht MP, Sodickson DK, Pock T, Knoll F. Learning a variational network for reconstruction of accelerated MRI data. *Magnetic resonance in medicine* 2018;79(6):3055-3071.
47. Aggarwal HK, Mani MP, Jacob M. MoDL: Model-based deep learning architecture for inverse problems. *IEEE transactions on medical imaging* 2018;38(2):394-405.
48. Zhang J, Ghanem B. ISTA-Net: Interpretable optimization-inspired deep network for image compressive sensing. 2018. p 1828-1837.
49. Schlemper J, Caballero J, Hajnal JV, Price A, Rueckert D. A deep cascade of convolutional neural networks for MR image reconstruction. 2017. *Springer*. p 647-658.
50. Qin C, Schlemper J, Caballero J, Price AN, Hajnal JV, Rueckert D. Convolutional recurrent neural networks for dynamic MR image reconstruction. *IEEE transactions on medical imaging* 2018;38(1):280-290.

51. Mardani M, Sun Q, Donoho D, Pappayan V, Monajemi H, Vasanawala S, Pauly J. Neural proximal gradient descent for compressive imaging. *Advances in Neural Information Processing Systems* 2018;31.
52. Gregor K, LeCun Y. Learning fast approximations of sparse coding. 2010. p 399-406.
53. Hosseini SAH, Yaman B, Moeller S, Hong M, Akçakaya M. Dense recurrent neural networks for inverse problems: History-cognizant unrolling of optimization algorithms. 2019.
54. Lindberg DM, Stence NV, Grubenhoff JA, Lewis T, Mirsky DM, Miller AL, O'Neill BR, Grice K, Mourani PM, Runyan DK. Feasibility and accuracy of fast MRI versus CT for traumatic brain injury in young children. *Pediatrics* 2019;144(4).
55. French LR, Jackson IT, Melton III LJ. A population-based study of craniosynostosis. *Journal of clinical epidemiology* 1990;43(1):69-73.
56. Liu J, Sun Y, Gan W, Xu X, Wohlberg B, Kamilov US. Sgd-net: Efficient model-based deep learning with theoretical guarantees. *IEEE Transactions on Computational Imaging* 2021;7:598-610.
58. Gan W, Sun Y, Eldeniz C, Liu J, An H, Kamilov US. Deformation-Compensated Learning for Image Reconstruction without Ground Truth. *IEEE Transactions on Medical Imaging* 2022.
59. Yaman B, Hosseini SAH, Moeller S, Ellermann J, Uğurbil K, Akçakaya M. Self-supervised learning of physics-guided reconstruction neural networks without fully sampled reference data. *Magnetic resonance in medicine* 2020;84(6):3172-3191.

# **Chapter 4: Demonstrate that 3D High-Resolution Cranial MR Images Provide CT-Equivalent Bone Information to Clinically Identify Cranial Abnormalities, Patent Sutures, and Fractures**

## **4.1 Introduction**

CT scans are commonly utilized to provide high-quality three-dimensional images of the craniofacial skeleton for diagnosis and surgery planning. These scans expose patients to ionizing radiation and are linked to an increased risk of cancer (1-8). Head trauma is the most common indication for a CT scan (9-11). CT is also performed for evaluation of cranial dysmorphology and patency of cranial sutures (12-16). Although magnetic resonance imaging (MRI) is radiation-free, it has historically been unable to produce diagnostic-quality images of bone on a clinically relevant timeline.

3D imaging of cranial structures is used by multiple specialties including Neurosurgery, Craniofacial Surgery, and Neuroradiology for diagnosis, surgical planning, and postoperative evaluation in patients with head trauma and craniosynostosis. The objective of this study was to assess the clinical utility of using the novel MR techniques outlined in this work to create CT-equivalent 3D MR cranial bone images without sedation and assess the feasibility of the GA-VIBE sequence to obtain clinically acceptable cranial bone images for evaluation of patients presenting with head trauma and craniosynostosis in comparison to the gold-standard CT scan.



To attain this objective, we tested the working hypothesis that clinicians can identify cranial abnormalities, patent sutures, and fractures and so eliminate the need for CT imaging in >85% of pediatric patients presenting for head trauma or craniosynostosis. We tested the working hypothesis by having two expert clinicians independently evaluate the 3D high-resolution MR and CT cranial images. We used their evaluations to verify the clinical utility of the 3D MR images and develop criteria to identify patients for whom CT imaging is unnecessary.

We hypothesized that deploying automated motion correction protocols and using machine learning to generate pseudo-CT images from MRI scans produce images of pediatric patients' skulls that are acceptable for clinical use.

In pediatric MRI, head motion is a significant cause of image deterioration. To reduce movement during clinical MR scans, sedation is frequently employed (17,18). In MR head imaging, the sedation rate is reported to be between 60 and 65 percent for patients aged 1-6 and 32 percent for all patients under the age of 18. By reducing scan times and utilizing a multidisciplinary team to time imaging with the patient's biorhythms, efforts have been made to lessen the requirement for sedation (19-21). Sedation is still employed to produce clinically acceptable pictures despite these attempts. In order to give motion-artifact-free images without the use of anesthesia, it is very desirable to develop MR imaging technology. 3D rigid head motion is first detected, estimated, and then corrected in MR motion correction using a self-navigated MR approach. (22-29)

Another obstacle to the MR-based restoration of the cranial bone is the requirement to manually define the signal threshold in separating bone from other tissues. The creation of an operator-independent post-processing method utilizing a typical signal intensity approach is difficult and

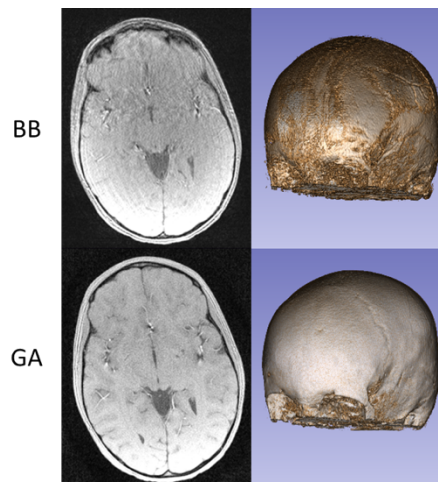
prevents its clinical application due to the weak signal contrast between bone and surrounding tissues in MR images. However, newly developed advanced image processing techniques, such as deep learning techniques, can automatically produce CT-like images from MR images (30).

In this study, Fast Low-Angle Shot (FLASH) Golden-Angle 3D stack-of-stars radial VIBE sequence (GA-VIBE) was used, which is more resistant to motion. In comparison to the gold-standard CT scan, the goal of this study is to determine whether the GA-VIBE sequence can produce clinically acceptable cranial bone imaging for the evaluation of patients with craniosynostosis/suture evaluation or head trauma. The 5 min motion-corrected pseudo-CT 3D reconstructed images in comparison to CT created clinically acceptable cranial images with the ability to detect suture closure and excellent ability to detect cranial fractures.

## 4.2 Materials and methods

### 4.2.1 Study Design and Participants

In this study, we used a Fast Low-Angle Shot (FLASH) Golden-Angle 3D stack-of-stars radial VIBE sequence (GA-VIBE), which is more motion-resistant than a Cartesian black bone acquisition. The GA-VIBE method is a radial scan that is inherently more resilient to motion



than the Black Bone and PETRA approaches. In a healthy pediatric participant, we compared the motion robustness of the GA-VIBE scan and the Black Bone scan. (Figure 4.1)

Figure 4.1. MR images (left) and the corresponding cranial bone images (right) using the BB (Black Bone) vs GA (Golden Angle radial) scans in a pediatric participant.

Before participant recruiting, IRB approval (#202112122) was obtained. Patients under the age of 18 were recruited who had a CT scan of the head as part of routine clinical treatment for head trauma evaluation of cranial suture patency

MRI scans were performed within 3 weeks of the CT scan for patients under 6 months of age and within 12 weeks for patients older than 6 months of age with a cranial vault fracture. MRI scans were performed within 6 months of the CT scan in situations where there was no fracture.

Exclusion criteria included time between CT and MRI is longer than the stated restrictions, having cranial operations between CT and MRI, or having a contraindication to MRI.

The study design was cross-sectional. The participant intervention was the radial MRI sequence that took approximately 5 minutes, either added to an already scheduled clinical MRI protocol or performed as a stand-alone research scan. Exclusion criteria consisted of (1) children who had a

cranial procedure after the CT and before the MRI, (2) time difference between MR and CT is out of the defined intervals, and (3) contraindications to MRI.

Thirty-three participants were enrolled between 2019 and 2021. Two were excluded due to excessive motion during the scan. Of the remaining 31 participants, 17 participants were male; 14 were female. Participant age at MRI ranged from 19 days to 17 years old (median = 10.9 years, interquartile range (IQR): 6.9 – 15.0). The time from CT to MRI ranged from 1 to 168 days (median = 22 days, IQR: 17 – 53). Only 2 of the 31 participants were sedated during their MRI. Demographic and diagnostic details of the 31 participants are shown in Table 4.1. Three of these subjects were excluded from the deep learning implementation since they had thick CT slices. The subjects with a spatial resolution of 2 mm were excluded from deep learning training and testing.

Table 4.1. Patient demographics and imaging data for trauma patients

<b>Subject</b>	<b>Age at MRI (years)</b>	<b>Sex</b>	<b>CT to MRI (days)</b>	<b>Sedated MRI</b>	<b>MRI Scanner Strength</b>	<b>Cranial Fractures on CT</b>
1	1.6	F	1	Yes	1.5T	depressed frontal and non-displaced parietal/temporal fractures
2	0.1	M	1	No	3T	parietal fracture, non-displaced
3	6.5	M	8	No	3T	None
4	10.9	F	22	No	3T	frontal fracture, non-displaced
5	10.9	M	4	Yes	3T	None
6	3.6	F	18	No	3T	None
7	8.6	F	168	No	3T	None
8	16.8	F	102	No	3T	None
9	14.0	M	110	No	3T	None
10	6.8	F	153	No	3T	None
11	7.1	M	103	No	3T	None
12	16.4	F	144	No	3T	None
13	12.6	M	9	No	3T	None
14	4.2	M	62	No	3T	occipital fracture, non-displaced
15	5.0	F	17	No	3T	occipital fracture, non-displaced
16	14.6	F	70	No	3T	None
17	16.2	M	38	No	3T	None
18	15.4	M	22	No	3T	None
19	7.8	F	23	No	3T	None
20	5.6	F	24	No	3T	frontal fracture, non-displaced
21	9.9	M	26	No	3T	None
22	17.1	M	14	No	3T	None
23	14.6	M	21	No	3T	None
24	10.2	F	22	No	3T	None
25	8.6	M	30	No	3T	None
26	8.4	M	33	No	1.5T	parietal fracture, non-displaced
27	15.8	M	15	No	3T	None
28	13.7	M	44	No	3T	None
29	15.9	F	20	No	3T	None
30	16.1	M	18	No	3T	None
31	14.4	F	19	No	3T	occipital fracture, non-displaced

Table 4.2. Patient demographics and imaging data

Patient #	Sex	Age at MRI (years)	Days after CT	Sedated MRI	Diagnosis
1	M	4.8	190	Yes	Arachnoid cysts
2	M	0.8	5	Yes	Encephalocele
3	M	1.4	101	No	Hydrocephaly
4	M	0.1	9	No	Sagittal synostosis
5	M	1.6	12	No	Sagittal and bi-lambdoid synostosis
6	M	1.8	12	Yes	Sagittal synostosis
7	F	2.7	193	Yes	Metopic synostosis
8	F	9.2	47	Yes	Frontonasal dysplasia
9	M	1.5	56	No	Sagittal synostosis
10	M	7.6	14	No	Crouzon syndrome
11	F	8.9	0	No	Crouzon syndrome
12	M	5	27	Yes	Sagittal synostosis
13	F	1.1	75	Yes	Sagittal synostosis
14	M	0.5	18	No	Shunt evaluation
15	M	2.5	90	No	Shunt evaluation

For the non-trauma category, 15 participants were recruited. MR scans could not be obtained on two candidates, a 16-month-old and a 3-year-old, due to poor patient compliance for an unsedated MRI. The GA-VIBE sequence was used on 15 participants. Age at MRI in these nine participants ranged from 3 weeks to 9 years (median age of 1.6 years). Median time after CT was 47 days (range: 5 – 193). None of the patients were sedated for CT whereas seven of the fifteen MR scans were performed under sedation per routine clinical care. Eight of the subjects had

diagnoses of craniosynostosis. Demographic and diagnostic details of the 15 participants are shown in Table 4.2

#### **4.2.2 Image Acquisition**

CT scans were collected using conventional clinical pediatric imaging techniques (Siemens Somatom Definition Flash or Force CT). Slice thickness ranged from 0.6mm to 1mm, with in-plane resolution ranging from 0.31mm to 0.39mm. Other settings included a 0.5-second rotation period, collimation of 64 x 0.6, 220 mAs, a pitch of 1, and a  $512 \times 512$  matrix. Reconstructions of soft tissue and bone kernels were carried out.

To acquire high-resolution MR images, a spoiled gradient-echo Golden-Angle 3D stack-of-stars radial VIBE sequence (GA-VIBE) was used (Siemens 3T Prisma, 3T Vida, or 1.5T Aera). This GA-VIBE sequence is a hybrid radial sequence with in-plane radial k-space coverage and slice-direction Cartesian coverage. For both the 3T and 1.5T scans, the imaging parameters of the GA-VIBE were FOV = 192 or 220 mm<sup>2</sup> depending on the head size, 224 slices, transverse orientation, a slice partial Fourier factor of 5/8, a flip angle of 3 to 5 degrees, a 320 x 320 acquisition matrix, resulting in a voxel size of 0.6-0.7 x 0.6-0.7 x 0.8 mm<sup>3</sup> and a scan duration of 7.7/4.76ms (1.5T), bandwidth 410 or 411 Hz/pixel (3T) vs. 280 Hz/pixel (1.5T), and the number of radial lines = 400 (3T) vs. 250 (1.5T). Bone has a low signal intensity in the GA-VIBE images, making it seem black. The GA-VIBE protocol was created to improve the contrast between bone and surrounding soft tissues by employing proton density weighting (low flip angle) and an in-phase echo time to preserve fat signal. Prior to performing a multi-coil non-uniform fast Fourier transform image reconstruction, motion-corrupted radial k-space lines were manually censored.

### 4.2.3 Motion Correction

A stack-of-stars radial acquisition scheme was utilized. A motion curve was extracted via a novel detection scheme that is simplistic and robust to inter-participant variations. The stationary frames of the acquisition were identified based on the curve and were combined into a motion-corrected, high-resolution image by using a forward-modeled reconstruction scheme (31-47).

### 4.2.4 Deep Learning-Based pCT

3D Golden-Angle stack-of-stars MRIs were obtained from 43 pediatric participants. Two patch-based ResUNets were trained using paired MR and CT patches randomly selected from the whole head (NetWH) or in the vicinity of bone, fractures/sutures, or air (NetBA) to synthesize pCT (30). A third ResUNet was trained to generate a binary brain mask using only MRI. The pCT images from NetWH ( $pCT_{NetWH}$ ) in the brain area and NetBA ( $pCT_{NetBA}$ ) in the non-brain area were combined to generate  $pCT_{Com}$ . A bias field correction is used to correct for spatial signal variations in MR images using the N4iTK algorithm (48). Each patient's MR was registered to their own CT images to match the spatial orientation and image resolution at  $0.3 \times 0.3 \times 0.5 \text{ mm}^3$  using an FSL affine registration (49). A level-set method was used to generate a mask to include only the head (cranial) region of the subject (50). Block matching 3D (BM3D) filtering was applied to the CT images to perform edge preserved smoothing and enhance suture representations.

Two different 3D patched-based ResUNet models were developed and combined to generate the final pCT from MR images (Figure 1). Both of the ResUnet models were trained using 3D MR image  $64 \times 64 \times 64$  patches where the central voxel determines the patch placement in the 3D volume.



The first model used patches selected randomly from the whole head (Whole Head model). The Whole Head ResUNet model utilized over one million partially overlapping 3D patches to increase the number of model training samples. Fractured bone and suture are the objects of interest or regions of interest (ROI), but they only occupy a small fraction of the total imaging volume. These ROIs are rarely represented in ResUNet training if the training patches are randomly selected over the whole image volume. To address this issue, we enhanced the representation of fractured bone and suture regions by manually segmenting these ROIs from CT as one independent class to ensure their presence in the training sample patches. (Bone/Air Enriched Model).

Enrolled patients had a 5-minute research MRI with automatic motion correction and pseudo-CT image processing, with the previously obtained CT scan acting as the control. An attending craniofacial plastic surgeon and a senior plastic surgery resident reviewed the MRI and CT scans. Depending on the cause for the scan, 1) the presence of a skull fracture or 2) cranial suture patency were noted first on the research MRI and then on the clinical CT.

#### **4.2.5 Clinical Evaluations**

Clinicians were given the participant's medical history and the purpose of imaging. Clinicians used RadiAnt DICOM viewer software Version 2020.2 (Medixant, Pozna, Poland) to view the slice-by-slice volumetric images and 3D surface renderings. Clinicians were able to change brightness and contrast, apply a sharpening filter if necessary, and switch orientation using multiplanar reconstruction after importing the DICOMs.

Clinicians assessed each participant's MR scans together, blind to the CT and diagnosis, and achieved an agreement on the position and kind of any cranial fractures.

The AO CMF guidelines were used to classify the fractures. Motion or noise artifacts in the pCT/CT images that obscure the areas of interest resulted in the need for additional imaging and therefore have unacceptable image quality. The presence or absence of the following structures was recorded. For craniosynostosis: the 6 primary cranial sutures: are sagittal, metopic, right and left lambdoid, and right and left coronal. For head trauma: cranial vault fractures: The AO cranial vault classification system was used to classify location (frontal bone, parietal bone, sphenoid bone, temporal bone, occipital bone), fracture line (single or multiple), and displacement (non-displaced, displaced but not depressed or depressed) (52).

In addition, using a 5-point Likert scale, the clinicians were asked to rate the image quality for clinical diagnosis and whether an additional scan was required. "The image quality allows for clinical diagnosis of bone fractures," for example. 1) Agree, 2) Strongly agree, 3) Neither agree nor disagree, 4) Disagree, 5) Strongly disagree. Following the MRI assessment, the clinicians immediately went over the same participant's CT scan, grading image quality, the necessity for additional imaging, and the detection and classification of any cranial fractures. Clinicians were asked to rate the appropriateness of MR images for clinical diagnosis on a 4-point scale after reviewing both CT and MR images for a participant (inadequate, sufficient, good, and excellent). Excel 2013 was used to collect responses and generate descriptive statistics (Microsoft, Redmond, WA). Fisher's exact test was used to compare image quality responses across modalities in R. (Version 4.0.3, R Core Team, 2020). Statistical significance was established to be  $p < 0.05$ .

## 4.3 Results

A total of 15 patients underwent imaging to evaluate suture patency, and 28 patients underwent CT and MRI for evaluation of head trauma. Acceptability for clinical use was graded as “Excellent” for 81% of the MRIs, “Good” for 14%, and “Sufficient” for 5%.

For head cranial suture patency, there was concordance between MRI and CT in 15 (100%) patients. All scans were acceptable for clinical use. Figure 4.2 depicts sample 3D rendered images for suture evaluation. Figure 4.2 demonstrates CT and pCT images created from MRI of four patients, Patient one was 5 years old and diagnosed with arachnoid cysts and lambdoid sutures on the back of the head, patient two was 19 months old with sagittal synostosis, patient three was 9 months with Dandy-walker syndrome, and patient four is 18 months, post-repair of sagittal synostosis. The proposed deep learning ResUNet models generated pCT images that closely resemble the gold-standard CT images.

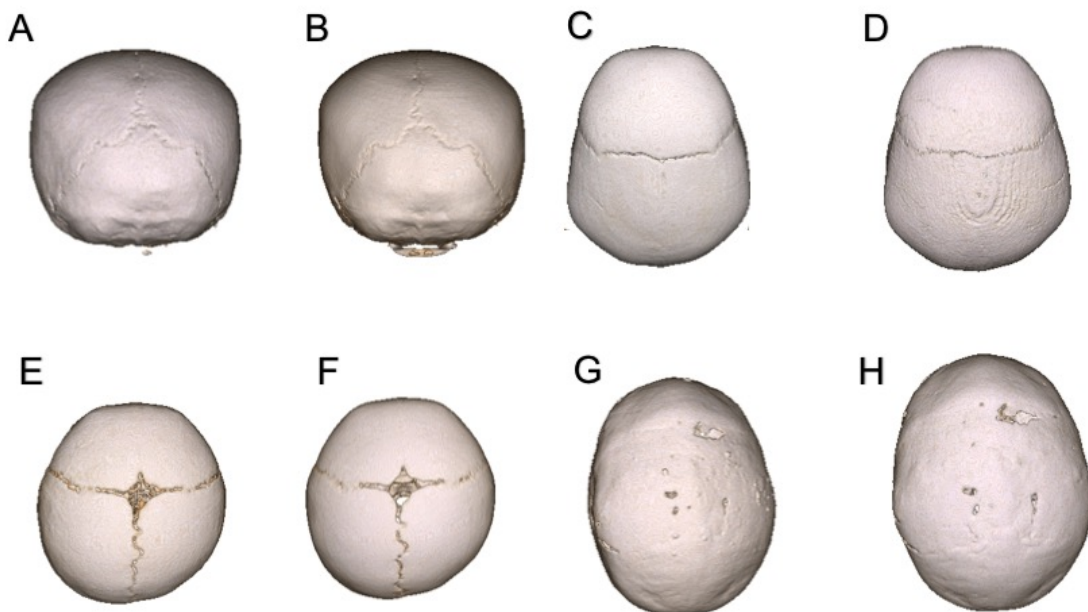


Figure 4.2. (pCT (A,C,E,G) and CT (B,D,F,H) 3D-reconstruction of images created from MRI of four patients, Patient one was 5 years old and diagnosed with arachnoid cysts and lambdoid sutures marked in red arrows (A,B), patient two was 19 months old with sagittal synostosis (C,D), patient three was 9 months with Dandy-walker syndrome (E,F), and patient four was 18 months, post-repair of sagittal synostosis (G,H).

For head trauma, there was concordance between MRI and CT in 27 (96%). For the discordant patient with head trauma, there were about 8 weeks between the CT performed at the time of injury and the research MRI scan, which showed radiographic healing. 6 out of 28 patients had one or more skull fractures, according to CT imaging. MRI identified 6 fractures in 5 patients. The strength of agreement differed slightly but not significantly between CT and MRI: clinicians strongly agreed that imaging was acceptable on 28 CT's and 25 MRI's ( $p = 0.705$ ) (Table 3).

Figures 4.3 and 4.4 demonstrate sample volumetric slices and 3D representations of CT and pCT images created from MRI of two people who sustained fractures. Overall, the sensitivity and specificity of fracture identification by MRI were 100% when compared to gold-standard CT. Furthermore, there were no differences in the classification of fracture type or location between CT and MRI.

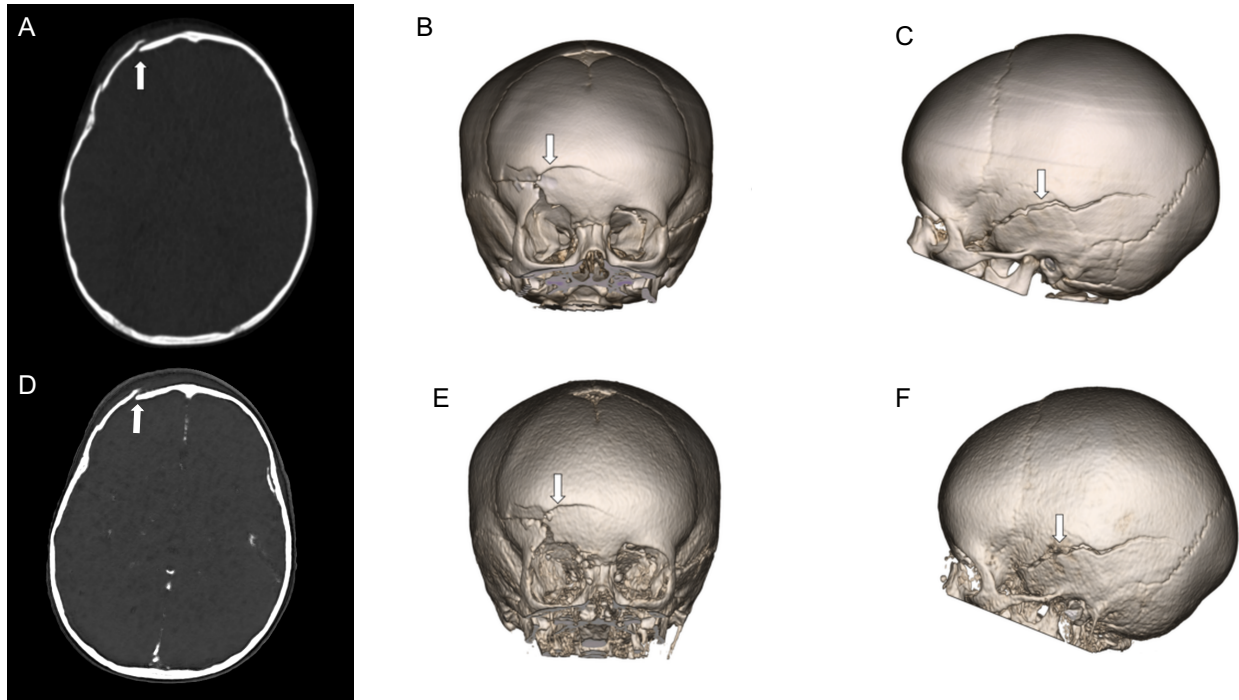


Figure 4.3. 1.6 years old, multiple bone fractures. Arrows indicate fracture. CT axial volumetric sample (A). CT 3D-reconstruction (B, C). pCT axial volumetric sample (D) and pCT 3D-reconstruction (E, F).

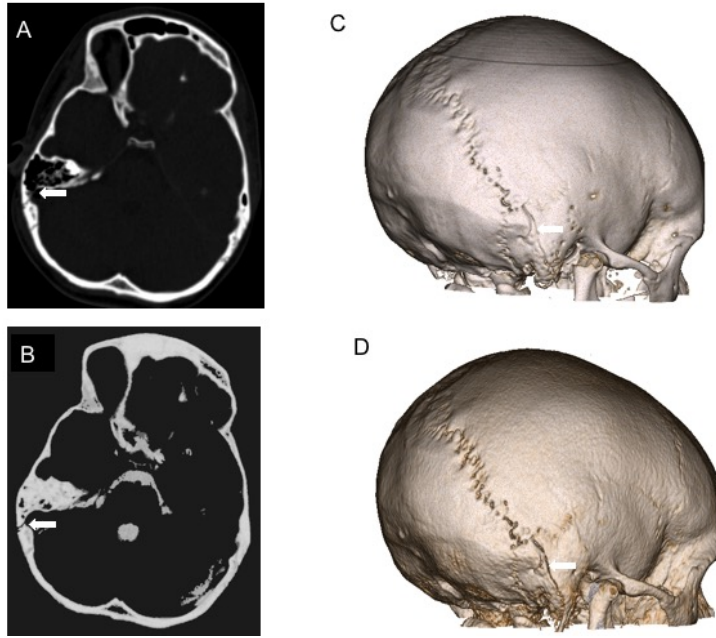


Figure 4.4. 14 years old, occipital bone fracture. Arrows indicate a fracture. CT axial volumetric sample (A). CT 3D-reconstruction (C). pCT axial volumetric sample (B) and pCT 3D-reconstruction (D).

## 4.4 Discussion and Summary

Automated machine learning-generated MRI images of the pediatric skull were acceptable for clinical use and offer a high level of diagnostic accuracy when compared to standard CT scans. Motion-corrected, machine learning-processed MRI images are acceptable for clinical use and have high diagnostic accuracy without exposure to ionizing radiation.

Magnetic Resonance Imaging (MRI) can be considered a safe alternative to CT because MRI does not expose patients to ionizing radiation. However, MRI imaging is clinically limited for

visualizing bone structures but provides greater soft tissue details. Eley et al. proposed a “Black Bone” (BB) protocol by using an MR 3D gradient echo sequence. Inverting the MRI image intensities caused the dark bone signal intensities to become bright and the bright soft tissue intensities to become dark to allow the bone to be more easily visualized (53-56). However, Black Bone MR imaging methods are not common because of suboptimal osseous/soft tissue contrast, motion artifacts in non-sedated patients, and manual post-processing steps by an operator which limits the capability MRI to produce CT quality 3D reconstructed images

Without sedation, both the PETRA sequence and gradient-echo "black bone" demonstrated low accuracy in the detection of non-displaced fractures. Due to its non-Cartesian acquisition pattern, the proposed GA-VIBE approach is fundamentally less sensitive to motion and maximizes picture contrast between bone and the surrounding soft tissue. On children under the age of six who presented with traumatic brain injury, Lindberg and colleagues used a GRE sequence and T2 images (9). Impressively, they were able to complete unsedated MRI scans on 99% of their subjects, and they discovered five persons who had severe brain injuries that CT imaging had missed. Six of the eight non-depressed skull fractures were overlooked by MRI, though. In our case series, cranial vault fractures and sutures on participants who weren't sedated could all be appropriately identified by clinicians utilizing MRI (60,61).

Although the sensitivity and specificity of MR imaging to fractures were 100% in our small sample, the reviewers felt one of the MRI images was unacceptable for clinical diagnosis due to severe motion artifacts.

The GA-VIBE sequence is a promising MRI method to achieve CT-like 3D cranial bone images in pediatric subjects. It is also inherently more resistant to motion than the Black Bone sequence.

We demonstrated that 3D-reconstructed high-resolution MR images can serve as a viable alternative to CT cranial images in a large patient cohort, enhanced MR image quality through motion correction, and automatically created CT-like images using MR images. By reducing radiation and possibly sedation-related patient hazards, the suggested technique will have a significant influence on pediatric health.



## **References**

1. Stewart NM, Hallac RR, Chou PY, et al. Craniofacial Flash: Minimizing Radiation Dose in Pediatric Craniofacial Computed Tomography. J Craniofac Surg 2018;29:1751-4.
2. Radiation Risks and Pediatric Computed Tomography (CT): A Guide for Health Care Providers. 2018. at <https://www.cancer.gov/about-cancer/causes-prevention/risk/radiation/pediatric-ct-scans>.)
3. Miglioretti DL, Johnson E, Williams A, et al. The use of computed tomography in pediatrics and the associated radiation exposure and estimated cancer risk. JAMA Pediatr 2013;167:700-7.
4. Brenner DJ, Elliston CD, Hall EJ, Berdon WE. Estimates of the cancer risks from pediatric CT radiation are not merely theoretical: comment on "point/counterpoint: in x-ray computed tomography.
5. Parker L. Computed tomography scanning in children: radiation risks. Pediatr Hematol Oncol 2001;18:307-8.
6. Pearce MS, Salotti JA, Little MP, et al. Radiation exposure from CT scans in childhood and subsequent risk of leukaemia and brain tumours: a retrospective cohort study. Lancet 2012;380:499-505.
7. Smyth MD, Narayan P, Tubbs RS, et al. Cumulative diagnostic radiation exposure in children with ventriculoperitoneal shunts: a review. Childs Nerv Syst 2008;24:493-7.
8. Brenner DJ, Hall EJ. Computed tomography--an increasing source of radiation exposure. N Engl J Med 2007;357:2277-84.
9. Lindberg DM, Stence NV, Grubenhoff JA, et al. Feasibility and Accuracy of Fast MRI Versus CT for Traumatic Brain Injury in Young Children. Pediatrics 2019;144.
10. Nelson EL, Melton LJ, 3rd, Annegers JF, Laws ER, Offord KP. Incidence of skull fractures in Olmsted County, Minnesota. Neurosurgery 1984;15:318-24.
11. Stanley RM, Hoyle JD, Jr., Dayan PS, et al. Emergency department practice variation in computed tomography use for children with minor blunt head trauma. J Pediatr 2014;165:1201-6 e2.
12. Doumit GD, Papay FA, Moores N, Zins JE. Management of sagittal synostosis: a solution to equipoise. J Craniofac Surg 2014;25:1260-5.

13. Kestle JRW, Lee A, Anderson RCE, et al. Variation in the management of isolated craniosynostosis: a survey of the Synostosis Research Group. *J Neurosurg Pediatr* 2018;22:627-31.
14. Domeshek LF, Mukundan S, Jr., Yoshizumi T, Marcus JR. Increasing concern regarding computed tomography irradiation in craniofacial surgery. *Plast Reconstr Surg* 2009;123:1313-20.
15. Fearon JA, Singh DJ, Beals SP, Yu JC. The diagnosis and treatment of single-sutural synostoses: are computed tomographic scans necessary? *Plast Reconstr Surg* 2007;120:1327-31.
16. Binning M, Ragel B, Brockmeyer DL, Walker ML, Kestle JR. Evaluation of the necessity of postoperative imaging after craniosynostosis surgery. *J Neurosurg* 2007;107:43-5. technique factors should be selected appropriate to patient size. against the proposition". *Med Phys* 2001;28:2387-8.
17. Cote CJ, Karl HW, Notterman DA, Weinberg JA, McCloskey C. Adverse sedation events in pediatrics: analysis of medications used for sedation. *Pediatrics* 2000;106:633-44.
18. Kannikeswaran N, Mahajan PV, Sethuraman U, Groebe A, Chen X. Sedation medication received and adverse events related to sedation for brain MRI in children with and without developmental disabilities. *Paediatr Anaesth* 2009;19:250-6.
19. Malviya S, Voepel-Lewis T, Eldevik OP, Rockwell DT, Wong JH, Tait AR. Sedation and general anaesthesia in children undergoing MRI and CT: adverse events and outcomes. *Br J Anaesth* 2000;84:743-8.
20. Kralik SF, Supakul N, Wu IC, et al. Black bone MRI with 3D reconstruction for the detection of skull fractures in children with suspected abusive head trauma. *Neuroradiology* 2019;61:81-7.
21. Goldwasser T, Bressan S, Oakley E, Arpone M, Babl FE. Use of sedation in children receiving computed tomography after head injuries. *Eur J Emerg Med* 2015;22:413-8.
22. Uman JC, Tumin D, Raman V, Thung A, Adler B, Tobias JD. MRI Utilization and the Associated Use of Sedation and Anesthesia in a Pediatric ACO. *J. Am. Coll. Radiol. JACR* 2017;14:924–930.
23. Uffman JC, Tumin D, Raman V, Thung A, Adler B, Tobias JD. MRI Utilization and the Associated Use of Sedation and Anesthesia in a Pediatric ACO. *J Am Coll Radiol* 2017;14:924-30.
34. Dong SZ, Zhu M, Bulas D. Techniques for minimizing sedation in pediatric MRI. *J Magn Reson Imaging* 2019.
25. Zaitsev M, Dold C, Sakas G, Hennig J, Speck O. Magnetic resonance imaging of freely moving objects: prospective real-time motion correction using an external optical motion tracking system. *NeuroImage* 2006;31:1038–1050 doi: 10.1016/j.neuroimage.2006.01.039.

26. van der Kouwe AJW, Benner T, Dale AM. Real-time rigid body motion correction and shimming using cloverleaf navigators. *Magn. Reson. Med.* 2006;56:1019–1032.
27. White N, Roddey C, Shankaranarayanan A, et al. PROMO – Real-time Prospective Motion Correction in MRI using Image-based Tracking. *Magn. Reson. Med. O . J. Soc. Magn. Reson. Med. Soc. Magn. Reson. Med.* 2010;63:91–105 doi: 10.1002/mrm.22176.
28. Lin W, Guo J, Rosen MA, Song HK. Respiratory motion-compensated radial dynamic contrast-enhanced (DCE)-MRI of chest and abdominal lesions. *Magn Reson Med* 2008;60:1135-46.
29. Grimm R, Furst S, Souvatzoglou M, et al. Self-gated MRI motion modeling for respiratory motion compensation in integrated PET/MRI. *Med Image Anal* 2015;19:110-20.
30. Eshraghi Boroojeni P, Chen Y, Commean PK, et al. Deep-learning synthesized pseudo-CT for MR high-resolution pediatric cranial bone imaging (MR-HiPCB). *Magn Reson Med.* 2022;1-13. doi: 10.1002/mrm.29356
31. Pipe JG. Motion correction with PROPELLER MRI: Application to head motion and free-breathing cardiac imaging. *Magn. Reson. Med.* 1999;42:963–969.
32. Liu C, Bammer R, Kim D, Moseley ME. Self-navigated interleaved spiral (SNAILS): Application to high-resolution diffusion tensor imaging. *Magn. Reson. Med.* 2004;52:1388–1396 doi: 10.1002/mrm.20288.
33. Ehman RL, Felmlee JP. Adaptive technique for high-definition MR imaging of moving structures. *Radiology* 1989;173:255–263 doi:10.1148/radiology.173.1.2781017.
34. Johnson PM, Liu J, Wade T, Tavallaei MA, Drangova M. Retrospective 3D motion correction using spherical navigator echoes. *Magn. Reson. Imaging* 2016;34:1274–1282 doi: 10.1016/j.mri.2016.06.006.
35. Kecskemeti S, Samsonov A, Velikina J, et al. Robust Motion Correction Strategy for Structural MRI in Unsedated Children Demonstrated with Three-dimensional Radial MPnRAGE. *Radiology* 2018;289:509–516 doi: 10.1148/radiol.2018180180.
36. Welch EB, Rossman PJ, Felmlee JP, Manduca A. Self-navigated motion correction using moments of spatial projections in radial MRI. *Magn. Reson. Med.* 2004;52:337–345 doi: 10.1002/mrm.20151.
37. Anderson III AG, Velikina J, Block W, Wieben O, Samsonov A. Adaptive retrospective correction of motion artifacts in cranial MRI with multicoil three-dimensional radial acquisitions. *Magn. Reson. Med.* 2013;69:1094–1103 doi: 10.1002/mrm.24348.
38. Feng L, Axel L, Chandarana H, Block KT, Sodickson DK, Otazo R. XD-GRASP: Golden-angle radial MRI with reconstruction of extra motion-state dimensions using compressed sensing. *Magn. Reson. Med.* 2016;75:775–788.

39. Glover GH, Pauly JM. Projection Reconstruction Techniques for Reduction of Motion Effects in MRI. *Magn. Reson. Med.* 1992;28:275–289.
40. Loktyushin A, Nickisch H, Pohmann R, Schölkopf B. Blind retrospective motion correction of MR images. *Magn. Reson. Med.* 2013;70:1608–1618.
41. Cordero-Grande L, Teixeira RPAG, Hughes EJ, Hutter J, Price AN, Hajnal JV. Sensitivity Encoding for Aligned Multishot Magnetic Resonance Reconstruction. *IEEE Trans. Comput. Imaging* 2016;2:266–280.
42. Graedel NN, McNab JA, Chiew M, Miller KL. Motion correction for functional MRI with three-dimensional hybrid radial-Cartesian EPI. *Magn. Reson. Med.* 2017;78:527–540.
43. Cruz G, Atkinson D, Buerger C, Schaefer T, Prieto C. Accelerated motion corrected three-dimensional abdominal MRI using total variation regularized SENSE reconstruction. *Magn. Reson. Med.* 2016;75:1484–1498.
44. Cruz G, Atkinson D, Henningsson M, Botnar RM, Prieto C. Highly efficient nonrigid motion-corrected 3D whole-heart coronary vessel wall imaging. *Magn. Reson. Med.* 2017;77:1894–1908.
45. Eldeniz, Cihat, Jammalamadaka, Udayabhanu, Skolnick, Gary B., Commean, Paul K., Patel, Kamlesh B., An, Hongyu. Skull MRI with MUFFIN: MultiFrame Forward-modeled Image Numismatics. In Proceedings of the 29th Annual Meeting of ISMRM, Virtual, 2021. Abstract #522.
46. Eldeniz C, Fraum T, Salter A, Chen Y, Gach HM, Parikh PJ, Fowler KJ, An H. CAPTURE: Consistently Acquired Projections for Tuned and Robust Estimation: A Self-Navigated Respiratory Motion Correction Approach. *Invest Radiol.* 2018;53(5):293-305. doi: 10.1097/RLI.0000000000000442. PubMed PMID: 29315083; PMCID: PMC582511.
47. Peters DC, Korosec FR, Grist TM, et al. Undersampled projection reconstruction applied to MR angiography. *Magn. Reson. Med.* 2000;43:91–101.
48. Tustison NJ, Avants BB, Cook PA, et al. N4ITK: improved N3 bias correction. *IEEE Trans Med Imaging* 2010;29:1310-20.
49. Jenkinson M, Bannister P, Brady M, Smith S. Improved optimization for the robust and accurate linear registration and motion correction of brain images. *Neuroimage* 2002;17:825-41.
50. Vese LA, Chan TF. A multiphase level set framework for image segmentation using the Mumford and Shah model. *international journal of computer vision* 2002;50:271-93.
51. Fedorov A, Beichel R, Kalpathy-Cramer J, et al. 3D Slicer as an image computing platform for the Quantitative Imaging Network. *Magn Reson Imaging* 2012;30:1323-41.
52. Cornelius CP, Kunz C, Neff A, Kellman RM, Prein J, Audige L. The Comprehensive AOCMF Classification System: Fracture Case Collection, Diagnostic Imaging Work Up,

AOCOIAC Iconography and Coding. Craniomaxillofac Trauma Reconstr. 2014;7(Suppl 1):S131-5. Epub 2014/12/10. doi: 10.1055/s-0034-1393722. PubMed PMID: 25489397; PMCID: PMC4251729.

53. Eley KA, McIntyre AG, Watt-Smith SR, Golding SJ. "Black bone" MRI: a partial flip angle technique for radiation reduction in craniofacial imaging. *Br J Radiol* 2012;85:272-8.

54. Eley KA, Watt-Smith SR, Golding SJ. "Black bone" MRI: a potential alternative to CT when imaging the head and neck: report of eight clinical cases and review of the Oxford experience. *Br J Radiol* 2012;85:1457-64.

55. Eley KA, Watt-Smith SR, Golding SJ. Three-Dimensional Reconstruction of the Craniofacial Skeleton With Gradient Echo Magnetic Resonance Imaging ("Black Bone"): What Is Currently Possible? *J Craniofac Surg* 2017;28:463-7.

56. Kralik SF, Supakul N, Wu IC, et al. Black bone MRI with 3D reconstruction for the detection of skull fractures in children with suspected abusive head trauma. *Neuroradiology* 2019;61:81-7.

57. Dremmen MHG, Wagner MW, Bosemani T, et al. Does the Addition of a "Black Bone" Sequence to a Fast Multisequence Trauma MR Protocol Allow MRI to Replace CT after Traumatic Brain Injury in Children? *AJNR Am J Neuroradiol* 2017;38:2187-92.

58. Lu A, Gorny KR, Ho ML. Zero TE MRI for Craniofacial Bone Imaging. *AJNR Am J Neuroradiol* 2019;40:1562-6.

59. Grodzki DM, Jakob PM, Heismann B. Ultrashort echo time imaging using pointwise encoding time reduction with radial acquisition (PETRA). *Magn Reson Med* 2012;67:510-8.

60. Patel KB, Eldeniz C, Skolnick GB, et al. 3D pediatric cranial bone imaging using high-resolution MRI for visualizing cranial sutures: a pilot study. *J Neurosurg Pediatr* 2020:1-7.

61. Patel KB, Eldeniz C, Skolnick GB, Commeyan PK, Eshraghi Boroojeni P, Jammalamadaka U, Merrill C, Smyth MD, Goyal MS, An H. Cranial vault imaging for pediatric head trauma using a radial VIBE MRI sequence. *J Neurosurg Pediatr*. 2022 Apr 22:1-6. doi: 10.3171/2022.2.PEDS2224. Epub ahead of print. PMID: 35453112.

# **Chapter 5: Summary and Future Work**

## **5.1 Summary**

Head trauma is common in the pediatric population resulting in emergency cases.

Craniosynostosis is the abnormal early fusion of a cranial suture, causing an irregular-shaped cranium. 3D high-resolution head CT scans are commonly used in these pediatric patients to identify skull fractures and sutures. However, CT exposes pediatric patients to ionizing radiation and increases the risk of cancer. MRI is a safe alternative to CT, as it does not expose patients to ionizing radiation. Current manual processing is time-consuming and unsuitable for clinical use. We developed a fully automated deep learning method to generate high-resolution pseudo-CT images from MRI. In this dissertation, we developed a robust and fully automated deep learning method to create pCT images from MR images, which facilitates translating MR cranial bone imaging into clinical practice for pediatric patients. The DL methods demonstrated that CT-equivalent 3D cranial bone images from pediatric subjects using a GA MR scan can be used to identify skull fractures and sutures.

A high-resolution MRI capable of resolving the detail of bony structures at sub-millimeter resolution is desired. A short MR acquisition results in under-sampled k-space data below the Nyquist rate, leading to artifacts and high noise. In this work, we developed a high-resolution reconstruction deep-learning method to reduce the MR acquisition time from 5 minutes to 1 minute. We achieved high-resolution MR ( $0.6 \times 0.6 \times 0.8 \text{ mm}^3$ ) with a one-minute acquisition time.

The 1-minute MR scans provide high-quality visualization of sutures/ fractures in craniosynostosis/trauma patients. The MR one-minute scan can be used to identify skull fractures

and sutures. The proposed deep learning one-minute scan closely resembled the 5-minute MRI scan in terms of image quality. Our results showed that our deep learning approach outperformed the conventional CS and SSDU approach. High-resolution 1-minute acquired MR images can provide CT-like images for clinical diagnostic evaluation for craniosynostosis and trauma patients.

We demonstrated that clinicians can identify cranial abnormalities, patent sutures, and fractures from MRI so CT imaging is unnecessary for >90% of pediatric patients presenting with head trauma or craniosynostosis

We developed a robust and fast 3D high-resolution MRI to provide cranial bone imaging in pediatric patients evaluated for head trauma or craniosynostosis. By reducing patient risks related to ionizing radiation, this project will have a significant influence on pediatric health. Future testing of the suggested method can be done in a multi-center trial. Though the techniques established in this research can be applied to assess bone in other regions of the body, this project is focused on minimizing the number of head CT scans in pediatric patients.

## **5.2 Future Work**

### **5.2.1 Increase the sample size of the study and train different models for different age ranges**

Deep learning networks can be improved by using more image data from a greater number of participants across a wide age range in the training. More patients are being enrolled into this ongoing study. With new patients' data added to the study, we can increase the number of

patches used to train the network, which will improve the training process and the network's parameter estimation.

In the future, as recruiting more patients study population will consist of 182 children (age 0 to 18) evaluated at SLCH for head trauma or craniosynostosis (n=121 and 61, respectively, based on clinical volume). In a pilot study, we enrolled 40 pediatric participants for an unsedated MR scan. We were able to obtain  $\geq 1$ -minute MR data from 88% of these pediatric participants, without physical constraints and with help from child life specialists. We expect a similar success rate in acquiring data in this study, so we will have usable data from  $n=160$  ( $182 \times 88\%$ ) participants. Historical data on the presentation for synostosis and head trauma at our institution suggests that approximately 40% of patients will be infants less than 6 months old, 36% will be 6 months to 5 years old, and the remainder (24%) between 5 and 18 years old.

The pediatric patients in this study have an age span of 0 to 18 years. Young pediatric patients, particularly infants (0-6 months) undergo rapid brain/head development. The cranium doubles in size in the first 6 months of life, triples by 2.5 years, and is 90% completed by age 5(1). The development of a diploic space and increase of calvarial thickness occurs at around 2-5 years of age (2). Tissue density, contrast, and size of the cortical bone and soft tissue may change rapidly during the first years of life. Cortical bone density and size and tissue MR properties will change rapidly during this age span. These age-dependent MR and CT imaging signal changes may impose a challenge in generalizing the trained ResUNet across all ages. In our study, we propose to perform a balanced sampling across all ages to account for this signal age dependence. If it does not fully account for this age effect, we will either derive longitudinal image contrast changes through image registration to the atlas and further normalize images with this contrast according to the age; or 2) train different neural networks for different ages. Training multiple



networks specifically for different age groups is possible but may suffer from a small sample size in each network training. In this study, we propose a general network first trained on the full cohort age range followed by transfer training based on the pre-trained general network for specific age ranges: 0-6 months, 6 months-5 years, and >5 years old (3).

### **5.2.2 Develop a 3D Bayesian ResUNet to estimate pseudo-CT (pCT) and uncertainty maps and determine the extent to which we can confidently identify cranial suture patency, and fractures via CT-equivalent bone 3D high-resolution cranial MR images**

The Bayesian deep learning framework can estimate both the aleatoric and epistemic uncertainties by replacing the deterministic network's weight parameters with a probability distribution (4). The aleatoric uncertainty is due to data-inherent uncertainty (reflecting the noise inside the data), and it can't be resolved by including more samples. Aleatoric uncertainty is estimated as another output of the Bayesian ResUNet besides pCT. The Bayesian ResUNet includes aleatoric uncertainty ( $\sigma$ ) in the loss function as either Gaussian or Laplacian prior. For Gaussian prior,  $(p(y|x) = \frac{1}{\sigma\sqrt{2\pi}} e^{-(f(x)-y)^2/2\sigma^2})$ , the loss function is  $-\log p(y_i|x_i) \propto \frac{1}{2\sigma^2} \|y_i - f(x_i)\|^2 + \frac{1}{2} \log(\sigma^2)$ , while for Laplacian prior, the loss function is  $-\log p(y_i|x_i) \propto \frac{\sqrt{2}}{\sigma} \|y_i - f(x_i)\| + \log(\sigma)$ . To obtain epistemic uncertainty, the Bayesian framework employs Monte Carlo dropout as a Bayesian inference approximation. Random dropouts are performed during both training and testing. During testing, Bayesian ResUNet generates numerous pCTs using random dropout for the same input. The epistemic uncertainty is then computed as the

variance of these pCTs (5,6). The total uncertainty is computed as the summation of the aleatoric and epistemic uncertainty.

Clinicians have high confidence in what they see with a confidence map included for their evaluation. Both high confidence and high accuracy are desired for clinical evaluation. The goal is to find out the confidence level and accuracy based on synostosis and/or fracture at different ages. If there are CT/MR image problems the clinician's confidence would be lower which would affect the accuracy.

### **5.2.3 Generate 1 min motion-corrected pCTs**

In this dissertation, we developed a fully automated method to create 5 min pCT images.

Furthermore, we reduced the MRI acquisition time from 5 minutes to 1 minute. We determined the clinical utility of the 5 min motion-corrected pCT images. A future study will create pCT images using 1-minute MRI data and evaluate their clinical utility by physicians. Based on clinicians' medical training using clinical CT for diagnosis, our clinical team of three reviewers will use each subject's pCT and uncertainty map to make a consensus evaluation to categorize pCT images as "acceptable" or "not acceptable" for clinical use. If the region of clinical interest, e.g. a cranial fracture or cranial suture, has high uncertainty, clinicians will thus become aware of potentially decreased diagnostic ability. The goal is to exclude as few scans as possible while retaining 100% diagnostic accuracy in the sub-group of patients who have "acceptable for clinical use" pCT images. We hypothesize that pCT images will be rated as "acceptable for clinical use" in  $\geq 90\%$  of completed MR scans. In our preliminary studies after implementation of a consensus evaluation, to mimic the clinical standard of care, clinicians achieved 100% diagnostic sensitivity and 100% specificity on all MR images found to be acceptable

#### **5.2.4 Introducing new evaluation matrices for more accurate evaluation**

Currently Dice Coefficient and MAE are two main accuracy measurements to compare the quality of final pCT with CT images. However, these two quantitative metrics do not directly evaluate cranial bone fractures and suture patency. Introducing accuracy metrics more focused on suture and fracture regions might be necessary for clinical evaluation. Fréchet Distance (FD) is a measure of similarity between two 3D curves by accounting for the location and order of points on the curve (10). 3DSlicer is used to manually trace fractures and sutures as 3D curves on CT, pCT, and manual MR segmentation images. FD will be computed between pCT and CT, and between manual MR segmentation and CT to evaluate whether the outlined fractures and sutures using pCT or manual MR segmentation match with those identified using the CT. A smaller FD indicates a better match. We expect that pCT provides higher DC and smaller FD than manual MR segmentation.

# **References**

1. Kamdar MR, Gomez RA, Ascherman JA. Intracranial volumes in a large series of healthy children. *Plast Reconstr Surg.* 2009;124(6):2072-5. Epub 2009/12/03. doi: 10.1097/PRS.0b013e3181bcefc4. PubMed PMID: 19952664.
2. Ghosh TD, Skolnick G, Nguyen DC, Sun H, Patel K, Smyth MD, Woo AS. Calvarial thickness and diploic space development in children with sagittal synostosis as assessed by computed tomography. *J Craniofac Surg.* 2014;25(3):1050-5. Epub 2014/05/14. doi: 10.1097/SCS.0000000000000762. PubMed PMID: 24820717.
3. Ladefoged CN, Hansen AE, Henriksen OM, Bruun FJ, Eikenes L, Oen SK, Karlberg A, Hojgaard L, Law I, Andersen FL. AI-driven attenuation correction for brain PET/MRI: Clinical evaluation of a dementia cohort and importance of the training group size. *Neuroimage.* 2020;222:117221. Epub 2020/08/05. doi: 10.1016/j.neuroimage.2020.117221. PubMed PMID: 32750498.
4. Kendall A, Gal Y. What Uncertainties Do We Need in Bayesian Deep Learning for Computer Vision CoRR. 2017;abs/1703.04977.
5. Gal Y, Ghahramani Z. Dropout as a Bayesian Approximation: Representing Model Uncertainty in Deep Learning. In: Maria Florina B, Kilian QW, editors. *Proceedings of The 33rd International Conference on Machine Learning; Proceedings of Machine Learning Research: PMLR*; 2016. p. 1050--9.
6. Gal Y, Ghahramani Z. Bayesian Convolutional Neural Networks with Bernoulli Approximate Variational Inference 2016 2016.
7. He K, Zhang X, Ren S, Sun J. Deep Residual Learning for Image Recognition. *IEEE Computer Vision and Pattern Recognition (CVPR)* 2016. p. 770-8.
8. Zhang H, Goodfellow I, Metaxas D, Odena A. Self-Attention Generative Adversarial Networks. *International Conference on Machine Learning* 2019. p. 770-8
9. Karim Armanian, Chenming Jian, Mark Fisher,.Medical Image Translation using GAN. *IEEE Computer Vision and Pattern Recognition (CVPR)*; 2019. p. 770-8.
10. ALT H, GODAU M. COMPUTING THE FRÉCHET DISTANCE BETWEEN TWO POLYGONAL CURVES. *International Journal of Computational Geometry & Applications.* 1995;05(01n02):75-91. doi: 10.1142/s0218195995000064.